From Phase-Engineered MoAlB to MoB MBene-MOF Nanocomposites: A Viable Route to High-Performance Electrocatalysts for Hydrogen Evolution

by

Tuğser Yılmaz

A Dissertation Submitted to the
Graduate School of Sciences and Engineering
in Partial Fulfillment of the Requirements for
the Degree of

Master of Science

in

Materials Science and Engineering

August, 2025

From Phase-Engineered MoAlB to MoB MBene-MOF Nanocomposites: A Viable Route to High-Performance Electrocatalysts for Hydrogen Evolution

Koç University

Graduate School of Sciences and Engineering

This is to certify that I have examined this copy of a master's thesis by

Tuğser Yılmaz

and have found that it is complete and satisfactory in all respects,
and that any and all revisions required by the final
examining committee have been made.

Committee Members:

Assoc. Prof. Umut Aydemir (Advisor)

Assoc. Prof. Uğur Ünal

Asst. Prof. Samira Fatma Kurtoğlu Öztulum

Date: 11.08.2025

To my lovely family…

ABSTRACT

From Phase-Engineered MoAlB to MoB MBene-MOF Nanocomposites: A Viable Route to High-Performance Electrocatalysts for Hydrogen Evolution

Tuğser Yılmaz
Master of Science in Materials Science and Engineering
August, 2025

The growing global energy crisis and the environmental consequences of fossil fuel consumption have accelerated the search for clean and sustainable energy sources. Among these, hydrogen has emerged as a promising energy carrier due to its high gravimetric energy density and zero-carbon emissions upon use. Electrocatalytic water splitting offers a green and efficient route to hydrogen generation, but its widespread application is hindered by the need for high-performance, earth-abundant electrocatalysts capable of facilitating both the hydrogen evolution reaction (HER) and oxygen evolution reaction (OER).

Two-dimensional (2D) transition metal borides, known as MBenes, have recently gained attention as next-generation electrocatalysts owing to their high electrical conductivity, chemical stability, and large surface area. In this thesis, a two-step strategy was developed to design MBene-based nanostructures for efficient HER catalysis.

In the first part of this thesis, the synthesis and chemical characterization of Mo_2AlB_2 were investigated using MoAlB, a member of the ternary transition metal boride (MAB phase) family. The primary objective of this study was to develop a novel approach for obtaining Mo_2AlB_2, which is considered the most suitable precursor phase for MoB MBene due to its favorable bonding characteristics. However, Mo_2AlB_2 is metastable and cannot be synthesized directly through conventional solid-state methods. Existing techniques reported in the literature typically require high temperatures, prolonged reaction times, and multiple processing steps. To address these limitations, a more efficient, low-temperature synthesis method was developed. The reaction was carried out at 450 °C for 2 hours using HCl gas, which was generated in situ through the thermal decomposition of NH_4Cl. This process enabled the production of high-purity Mo_2AlB_2 in

a single step. Structural and compositional analyses using XRD, SEM, TEM, EDX, ICP-MS and XPS confirmed the successful synthesis of Mo_2AlB_2 as a viable precursor for MoB MBene.

In the second part of the thesis, MoB MBene was synthesized from the MoAlB phase using a Lewis acid molten salt etching method. The as-obtained MBene was then combined with Ni-BDC, a nickel-based metal-organic framework (MOF), and deposited directly onto nickel foam via a solvothermal process at varying loading ratios. The aim was to fabricate a nanocomposite with a well-integrated interface that could lower the overpotential for HER by harnessing the high surface area of Ni-BDC and the excellent electrical conductivity of MoB MBene. At a current density of 10 mA cm^{-2}, the nanocomposite containing 7.5 wt.% MoB MBene exhibited an overpotential of 214 mV. Upon annealing at 400 °C, the formation of nickel nanoparticles further increased the surface area, resulting in a significantly reduced overpotential of 120 mV. Moreover, chronopotentiometric analysis demonstrated remarkable long-term stability, with the optimized catalyst maintaining consistent performance over 50 hours at 50 mA cm^{-2}.

This work introduces an efficient synthesis route for MBene-type materials and demonstrates their successful integration into hierarchical nanocomposites for electrocatalytic hydrogen production. The findings not only expand the synthetic toolbox for 2D boride materials but also underscore the promise of MBene-MOF architectures in green energy applications.

ÖZETÇE

MoAlB'nin Faz Mühendisliğiyle MoB MBene-MOF Nanokompozitlerine Dönüştürülmesi: Yüksek Performanslı Elektrokatalizör Üretimi için Yenilikçi Bir Yaklaşım

Tuğser Yılmaz
Malzeme Bilimi ve Mühendisliği, Yüksek Lisans
Ağustos, 2025

Küresel enerji krizinin derinleşmesi ve fosil yakıt tüketiminin çevresel etkileri, temiz ve sürdürülebilir enerji kaynaklarına olan ihtiyacı önemli ölçüde artırmıştır. Bu bağlamda, hidrojen; yüksek kütle başına enerji yoğunluğu ve kullanım sırasında sıfır karbon salınımı sayesinde umut vadeden bir enerji taşıyıcısı olarak öne çıkmaktadır. Elektrokatalitik su ayrıştırması, hidrojen üretimi için çevre dostu ve verimli bir yöntem sunsa da, bu sürecin yaygın uygulaması, hem hidrojen (HER) hem de oksijen (OER) üretim reaksiyonlarını kolaylaştırabilecek yüksek performanslı ve ucuz elektrokatalizörlere olan gereksinim nedeniyle sınırlanmaktadır.

Son yıllarda, iki boyutlu geçiş metali borürleri (MBene'ler), yüksek elektriksel iletkenlikleri, kimyasal kararlılıkları ve geniş yüzey alanları sayesinde yeni nesil elektrokatalizörler olarak dikkat çekmektedir. Bu tezde, HER reaksiyonu için yüksek verimli MBene tabanlı nanoyapılar tasarlamak amacıyla iki aşamalı bir strateji geliştirilmiştir.

Tezin ilk bölümünde, üçlü geçiş metali borürleri (MAB fazı) ailesinin bir üyesi olan MoAlB kullanılarak Mo_2AlB_2'nin sentezi ve kimyasal karakterizasyonu araştırılmıştır. Bu çalışmanın temel amacı, bağ yapısı açısından MoB MBene için en uygun öncül faz olarak kabul edilen Mo_2AlB_2'yi elde etmeye yönelik yeni bir yöntem geliştirmektir. Ancak, Mo_2AlB_2 metastabil bir fazdır ve geleneksel katı hâl yöntemleriyle doğrudan sentezlenmesi mümkün değildir. Literatürde raporlanan mevcut teknikler genellikle yüksek sıcaklık, uzun süreli reaksiyonlar ve çok aşamalı işlem adımları gerektirmektedir. Bu sınırlamaların üstesinden gelmek için, daha verimli ve düşük sıcaklıkta gerçekleştirilebilen bir sentez yöntemi geliştirilmiştir. Reaksiyon, düşük sıcaklıkta

NH_4Cl'nin termal bozunması sonucu yerinde (in situ) üretilen HCl gazı kullanılarak 450 °C'de 2 saat boyunca gerçekleştirilmiştir. Bu yöntemle, yüksek saflıkta Mo_2AlB_2 tek adımda başarıyla elde edilmiştir. XRD, SEM, TEM, EDX, ICP-MS ve XPS teknikleri ile yapılan yapısal ve bileşimsel analizler, Mo_2AlB_2'nin başarıyla sentezlendiğini ve MoB MBene için uygun bir öncül olduğunu doğrulamıştır.

Tezin ikinci bölümünde, MoAlB fazından MoB MBene üretimi için $ZnCl_2$ Lewis asidi içeren ergimiş tuz aşındırma yöntemi kullanılmıştır. Elde edilen MBene, daha sonra nikel bazlı bir metal-organik kafes yapı (MOF) olan Ni-BDC ile birleştirilmiş ve farklı katkı oranlarında solvotermal yöntemle nikel köpük üzerine doğrudan kaplanmıştır. Bu çalışmanın amacı, Ni-BDC'nin yüksek yüzey alanı ve MoB MBene'in üstün elektriksel iletkenliğinden yararlanarak HER için aşırı potansiyeli azaltabilecek, iyi entegre olmuş arayüzeylere sahip bir nanokompozit üretmektir. 10 mA cm^{-2} akım yoğunluğunda, % 7,5 ağırlıkça MoB içeren nanokompozit 214 mV'luk bir aşırı potansiyel sergilemiştir. 400 °C'de tavlama sonrası oluşan nikel nanoparçacıkları yüzey alanını daha da artırmış ve aşırı potansiyel değeri 120 mV'a kadar düşmüştür. Ayrıca, yapılan kronopotansiyometrik analizler, optimize edilen katalizörün 50 mA cm^{-2} akım yoğunluğunda 50 saat boyunca kararlı performans gösterdiğini ortaya koymuş ve uzun vadeli dayanıklılığını kanıtlamıştır.

Bu çalışma, MBene benzeri malzemeler için verimli bir sentez yolu sunmakta ve bunların MOF'larla birlikte hiyerarşik nanokompozitler içinde elektrokatalitik hidrojen üretimi amacıyla nasıl entegre edilebileceğini ortaya koymaktadır. Bulgular, yalnızca iki boyutlu borür malzemeleri için sentez araçlarını genişletmekle kalmamakta, aynı zamanda MBene-MOF mimarilerinin yeşil enerji uygulamaları için taşıdığı potansiyeli de ortaya çıkarmaktadır.

ACKNOWLEDGMENTS

I would like to express my appreciation for the financial assistance provided by TÜBİTAK under grant number 223M182.

I am especially grateful to my advisor, Assoc. Prof. Dr. Umut Aydemir, for the invaluable guidance, patience, and support he provided me throughout my graduate studies and thesis. At a time when I was unsure about my life's direction, he offered me the opportunity to discover myself and fulfill my potential, which was transformative for both my academic and personal development. His deep knowledge of chemistry and materials science and his inspiring leadership played a crucial role in the successful completion of this journey.

I would especially like to thank my thesis committee members, Assoc. Prof. Dr. Uğur Ünal and Asst. Prof. Dr. Samira Fatma Kurtoğlu Öztulum, for their support and contributions to the evaluation of this thesis. I would also like to thank Dr. Michael Baitinger from Max Planck Institute Chemical Physics of Solids, for his valuable contributions to my first publication. I am also grateful to Dr. Barış Yağcı and Dr. Hadi Jahangiri for their support and guidance throughout the materials characterization process.

I am also deeply grateful to the valued members of our catalysis group. I sincerely thank Dr. Naeimeh Sadat Peighambardoust, Dr. Ebrahim Sadeghi, and Dr. Sanaz Chamani for their kind support and guidance in understanding the electrocatalytic properties of the materials I prepared, as well as for their assistance in the analytical processes. I am equally grateful for their valuable contributions to my published papers.

I extend my heartfelt thanks to all my colleagues and friends at Koç University's Boron and Advanced Materials Application and Research Center (KUBAM) for their support, insightful discussions, and wonderful friendship throughout my research. I am especially thankful to Özden Güneş Yıldız, Samet Aydın, Melis Aktürk Aktaş, Aslı Ceren Can, Özlem Evren, Aybike Paksoy, Ali Arda Aydın, Pouriya Naziri, Saba Sepahban Shahgoli, Egemen Acar, and Gülçin Aliyeva. By exchanging ideas, engaging in open discussions, and seeking solutions together during challenging times, they not only lightened the workload but also made the process far more enjoyable and meaningful.

They were not just my labmates, we laughed together, shared thoughts, supported each other through tough times, and gave each other strength. Their presence made this journey truly special and unforgettable.

I would also like to extend my sincere gratitude to Merve Yılmaz, Sevgi Özen and Zeynep Özörnek, whom I met during my stay at the dormitory. The friendship, support and warm approach they showed during this challenging time transformed a simple living space into a place filled with a sense of belonging, and made this journey even more meaningful.

The two people I am most proud to remember while writing these lines are Tarık Safa Kaya and Fatih Uçar. From the very beginning of my undergraduate studies, we spent countless hours studying together, stayed up through sleepless nights, dreamed about the future, supported one another in every situation, and built a lasting friendship filled with both hard work and joy. I am deeply grateful for all those shared memories.

And lastly, perhaps most importantly, I would like to express my deepest and endless gratitude to my beloved family, my father Türker Yılmaz, my mother Ayşenur Yılmaz, and my sister Fulin Yılmaz. No words can truly express how much I appreciate their unwavering support and unconditional presence. Their encouragement has been the foundation of this entire journey.

TABLE OF CONTENTS

List of Tables xii

List of Figures xiii

Abbreviations xvii

Chapter 1: Introduction 1

1.1 Electrocatalytic Water Splitting 3

1.2 Fundamentals of Electrocatalytic Water Splitting 5

1.2.1 Hydrogen Evolution Reaction 6

1.2.2 Oxygen Evolution Reaction 8

1.3 Two Dimensional Transition Metal Borides 10

1.3.1 MAB Phases 11

1.3.2 MBene 13

1.3.3 MBene in Electrocatalytic Hydrogen Evolution Reaction 16

Chapter 2: One-Step Synthesis of Metastable Mo_2AlB_2 From MoAlB Using Gaseous HCl 18

2.1 Introduction 19

2.2 Experimental Methods 21

2.2.1 Characterization tecniques 21

2.2.2 Synthesis of powders 21

2.3 Chemical Characterization 25

2.4 Conclusions 32

Chapter 3: Hybrid Metal–Organic Framework/MBene Nanostructures Featuring Active Ni Sites for Boosted Hydrogen Evolution in Alkaline Media 33

3.1 Introduction 34

3.2 Experimental Methods 35

3.2.1 Catalyst Preperation 35

3.2.2 Materials Characterization 39

3.2.3 Electrochemical Characterization 40

3.3 Chemical Characterization 40

3.4 Electrochemical Studies 55

3.4.1 Electrocatalytic Activities of the Electrodes for HER 55

3.4.2 Post-Electrocatalysis Characterization 62

3.5 Conclusion 66

Chapter 4: Conclusion 67

Bibliography 70

Appendix A 81

Appendix B 83

LIST OF TABLES

Table 2.1 Comparative summary of synthesis methods for Mo_2AlB_2, showing experimental techniques and conditions. 20

Table 2.2 Atomic percentages of $MoAl_{1-x}B$ samples treated with 1M HCl for 6 hours at 25 °C, as determined by SEM-EDS analysis. 26

Table 2.3 Lattice parameters of Mo_2AlB_2 (space group *Cmmm*) in comparison with literature values. 28

Table 2.4 Atomic percentage of Mo_2AlB_2 from SEM-EDX. 30

Table 3.1 XPS results of MoB-7.5/Ni-BDC/NF/*400* as an atomic percent before and after stability test. 65

LIST OF FIGURES

Figure 1.1 Electrochemical water splitting cell configuration highlighting hydrogen evolution and oxygen evolution reaction processes at the cathode and anode, respectively [5]. 1

Figure 1.2 Schematic illustration of HER mechanisms under (a) acidic and (b) alkaline conditions [27]. 7

Figure 1.3 Hydrogen adsorption free energy (ΔG_{H^*}) volcano graphic of several metal catalysts in HER [28]. 8

Figure 1.4 2D materials family [33]. 10

Figure 1.5 MAB phase elements in the periodic table [41]. 12

Figure 1.6 Orthorombic crystal structures of MAB phases [49]. 13

Figure 1.7 A comparison of the bonding energies in M_2AlB_2-type MAB phases and M_2AlC-type MAX phases [10]. 14

Figure 1.8 Hydrogen coverage-dependent free energy diagrams for 2D MoB and FeB [10]. 17

Figure 2.1 Crystal structures of (a) MoAlB (*Cmcm*) [39] and (b) Mo_2AlB_2 (*Cmmm*); (c) Schematic representation of the reactor. 19

Figure 2.2 PXRD Pattern of α-MoB obtained from carbothermal reduction. 22

Figure 2.3 SEM images of the α-MoB with (a) low and (b) high magnification (SE contrast). 22

Figure 2.4 Comparison of the precursor phase MoAlB obtained from solid state reaction (blue pattern) and Mo_2AlB_2 obtained after 2h reaction with gaseous HCl at 450°C (pink pattern). The low-temperature reaction leads to a lower crystallinity and broader reflections..... 23

Figure 2.5 SEM images of MoAlB with (a) low and (b) high magnification (SE contrast). 23

Figure 2.6 The experimental setup used for the production of Mo_2AlB_2 from MoAlB by gaseous HCl. 24

Figure 2.7 PXRD patterns of MoAlB samples treated with HCl under various conditions, with the gaseous HCl experiment displayed at the top. The hatched area highlights peak positions corresponding to the (020) plane. 25

Figure 2.8 Mo_2AlB_2 products obtained from the reaction of MoAlB and gaseous HCl at different annealing conditions..... 27

Figure 2.9 HR-TEM images of (a) Mo_2AlB_2 with different d spacings corresponding to (b) (020), (c) (130), and (d) (131) planes..... 28

Figure 2.10 SEM images of Mo_2AlB_2 treated at 375 °C for (a) 30 min and (b) 2 h and at 450 °C for 2 h at (c) lower magnification and (d) higher magnification. 29

Figure 2.11 SEM-EDX investigation of Mo_2AlB_2. (a); EDX spectrum; (b) image with SE contrast; (c) elemental mapping of Mo, Al, and B..... 30

Figure 2.12 High-resolution XPS spectrum for Mo, Al, and B elements of (a) MoAlB and (b) Mo_2AlB_2. 31

Figure 3.1 Schematic illustration of the synthesis steps: (a) Preparation of layered ternary MoAlB compound via solid-state reaction; (b) Selective etching of Al layers using Lewis acid molten salt to produce MoB MBene; (c) In-situ growth of Ni-BDC MOF integrated with MoB MBene on NF (MoB/Ni-BDC/NF), followed by thermal treatment (MoB/Ni-BDC/NF/*T*). 39

Figure 3.2 XRD patterns of (a) MoAlB and MoB MBene, (b) Ni-BDC/NF and MoB-*X*/Ni-BDC/NF nanocomposites before and after annealing. 41

Figure 3.3 FT-IR results of (a) Ni-BDC, MoB-7.5/Ni-BDC, MoB-7.5/Ni-BDC/*300* and MoB-7.5/Ni-BDC/*400* and (b) TGA results of Ni-BDC, MoB-7.5/Ni-BDC, and MoB MBene..... 43

Figure 3.4 XRD pattern of (a) MoB-7.5/Ni-BDC annealed at 300 and 400 °C with the powder form and (b) MoB MBene annealed at 400 °C under Ar atmosphere. 44

Figure 3.5 SEM images of (a, b) MoAlB and (c, d) MoB MBene powder. 45

Figure 3.6 SEM-EDS results of MoB MBene at (a) low and (b) high magnification. 46

Figure 3.7 AFM images of MoB MBene..... 47

Figure 3.8 SEM images of (a) Ni-BDC/NF, (b) MoB-5/Ni-BDC/NF, (c) MoB-7.5/Ni-BDC/NF, (d) MoB-10/Ni-BDC/NF, (e, f) MoB-7.5/Ni-BDC/NF/*300* and (g, h) MoB-7.5/Ni-BDC/NF/*400* at low and high magnifications. 48

Figure 3.9 SEM-EDS elemental mapping of (a) Ni-BDC/NF, (b) MoB-7.5/Ni-BDC/NF, and (c) MoB-7.5/Ni-BDC/NF/*400*. 49

Figure 3.10 TEM images of (a) Ni-BDC, (b) MoB-7.5/Ni-BDC, and (c) MoB-7.5/Ni-BDC/*400*. HR-TEM images of (d) MoB-7.5/Ni-BDC/*400* and (e) HAADF-STEM image along with the corresponding EDS–STEM elemental mappings..... 50

Figure 3.11 TEM images of MoB MBene..... 51

Figure 3.12 Nitrogen adsorption–desorption isotherms (a) and corresponding BJH pore size distribution curves (b) of Ni-BDC, MoB-7.5/Ni-BDC, and MoB-7.5/Ni-BDC/*400* samples. 52

Figure 3.13 High resolution XPS spectrum (a) Ni 2p and (b) O 1s for Ni-BDC/NF, MoB-7.5/Ni-BDC/NF and MoB-7.5/Ni-BDC/NF/*400*; (c) Mo 3d and (d) B 1s for MoB/NF, MoB-7.5/Ni-BDC/NF and MoB-7.5/Ni-BDC/NF/*400*. 53

Figure 3.14 XPS high resolution spectrum of Mo 3d, B 1s, Al 2p for (a) MoAlB and (b) MoB MBene with Zn 2p. 55

Figure 3.15 (a) HER polarization curves of the samples, (b) 3D bar graphs of overpotentials at 10 and 50 mA cm^{-2}. 56

Figure 3.16 (a) HER Tafel plots obtained by polarization curves, (b) EIS spectra recorded at 0.0 V versus RHE. 58

Figure 3.17 Typical cyclic voltammetry (CV) curves obtained at different scan rates (0.06–0.20 V s-1) within the potential window 0.65–0.75 V vs RHE for (a) Ni-BDC/NF,

(b) MoB-5/Ni-BDC/NF, (c) MoB-7.5/Ni-BDC/NF, (d) MoB-10/Ni-BDC/NF, (e) MoB-7.5/Ni-BDC/NF/*300* and (f) MoB-7.5/Ni-BDC/NF/*400*. 59

Figure 3.18 Capacitive current density versus scan rate curves for ECSA measurements (a) before and (b) after annealing. 60

Figure 3.19 (a) TOF values of the samples at various overpotentials, (b) long-term HER stability test of best performing MoB-7.5/Ni-BDC/NF/*400* at the applied current densities of 10 and 50 mA cm^{-2}. 61

Figure 3.20 HER polarization curve of the MoB-7.5/Ni-BDC/NF/*400* catalyst after a 50 h stability test under a constant current density of 50 mA cm^{-2}. 62

Figure 3.21 SEM images of MoB-7.5/Ni-BDC/NF/*400* after (a) 1 HER run and (b) 50 h HER stability test. (c) TEM and (d) HR-TEM images of MoB-7.5/Ni-BDC/NF/*400* after 50 h HER. 63

Figure 3.22 TEM-EDS elemental mappings of MoB-7.5/Ni-BDC/NF/*400* after 50 hours stability test at a current density of 50 mA cm^{-2}. 63

Figure 3.23 High-resolution XPS spectra of MoB-7.5/Ni-BDC/NF/*400* after HER and 50-hour stability testing: (a) Ni 2p, (b) Mo 3d, (c) B 1s, (d) O 1s. 65

ABBREVIATIONS

HER	Hydrogen Evolution Reaction
OER	Oxygen Evolution Reaction
2D	Two Dimensional
MBene	Two Dimensional Transition Metal Boride
MAB	Ternary Transition Metal Boride
MAX	Ternary Transition Metal Carbide
XRD	X-Ray Diffraction
SEM	Scanning Electron Microscopy
EDX	Energy Dispersive X-Ray Spectroscopy
TEM	Transmitted Electron Microscopy
XPS	X-Ray Photoelectron Spectroscopy
AFM	Atomic Force Microscopy
FTIR	Fourirer-Transform Infrared Spectroscopy
MOF	Metal Organic Framework
DFT	Density Functional Theory
AWE	Alkaline Water Electrolyzer
PEMWE	Proton Exchange Membrane Water Electrolyzer
AEMWE	Anion Exchange Membrane Water Electrolyzer
TOF	Turnover Frequency
EIS	Electrochemical Impedance Spectroscopy
ECSA	Electrocatalytic Active Surface Area
CV	Cyclic Voltametry
AEM	Adsorbate Evolution Mechanism
LOM	Lattice-Oxygen-Mediated Mechanism

Chapter 1: Introduction

One of humanity's major developments during the 18th century was the Industrial Revolution . The invention of steam locomotives and internal combustion engines greatly facilitated human life. This progress, along with the development of systems such as electronics and automation in the 19th and 20th centuries, has continued to this day [1]. However, increasing energy demand has created significant challenges in determining the resources needed to meet this demand. While fossil fuels have long played a significant role in meeting energy demand, scientific research highlighting the impact of their byproducts, greenhouse gases, on global warming has suggested that a shift toward renewable energy alternatives is more appropriate [2]. Hydrogen energy distinguishes itself among alternative energy sources with its exceptionally high gravimetric energy density and environmentally friendly, carbon-free composition. The problems with clean, sustainable hydrogen production and storage, however, continue to be serious concerns. Today, industrial hydrogen production is primarily based on coal gasification and steam methane reforming, processes that release harmful gases and thus cause environmental pollution [3]. In recent years, hydrogen production by water electrolysis (Figure 1.1) has become the focus of laboratory research and has begun to take place in industrial applications due to its simplicity, cost-effectiveness and high purity output [4].

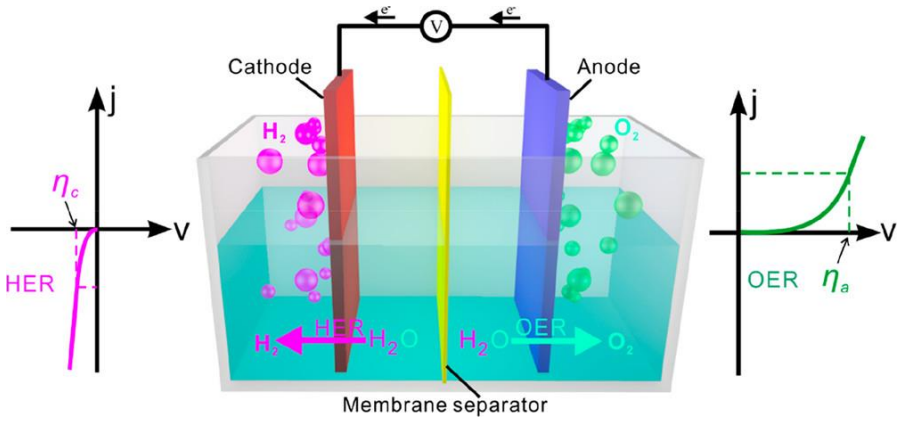

Figure 1.1 Electrochemical water splitting cell configuration highlighting hydrogen evolution and oxygen evolution reaction processes at the cathode and anode, respectively [5].

Various methods have been developed for hydrogen production via water splitting, including two-electrode electrochemical cells, solar cells, thermoelectric devices, photoelectrodes, and triboelectric nanogenerators [6]. These systems generally operate

based on similar theoretical principles. Although a theoretical potential of 1.23 eV is required, it is insufficient to initiate the reaction, and in practice, a higher potential is generally required [2]. To reduce this overpotential, materials that are not degraded by the system, called catalysts, are used. Carbon-supported platinum (Pt/C) is generally used as the hydrogen evolution catalyst, while ruthenium and iridium oxides are preferred for oxygen evolution. However, due to their scarcity and high cost, alternative catalyst materials are being investigated. In particular, low-cost and abundant bifunctional catalysts that can facilitate both reactions have become the focus of research [7].

In electrochemical water splitting, specific surface area, catalytic activity, and electrical conductivity are critical parameters [5]. Transition metal-based carbides, oxides, hydroxides, phosphides, nitrides, and borides have been extensively studied for this purpose due to their natural abundance, low cost, scalability, and high chemical stability [8]. The discovery of graphene led to a sharp rise in interest in two-dimensional (2D) materials. When the A element from the proper MAX phases (M: transition metal, A: Group 3A or 4A element, X: C, N, or CN) is selectively etched, a new class of 2D transition metal carbides, nitrides, and carbonitrides is created [9]. Subsequently, due to the neighboring positions of carbon and boron in the periodic table and their similar properties, computational studies have shown that 2D transition metal borides (MBenes) can also be synthesized [10]. These materials have become the focus of interest for energy-related applications, especially batteries, supercapacitors, and electrochemical water splitting [11, 12], due to their high surface area because of layered structure and their excellent catalytic activity attributed to the presence of transition metals.

Density functional theory (DFT) studies have shown that Cr, Mn, Fe, Co, and Ni-based materials, such as Fe_3B_4, Co_3B_4, and Ni_2B_2, are suitable hydrogen evolution reaction (HER) electrocatalysts in various MBene structures, including M_2B_2, M_3B_4, and M_4B_6 configurations [13]. Among MoB MBenes doped with different transition metals, $Ni@Mo_2B_2$ has been reported as a particularly effective bifunctional electrocatalyst [14]. Another study showed that Fe_2B_2 MBene exhibited high catalytic activity for HER [10]. Mo-doped Hf_2BO_2 has also been identified as a promising HER catalyst [15]. Based on these computational findings, it is anticipated that experimental studies may yield successful results, as these MBene-like materials exhibit high metallic conductivity, low

electrical resistivity, and efficient charge transport properties that enhance electrochemical performance [16].

On this basis, research was conducted to address the lack of experimental studies on catalyst design for the synthesis of Mo-based MBene and their applications in electrocatalytic HER. In the first part, Mo_2AlB_2, which is shown as the precursor material to obtain 2D MoB from MoAlB, was synthesized and characterized in a single-step, innovative, and effective manner. Subsequently, in the second part, Mo_2B_2 MBene was synthesized using the Lewis acidic molten salt method. This was followed by the fabrication of a nanocomposite containing a Ni-based metal-organic framework (MOF). The resulting materials were systematically investigated and characterized for their electrocatalytic HER performance.

1.1 Electrocatalytic Water Splitting

The first water electrolysis experiment was conducted in 1789, utilizing gold electrodes and passing an an electric current through water [17]. Despite attempts 250 years ago with water, the majority of hydrogen production today still relies on methods such as steam methane reforming, coke gasification, and oil reforming or gasification. Only 4% of H_2 production worldwide is achieved by water electrolysis [18]. This is primarily due to the small-scale nature of electrolysis and the high costs associated with building specialized facilities. However, increasing environmental concerns, such as global warming, have heightened interest in water electrolysis as a clean method for producing hydrogen. The use of water as a raw material and the absence of harmful or hazardous by-products are the main reasons for the choice. Furthermore, if the electricity used in the process is sourced from renewable energy, water electrolysis becomes a sustainable option within the hydrogen economy [6].

Water splitting is not a thermodynamically spontaneous reaction because the Gibbs free energy change ($\Delta G = +237.1$ kJ/mol) remains positive over a wide temperature range. ΔG becomes negative only at about 2000 K below 1 bar, and a temperature of about 4000 K is required for hydrogen to reach 50% conversion [17]. Therefore, under standard conditions, external energy input, such as electricity or light, is required to initiate the reaction. Depending on the energy source, the processes are called electrocatalytic or photocatalytic water splitting. Electrochemical water splitting consists of two half-

reactions: the hydrogen evolution reaction (HER) occurring at the cathode and the oxygen evolution reaction (OER) taking place at the anode [19]. The electrolyte facilitates ion transport, while the external circuit provides electron flow [20] (Figure 1.1). Water is reduced at the cathode to produce hydrogen and oxidized at the anode to produce oxygen when a potential is applied.

Theoretically, regardless of pH, water dissociation takes place at an applied potential of 1.23 V at 25 °C and 1 atm. For both HER and OER, the multistep nature and slow kinetics of the reactions often necessitate a higher potential than necessary. Electrocatalysts that help reduce this additional potential increase both the efficiency and the reaction rate of the system [21]. Catalysts are typically classified as either homogeneous or heterogeneous based on whether they share the same phase with the reactants. Homogeneous electrocatalysts are molecular species that dissolve in water, whereas heterogeneous electrocatalysts are solid materials that are insoluble in water and are usually immobilized on the surface of the working electrode [22].

Hydrogen production via low-temperature water splitting is generally divided into three main types: alkaline water electrolyzers (AWEs), proton exchange membrane water electrolyzers (PEMWEs), and anion exchange membrane water electrolyzers (AEMWEs) [23]. While low-cost electrocatalysts with high catalytic activity at low current densities have been developed for each of these systems, industrial-scale AWEs require electrocatalysts that can operate efficiently at high current densities up to 500 mA cm^{-2}. At such high current densities, gas bubble formation occurs at the electrode surface. These bubbles, formed at the solid-liquid interface, inhibit mass transfer and block the active sites, resulting in increased ohmic resistance and subsequent reduction in overall performance [24]. Therefore, selecting a suitable electrocatalyst to improve both activity and efficiency under these conditions is critical.

Noble metal-based catalyst materials exhibit high performance particularly under acidic electrolytes, for example, Pt for HER and IrO_2 and RuO_2 for OER in H_2SO_4. In contrast, transition metal-based catalysts demonstrate strong activity in alkaline environments, such as Ni for HER and stainless steel composites for OER in KOH. Although the high performance of noble metal-based electrocatalysts is well established, their high cost, scarcity, and limited stability have accelerated the search for alternatives [21]. Meanwhile, the moderate efficiency of noble metal-free electrocatalysts has

sustained continued research efforts. In particular, during electrocatalytic water splitting in alkaline media, the high dissolution rates of noble metals have prompted the use of techniques such as surface modification and doping to enhance their stability [6]. Alternatively, research efforts have increasingly focused on designing low-cost, earth-abundant, and high-performance catalysts based on non-noble metal based compound to achieve long-term stability.

1.2 Fundamentals of Electrocatalytic Water Splitting

Two components are required for water electrolysis: electrodes (cathode and anode) and the electrolyte. In essence, an oxidation process takes place at the anode and a reduction reaction at the cathode if the externally applied potential is greater than the equilibrium potential. The net reaction in water electrolysis is as follows (Equation 1.1):

$$2H_2O \rightarrow 2H_2 + O_2 \tag{1.1}$$

The standard equilibrium potential required for this to occur is U_0 = 1.229 V under conditions of T = 298 K, P = 1 atm, and pH = 0. The equilibrium potential is determined from the Gibbs free energy equation [23] (Equation 1.2).

$$\Delta G_R^0 = -nFU_0 \tag{1.2}$$

The potential required to be applied to the cell can sometimes reach up to 1.8 V, which is related to the activation barrier because of sluggish reaction kinetics [2]. Overpotential refers to the additional applied potential in relation to the theoretical value [25]. Therefore catalysts are used to reduce overpotential and increase energy efficiency. Material design for catalysts is of great importance, and high performance catalyst must be catalytically active and stable. To evaluate an electrocatalyst, values such as overpotential (η), tafel slope, charge transfer resistance (R_{ct}), double layer capacitance (C_{dl}) and turnover frequency (TOF) are examined. Linear Sweep Voltammetry is used for overpotential evaluations, a certain potential range is scanned and the overpotential is found by calculating the potential corresponding to a 10 mA cm^{-2} current density value. A reduced overpotential indicates a more effective catalyst, thereby enhancing the overall efficiency of the water splitting process [25]. The tafel slope is derived from Equation 1.3, where b is the tafel slope and j is the current density.

$$\eta = a + b \log j \quad (1.3)$$

A smaller Tafel slope reflects faster reaction kinetics, implying that a higher current density can be achieved with a smaller increase in applied potential [25]. Electrochemical Impedance Spectroscopy (EIS) is used to analyze charge transfer processes. The impedance of the system to an applied AC signal at different frequencies is measured. The semicircular portion of a Nyquist diagram is often referred to as the charge transfer resistance. A lower R_{ct} indicates faster reaction kinetics, lower electrode-electrolyte resistance [26]. Catalyst stability is measured by chronopotentiometry or chronoamperometry. A constant current or potential is applied, and changes in potential or current are observed over time [25]. For example, using chronopotentiometry, the change in catalyst potential over a 50 hour period can be analyzed at current densities of 10, 50, or 100 mA cm^{-2}. The change in overpotential can then be reassessed by repeating the LSV after the stability test. Electrocatalytic active surface area (ECSA) is determined using cyclic voltammetry (CV) at different scan rates, result give double layer capacitance (C_{dl}). A higher C_{dl} value indicates more electrochemically active sites on the electrode surface. The TOF is a measure of how much product each active site produces in a given length of time [25]. A high TOF value indicates a higher intrinsic activity of the catalyst and a more efficient operation of each active site.

Resulting from the decomposition of water, the formation of H_2 and O_2 occurs through two half-reactions. Since H_2 formation is the result of water reduction, it occurs at the cathode, while O_2 formation is observed at the anode because it is an oxidation reaction.

1.2.1 Hydrogen Evolution Reaction

HER varies depending on pH in acidic and basic environments. The binding energy of hydrogen and water dissociation are two important parameters for the HER [25]. The HER that occurs in acidic environments is as follows (Equation 1.4):

$$H^+ + e^- \rightarrow H^*, \quad (1.4)$$

$$H^+ + e^- + H^* \rightarrow H_2,$$

$$H^* + H^* \rightarrow 2H^*$$

Volmer, Heyrovsky, and Tafel are the names of these chemical stages, respectively. Two of these steps occur together, resulting in the formation of hydrogen, which are the Volmer-Tafel or Volmer- Heyrovsky reaction pathways in both acidic and alkaline medium. In acidic environments, the proton source are hydronium ions (H_3O^+). The first step in both reaction pathways is the Volmer reaction, where hydrogen is adsorbed on the catalyst active site along with electron transfer from the electrode. After that, the reaction can either proceed via the Heyrovsky step, in which the adsorbed hydrogen combines with protons to generate H_2, or the Tafel step, in which two adsorbed hydrogen combine to make H_2 (Figure 1.2) [23].

In alkaline environment, since there are no protons in the electrolyte, H_2O acts as a proton source and the reaction pathway is as follows in equation 1.5:

$$H_2O + e^- \rightarrow OH^- + H^*, \tag{1.5}$$

$$H_2O + e^- + H^* \rightarrow OH^- + H_2,$$

$$H^* + H^* \rightarrow H_2$$

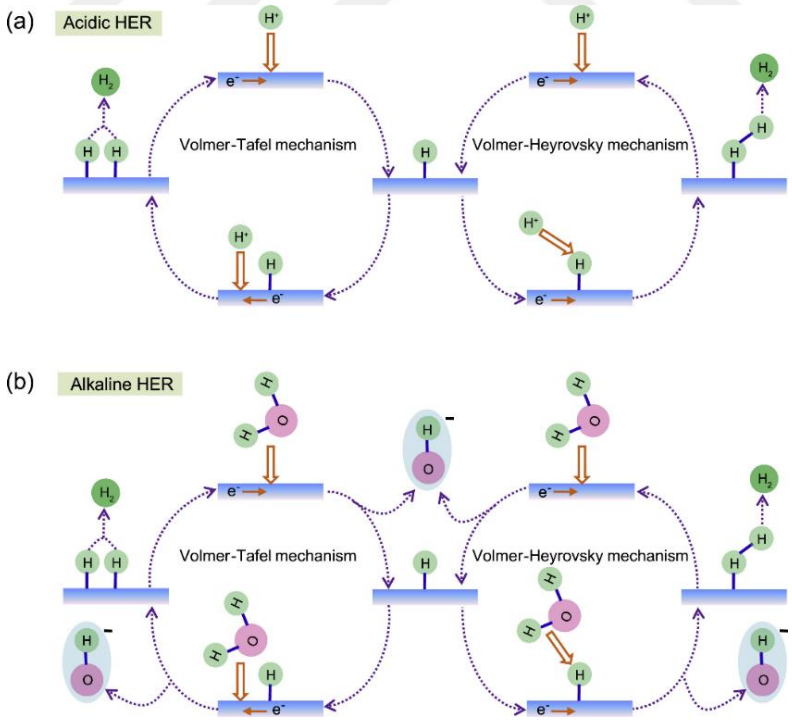

Figure 1.2 Schematic illustration of HER mechanisms under (a) acidic and (b) alkaline conditions [27].

The reaction steps are Volmer, Heyrovsky and Tafel steps, respectively. Hydrogen formation begins with water dissociation and continues with the Heyrovsky or Tafel step. In the Volmer mechanism, the first step of the reaction, the metal must possess sufficient binding energy to adsorb a proton to its surface. However, if this bond is too strong, the hydrogen species formed will be trapped on the surface, making desorption difficult and potentially clogging the catalyst surface. This demonstrates that HER performance is directly related to the interaction strength between the catalyst surface and the adsorbed hydrogen [23]. Figure 1.3 shows the Volcano plot of hydrogen adsorption free energy (ΔG_{H^*}), showing that Pt metal are the best HER materials as its medium bond strength which is in the optimum position for hydrogen adsorption [28].

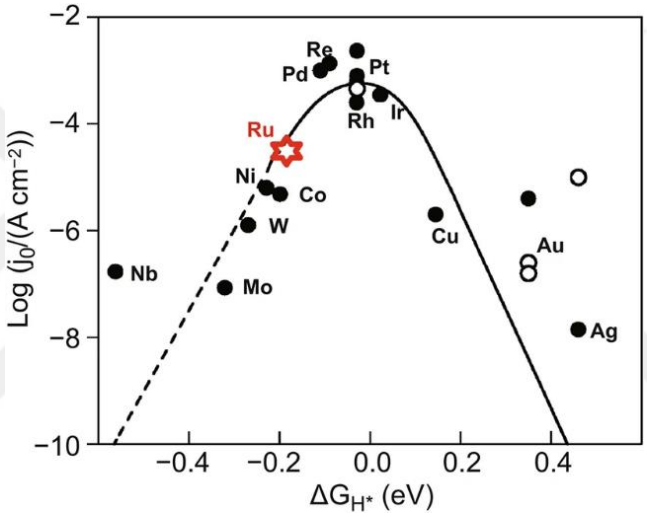

Figure 1.3 Hydrogen adsorption free energy (ΔG_{H^*}) volcano graphic of several metal catalysts in HER [28].

The HER mechanism varies highly depending on process parameters such as electrolyte pH, electrode potential and electrode material [23]. The reaction proceeds much less efficiently in an alkaline environment since the proton supply is much lower than in an acidic environment. Therefore, in an alkaline environment, water dissociation occurs first, and the reaction continues. In industrial applications, processes are carried out using more alkaline media than acidic [25].

1.2.2 Oxygen Evolution Reaction

OER is much more complex than the HER reaction because it involves a four-electron transfer. This situation reduces the reaction kinetics and causes the overpotential to become much more severe. The two main methods that the reactions for OER might

happen are through the adsorbate evolution mechanism (AEM) and the lattice-oxygen-mediated mechanism (LOM). In the AEM mechanism, 4 electron-proton transfers occur through the active sites [29]. The following route is pursued by the AEM reaction (Equation 1.6):

$$H_2O + * \rightarrow OH^* + H^+ + e^- \quad 1.6$$

$$OH^* \rightarrow O^* + H^+ + e^-$$

$$O^* + H_2O \rightarrow OOH^* + H^+ + e^-$$

$$OOH^* \rightarrow * + O_2 + H^+ + e^-$$

First, water adsorbs via a one-electron oxidation process, forming OH* on the metal site. Then, OH* undergoes proton coupling and loses electrons, turning into O*. O* then combines with another OH^- to form OOH*, which then releases O_2. The resulting void is filled with a new OH^- which is coming from electrolyte completing the cycle. Each step has specific free energy and by comparing these values, the step that the highest ΔG is determined as the rate determining step, and accordingly the overpotential of the OER can be calculated theoretically [29].

In the LOM mechanism, the reaction begins with the formation of O*, as in AEM. This O* then combines with the oxygen in the material's structure, releasing O_2 gas, creating a vacancy in the structure. This vacancy is refilled with OH^- ions from the electrolyte. Since there is no OOH* intermediate is formed in LOM, some energy constraints are eliminated [30].

Materials based on noble metals, including Ir and Ru, perform well during OER. Since high potentials are applied during the reaction, noble metal oxides such as RuO_2 and IrO_2 are commonly used as benchmark electrocatalysts. Stability problems, similar to those encountered with Pt used in HER applications, are also encountered. RuO_2 can decompose in both acidic and basic electrolytes. However, IrO_2 exhibits greater stability than RuO_2 in high anodic potentials. Due to their high cost, research is underway to develop high-performance, more stable, environmentally friendly, and easily prepared transition metal-based electrocatalysts. For OER, perovskite and spinel oxides are

therefore recommended. Transition metal content in the materials allows for design flexibility thanks to their multiple oxidation states and coordination environments [29].

1.3 Two Dimensional Transition Metal Borides

The discovery of graphene, a single-layer carbon layer with a hexagonal structure, using the scotch tape method from graphite, ushered in a new era in materials science [31]. Numerous investigations have been conducted because to its remarkable electrical conductivity and great strength. Furthermore, interest in 2D materials has grown even further, and in subsequent years, 2D materials have been produced using van der Waals materials such as metal chalcogenides, boron nitride, and black phosphorus (Figure 1.4). This weak van der Waals bond between layers has enabled the production of various materials using mechanical methods such as top-down exfoliation [32].

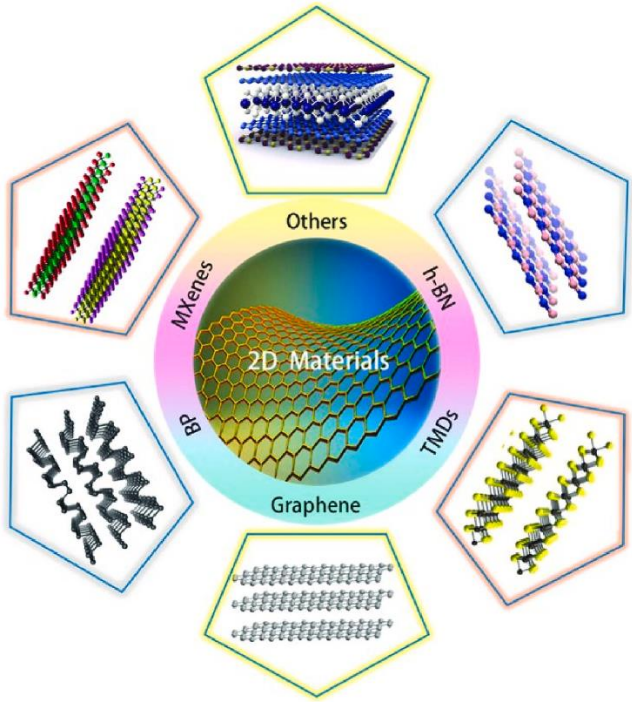

Figure 1.4 2D materials family [33].

Two-dimensional materials can also be produced using selective etching using crystalline materials with covolent, ionic, and metallic bonds between layered structures, interconnected by hybrid bonds. A specific example of this is the synthesis of $Ti_3C_2T_x$ using Ti_3AlC_2, a ternary transition metal carbide (MAX phase) member, discovered by Gogotsi and colleagues in 2011 [34]. The basic principle here is to exploit the fact that the Ti-Al bond in the hexagonal Ti_3AlC_2 is metallic, while the Ti-C bond is a mixed

covolent/ionic bond. Using HF acid, it selectively removes Al from the weak Ti-Al bond as AlF_3, but HF has no effect Ti-C bond. This results in the formation of interstitial structures between the TiC layers, resulting in an accordion-like morphology with surface functionality. These resulting materials are called MXene, the "ene" suffix emphasizing their two-dimensional nature, similar to graphene. Since there are more than 300 transition metal carbides/nitrides/carbonitrides in the MAX phase family, MXene can be produced in a wide range of material compositions [35].

Ternary transition metal borides, called MAB phases, can also be synthesized by substituting boron for carbon or nitrogen in the MAX phases. Although numerous structural variations are present, it has been suggested, and computational studies have shown, that two-dimensional transition metal borides, or MBenes, can also be synthesized because they share similar bond structures in the crystal [10]. In this section, MAB phases, MBene synthesis, characterization and usage in electrocatalysis are investigsted.

1.3.1 MAB Phases

Boron (B), due to its location alongside carbon (C) on the periodic table, has always spurred considerable research. Transition metal borides possess rich chemical properties due to the smaller number of electrons in B compared to C and this electron deficieny allows to formation of complex metal boride. In addition, the small size of the B atom allows the electrons in its outer shell to be strongly attracted by the nucleus, preventing the formation of ions. Therefore, transition metal borides have high melting point and other properties such as their high hardness, high thermal resistance, and electrical conductivity [36]. These properties have also led to an increase in the application areas of transition metal borides.

The MAB phase is a synonym, M represents transition metals, A stands for the elements of group 3A or 4A (mostly Al, In or Si), and finally B represents boron which are clearly shown in Figure 1.5 [37]. The first material included in this group was $Mo_7Al_6B_7$, which was synthesized and analyzed in 1942 in the orthorhombic crystal structure of the *Pmmm* space group [38]. MoAlB was subsequently improved in the *Cmcm* orthorhombic structure in 1966 [39]. Subsequently, MAB phases were synthesized with other transition metals such as W, Mn, Cr and Fe. However, the abbreviation "MAB" was first coined in 2015 by Ade et al. [40], who synthesized a Cr_4AlB_6 along with other

phases based on Mo, Cr, Mn and W single crystals, as a result of the similarity of atomically laminated transition metal borides to the MAX phases.

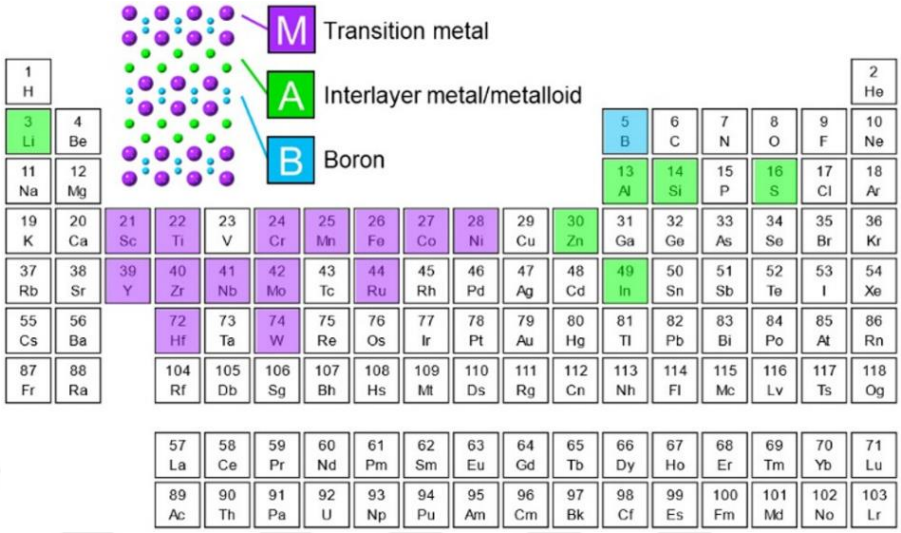

Figure 1.5 MAB phase elements in the periodic table [41].

The general formula for MAB phases is $(MB)_{2z}A_x(MB_2)_y$ (z = 1-2; x = 1-2; y = 0-2), and M-B sublattices are separated by interleaved monolayer or bilayer A atoms. Atoms of transition metals are grouped in triangular prisms and connected by shared faces, while B atoms form zigzag chains or bands of six rings (BM_6) [42]. MAB phases have crystal structures of either orthorhombic or hexagonal [11]. When examining orthorhombic MAB phases, the stoichiometry of the orthorhombic structures varies depending on the M:B ratio and the A planes separating the layers [42]. Orthorhombic phase lattice structures come in six varieties: M_2AB_2, $M_2A_2B_2$, $M_3A_2B_2$, M_3AB_4, M_4AB_4 and M_4AB_6 and only $M_2A_2B_2$ has a double-layered zigzag-shaped Al layer (Figure 1.6) [43]. Although the M_4AB_4 phase does not conform to the general formula, it is included as a MAB phase, and Cr_4AlB_4 has also been synthesized experimentally [44, 45]. Other experimentally synthesized orthorhombic Al contains MAB phases are MoAlB, WAlB, Fe_2AlB_2, Mn_2AlB_2, Cr_2AlB_2, Cr_3AlB_4, and Cr_4AlB_6 [40].

While most studies to date have focused on orthorhombic MAB phases, atomically laminated phases with hexagonal crystal structures also exist. M_2AB_2 and M_3AB_4 are theoretically calculated and known to be stable [43]. Experimental synthesis of Ti_2InB_2 and Hf_2InB_2 MAB phases has also been achieved [46, 47]. Furthermore, quaternary hexagonal phases formed by adding another transition metal to the structure are designated as *i*-MAB phases. The designation here is generally $(M'_{4/3}M''_{2/3})AlB_2$, and the

larger radius and lower electronegativity of the M'' atom relative to M' have been shown to increase phase stability [37]. So far, the materials that have been experimentally synthesized under the *i*-MAB phase are $Mo_{4/3}Y_{2/3}AlB_2$ and $Mo_{4/3}Sc_{2/3}AlB_2$ [48].

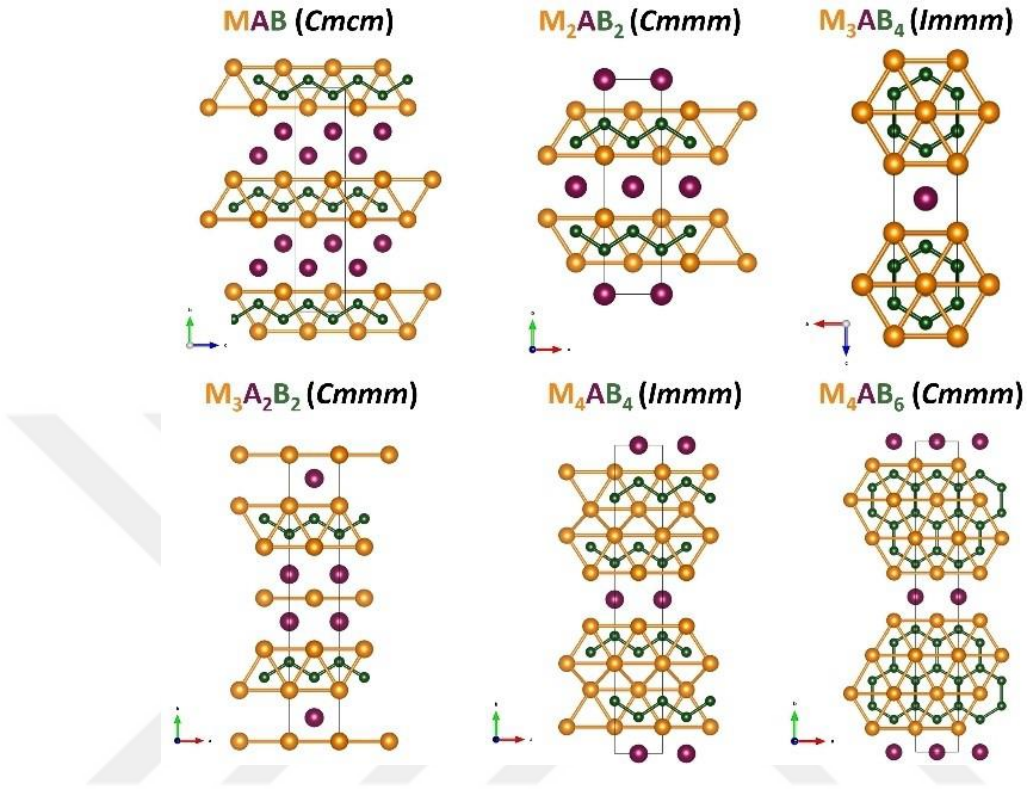

Figure 1.6 Orthorombic crystal structures of MAB phases [49].

1.3.2 MBene

The feasibility of MBene synthesis stems from the bond strengths in the MAB phase; the same situation exists in MXene. In the MAB phases, a metallic bond exists between M-A (secondary bond), while between M-B, a mixed covalent/ionic bond (primary bond) is present. Essentially, due to the difference in bond strength between these two different bondings, element A can be etched and removed without damaging the M-B bond [43]. A computational study examining the bond energies in the M_2AlB_2 type MAB phases containing transition metals such as Cr, Mo, W, and Fe showed that the M-B bond energy is nearly twice the M-Al bond energy (Figure 1.7) [10]. This is also the same for the common MAX phases. The M-B bond strength is also directly related to the thermodynamic stability of the resulting MBene . This is because the removal of metal A typically creates an acidic, harsh environment, and this bond must be protected from this environment.

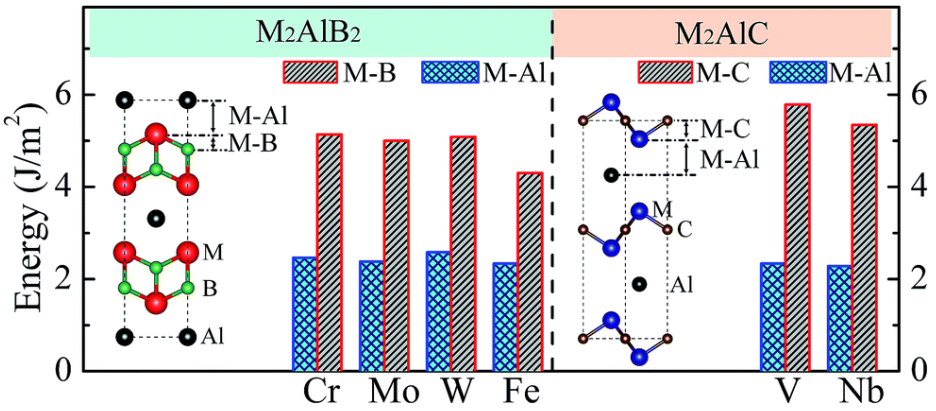

Figure 1.7 A comparison of the bonding energies in M_2AlB_2-type MAB phases and M_2AlC-type MAX phases [10].

The initial MBene synthesis method was generally considered to utilize techniques previously tested in MXene synthesis. The most common technique is the use of HF acid, and computational studies on MBenes have shown that HF causes deintercalation in MAB phases of the M_2AlB_2 type by forming AlF_3 and H_2, and that showed the synthesis of 2D structured MBene is feasible using strong acid like HF [10]. For this reason, HF treatment has been experimentally applied. Furthermore, since HF use is known to have harmful health effects, acidic/basic aqueous solution treatments, hydrothermal reactions, and Lewis acid molten salt techniques have also been tried for MBene synthesis.

Treatment trials using HF and in situ generated HF involve prolonged processing steps, and additional extensive washing is required to neutralize the solution pH to 7 at the end of the procedure. Alameda et. al [50] showed that experiments done using HF and in situ HF (2 M LiF + 6 M HCl) on single crystal MoAlBs demonstrated that etch cavities formed on the MoAlB but also caused corrosion in the MoB layers. Furthermore, it was observed that not all of the Al in the structure was etched. Kim et al. [51] showed that by applying 3 M LiF + 10 M HCl on MoAlB for 48 h, the metastable phase Mo_2AlB_2 product was obtained in which half of the Al was removed. In the study by Wang et al. [52] 2D MnB was obtained as a result of the reaction in LiF + HCl solution using Mn_2AlB_2 as the precursor material. In another work done by Zhou et al. [53], as a result of the reaction carried out with $(Mo_{2/3}Y_{1/3})_2AlB_2$ using 22.5 M HF for 3 hours, 2D $Mo_{4/3}B_{2-x}$ boridine containing a metal vacancy was obtained after tetrabutylammonium hydroxide (TBAOH) treatment which was applied to further increase the distance between the layers. Wang et al. [54] imply that $Mo_2ErB_3T_{2.5}$ was obtained after the $(Mo_{2/3}Er_{1/3})_2AlB_2$ MAB phase was stirred in a mixture of HF (13.5 M) and HCl (4.8 M) for 30 hours.

Although acidic/basic aqueous solution treatments generally involve easy processing, long periods are needed for the reaction to occur completely. Zhang et al. [55] obtained 2D CrB by using the Cr_2AlB_2 MAB phase and stirring it in 1.25 M HCl for 8 hours at room temperature. XRD results showed that the formed CrB had -OH surface termination. A study by Alameda et al. [56] using 10 wt.% % NaOH on MoAlB initially determined that some of the Al was removed, yielding $MoAl_{1-x}B$ (1-x, refers to etch less than 25% Al). Subsequent annealing at 600 °C for 4.5 h resulted in Mo_2AlB_2 formation. Bury et al. [57] showed that the combined use of HCl and H_2O_2 on MoAlB resulted in the synthesis of single or few-layer MBene after 48 hours.

Synthesis attempts by hydrothermal reaction were generally carried out with concentrated NaOH. Xiong et al. [58] obtained MoB MBene by reacting MoAlB in 25 wt.% NaOH at 150 °C for 24 h using a hydrothermal reactor. In another study, Wei et al. [59] produced single/few-layer MoB MBene by hydrothermal reactions using the MoAlB MAB phase with 0.25 M NaOH at 200 °C. Khan et al. [60] produced $Mo_{4/3}B_2T_x$ MBene from the $(Mo_{2/3}Y_{1/3})_2AlB_2$ MAB phase by hydrothermally reacting it for 24 hours at 150 °C in 25 wt.% NaOH.

Studies using Lewis acid molten salts generally used transition metal salts $ZnCl_2$ and $CuCl_2$, especially for MBene synthesis. Mou et al. [61] obtained 2D MoB by applying a heat treatment at 700°C for 2 hours to a mixture of MoAlB and $ZnCl_2$ in a 1:2 molar ratio and then treating it with dilute HCl to separate Zn-based byproducts. Another study done by Baumler et al. [62] $ZnCl_2$ lewis acid molten salt method preferred, and after 170 h at 550 °C, Mo_2AlB_2 was obtained. Li et al. [63] used $CuCl_2$, NaCl, and KCl salts to remove Al from the MoAlB MAB phase in a 1:6:1:1 (MoAlB:$CuCl_2$:NaCl: KCl) molar ratio. Additional NaCl and KCl were added because of increasing molten salt efficiency. Immediately after a 30-minute treatment at 650 °C, byproduct Cu was removed with an ammonium persulfate (APS) solution treatment to obtain the phase-pure Mo_2AlB_2. Chen et al. [64] used a salt mixture containing $CuCl_2$, NaCl, and KCl in a 1:3:2:2 molar ratio to remove Al in the MoAlB phase. This mixture was annealed for 24 hours at 640 °C in an Ar atmosphere, followed by washing with an APS solution to obtain a Mo_xB_y MBene.

1.3.3 MBene in Electrocatalytic Hydrogen Evolution Reaction

MBenes are suitable materials for energy applications such as electrocatalytic water splitting due to their high surface area, electrical conductivity, low resistance, and surface functionalization [11]. Electrical conductivity is an important parameter for electrocatalysis because of electrode-electrolyte electron transfer is critical [65]. Since the electrons in MBene are in the *d* state, due to the M metal, they must exhibit metallic properties and be electrically conductive [16]. Surface functions such as -F, -Cl, and -OH, which form depending on the synthesis method, also maintain this state as metallic or semimetallic [16, 43]. Other 2D materials such as molybdenum dichalcogenides (MoS_2) and graphitic carbon nitride (gCN) have high surface area but low charge transfer performance because they behave like semiconductors. On the other hand, catalytically active sites do not include in-plane atoms but are instead limited to corners and defective atoms [12].

Three state diagrams show the HER process, and the formulation comprises $H^+ + e^-$, H*, and H_2 formation, in that order. The Gibbs free energy of proton adsorption at active sites on the catalyst surface $|\Delta G_H|$, which is the intermediate step of the HER reaction, is an important parameter for comparing catalytic activity. In research conducted by Guo et al. [10], the catalytic performances of 2D MoB and 2D FeB orthorhombic MBene were evaluated and it was found that the $|\Delta G_H|$ value of 2D FeB was close to 0 (Figure 1.8). This indicates that the interaction between the Fe atom and H on the surface is suitable for electrocatalytic HER. In another study by Zhang et al [14], the single atom catalyst calculations for different transition metals by creating a Mo vacancy on Mo_2B_2 MBene, and as a result, it was observed that the Ni addition causes the $|\Delta G_H|$ value under 1/4 H coverage to −0.09 eV. Since the $|\Delta G_H|$ value is higher than -0.2 eV (between 0.2 and -0.2 eV materials show good catalytic activity) and close to 0 eV (the optimum value for catalytic activity), the Ni single atom doped MoB MBene is a good HER electrocatalyst candidate.

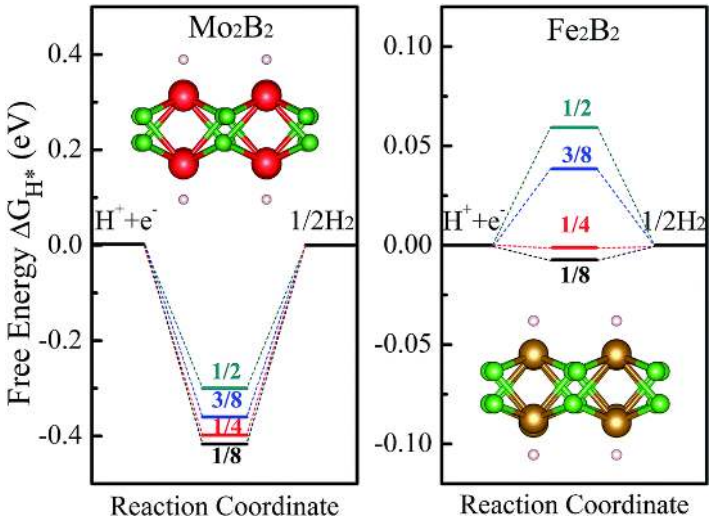

Figure 1.8 Hydrogen coverage-dependent free energy diagrams for 2D MoB and FeB [10].

In the experimental study conducted by Li et al. [63], it was observed that the overpotential of Mo_2AlB_2, synthesized from MoAlB using $CuCl_2$ molten salt, decreased from 410 mV to 145 mV for electrocatalytic HER in 1 M KOH medium as compared to MoAlB. The reason behind this decrease in overpotential is the internal interaction between Mo_2AlB_2 layers, which leads to improved performance. After etching, the active surface area increased, charge transfer resistance decreased, and reaction kinetics improved. In a study by Park et al. [66], MoAlB was etched with NaOH, followed by single atom doping of Pt into the resulting $MoAl_{1-x}B$. The resulting Pt-doped $MoAl_{1-x}B$ exhibited significantly better catalytic activity in acidic and basic environments than both $MoAl_{1-x}B$ and MoAlB. The study's DFT analysis indicated that Mo sites were replaced with doped Pt, leading to an increase in charge density within the *5d* orbital, which improved the catalytic activity for HER. Furthermore, when Pt was added to other 2D materials such as MoS_2 and Mo_2C, HER activity was experimentally shown to be better in MBene.

Chapter 2:
One-Step Synthesis of Metastable Mo_2AlB_2 From MoAlB Using Gaseous HCl

Most of the content in this chapter was published in ACS Inorganic Chemistry, 2025, 64(2), 1139–1145. The original article has been modified and reformatted to meet the structural requirements of this dissertation.

2.1 Introduction

As a member of the MAB phases, MoAlB is the only thermodynamically stable phase in the ternary system Mo–Al–B [39]. In its orthorhombic crystal structure, Mo–B layers are separated from each other by a double layer of Al (Figure 2.1a). In addition, a metastable compound, Mo_2AlB_2, [10] has been obtained with a closely related orthorhombic crystal structure in which only a single Al layer separates the MoB layers (Figure 2.1b). This single-layer configuration makes Mo_2AlB_2 a more suitable precursor for synthesizing 2D MoB [67] (MBene) compared to MoAlB. Therefore, identifying scalable synthetic routes for the metastable Mo_2AlB_2 phase would be advantageous.

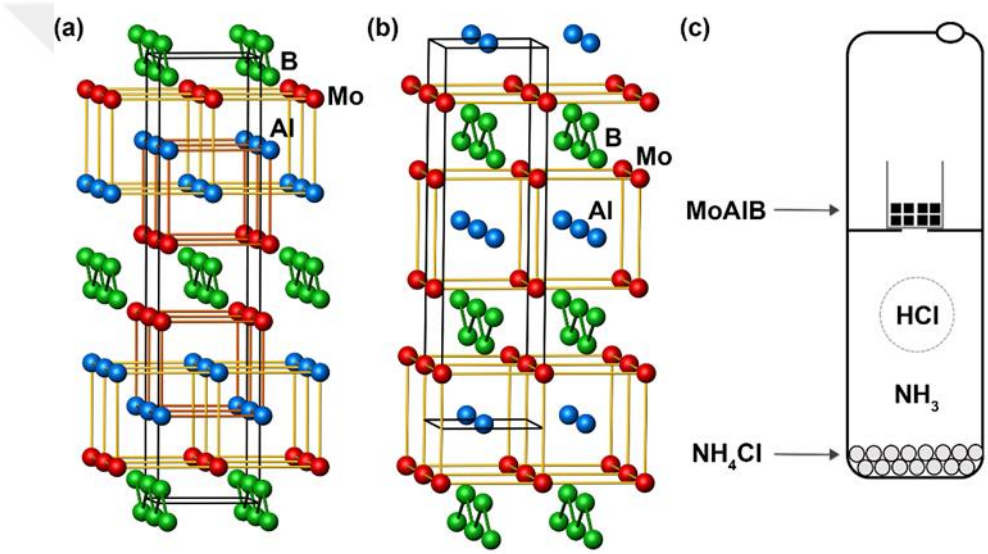

Figure 2.1 Crystal structures of (a) MoAlB (*Cmcm*) [39] and (b) Mo_2AlB_2 (*Cmmm*); (c) Schematic representation of the reactor.

Various methods have been explored to deintercalate Al in MoAlB to obtain Mo_2AlB_2 (Table 2.1). Aqueous solutions of HF and LiF + HCl, although effective at relatively low temperatures, require extended reaction times of up to 48 h, along with additional drying and phase separation steps and involve hazardous chemicals, raising significant health and safety concerns [51, 68]. NaOH-based methods require an additional heat treatment step at 600 °C for 4.5 h, increasing both process complexity and duration [56]. Lewis acid molten salt techniques, like those involving $ZnCl_2$ [61], require high temperatures and post-treatment with aqueous HCl to remove residual Zn nanoparticles. Similarly, $CuCl_2$-based methods demand even higher temperatures and

further washing steps with ammonium persulfate ($(NH_4)_2S_2O_8$) [63]. These methods often involve prolonged reaction times, high temperatures, or extensive postprocessing, highlighting the need for a more efficient, single-step synthesis route.

Table 2.1 Comparative summary of synthesis methods for Mo_2AlB_2, showing experimental techniques and conditions.

Reaction medium	Temperature (°C)	Duration (h)	Additional treatment	Reference
Gaseous HCl	450	2	-	This work
HF solution	45	48	-	[68]
LiF+HCl solution	40	48	-	[51]
NaOH solution	RT	24	Heat Treatment	[56]
$ZnCl_2$ molten salt	550	2	HCl Treatment	[61]
$ZnCl_2$ molten salt	550	170	-	[62]
$CuCl_2$ molten salt	650	2	APS Treatment	[63]

Reactive Zintl phases can be transformed into metastable or otherwise inaccessible stable phases through oxidation with gaseous agents at moderate reaction temperatures [69, 70]. For instance, as an alternative to the well-established high-pressure synthesis of the clathrate-I phase $Ba_{8-x}Si_{46}$, the precursor $Ba_4Li_2Si_6$ was oxidized at low temperature and ambient pressure by reaction with gaseous HCl. The coproducts $BaCl_2$ and LiCl were washed from the product [71]. However, this method has not yet been applied to stable compounds containing d-block elements. Applying this method to convert MoAlB to Mo_2AlB_2 may offer a significant advantage, as the coproduct $AlCl_3$ evaporates, eliminating the need for washing and preventing solvent contamination on the crystallite surfaces.

In this study, we present the conversion of MoAlB to the metastable Mo_2AlB_2 phase through a topochemical synthesis using gaseous HCl in a closed system (Figure 2.1c). This method offers a promising gas–solid reaction pathway that may enable the direct synthesis of 2D MBene materials from other MAB phases. By addressing key challenges in the stabilization and exfoliation of hybrid bonded structures, this approach offers a scalable and efficient route for developing MBenes, opening avenues for their broad application in fields such as catalysis and energy storage.

2.2 Experimental Methods

2.2.1 Characterization tecniques

The structure and phase analysis were carried out by a Rigaku Mini Flex 600 X-ray diffractometer (XRD) equipped with a Cu Kα radiation (λ = 1.5418 Å). XRD patterns were obtained within the 2θ range of 10–90°, employing a scanning rate of 5° s^{-1}. The morphology was investigated via field emission-scanning electron microscopy (FE-SEM, Zeiss Ultra Plus) connected to an energy-dispersive X-ray spectroscopy (EDX) detector (Bruker XFlash 5010, 123 eV spectral resolution). High-resolution transmission electron microscopy (HR-TEM) images were captured using a Thermo Scientific Talos F200S TEM 200 kV instrument. To gain better insights into the surface composition and oxidation states, X-ray photoelectron spectroscopy (XPS) was conducted using a Thermo Scientific K-Alpha instrument equipped with an Al Kα monochromator source emitting at 1486.6 eV. All XPS spectra underwent correction based on the binding energy of C 1s, set at 284.50 eV. The chemical composition of the prepared powder was analyzed using an Agilent 7700x Inductively Coupled Plasma-Mass Spectrometry (ICP-MS) system.

2.2.2 Synthesis of powders

- **α-MoB powder**

A polycrystalline powder specimen of α-MoB was synthesized via carbothermal reduction [72]. MoO_3 (powder, 99.9% metals basis, Alfa Aesar), B_2O_3 (powder, 99.9% metals basis, Alfa Aesar), and activated charcoal (powder, pure, Sigma-Aldrich) were weighed in stoichiometric amounts under an Ar atmosphere in a glovebox. This mixture was loaded into a hardened stainless-steel vial and sealed. The steel vials were cleaned before by using silica in a sandblaster. High-energy ball milling was employed for 3 h using steel balls of two 1/2″ and four 1/4″ in diameter, with a ball-to-powder weight ratio of 13:1. After milling, the mixture was observed to be homogeneous. The mechanically activated powder was transferred to a graphite crucible and heated at a rate of 8 °C/min to 1450 °C and annealed for 6 h at this temperature. Heat treatment was performed in a horizontal tube furnace under flowing Ar. The resulting product formed according to equation 2.1 was single phase α-MoB according to PXRD (Figure 2.2). The crystallinity of the product was also confirmed by SEM images (Figure 2.3).

$$2MoO_3(s) + B_2O_3(s) + 9C(s) \rightarrow 2MoB(s) + 9CO(g) \quad (2.1)$$

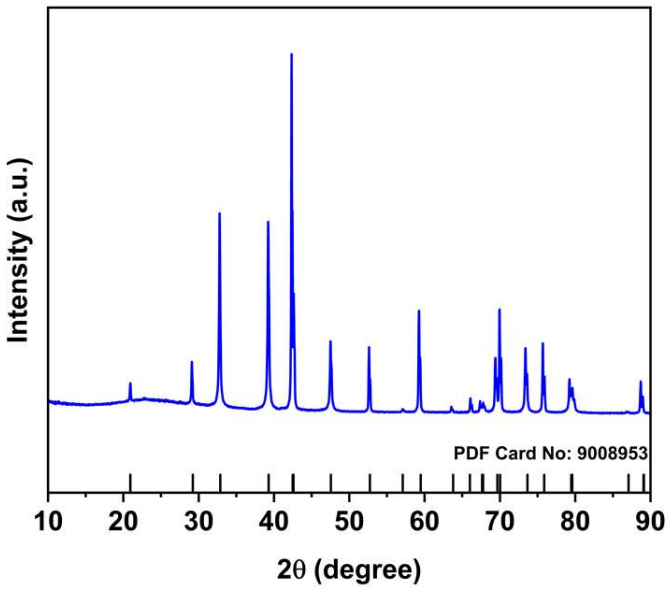

Figure 2.2 PXRD Pattern of α-MoB obtained from carbothermal reduction.

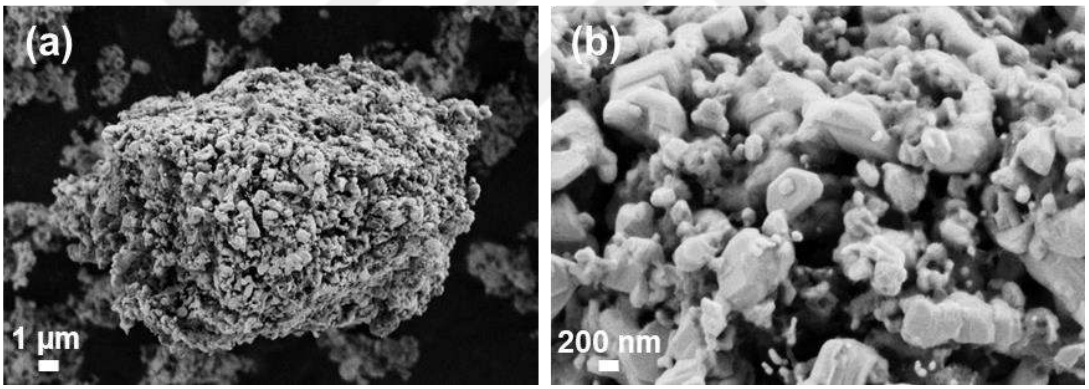

Figure 2.3 SEM images of the α-MoB with (a) low and (b) high magnification (SE contrast).

- **MoAlB powder**

MoB and Al (powder, 99.5% metals basis, Alfa Aesar) were weighed in a 1:1.6 ratio under an Ar atmosphere in glovebox and transferred in a hardened stainless-steel vial. To homogenize the powder mixture, high-energy ball milling was performed for 5 min using two 1/4″ diameter steel balls with a ball-to-powder ratio of 3:1. Subsequently, the mixture was pressed into a pellet with a diameter of 10 mm by applying 5 tons of force. The pellet was placed in an alumina crucible and heated in a horizontal tube furnace at a rate of 8 °C/min to 1200 °C and annealed for 1 h at this temperature under constant Ar flow. After

the reaction, the pellets were removed from the furnace and ground into powder using a tungsten carbide mortar for 30 min. The resulting product was found to be single phase according to PXRD (Figure 2.4). SEM images of the MoAlB product show microcrystals with nonuniform particle size distribution (Figure 2.5).

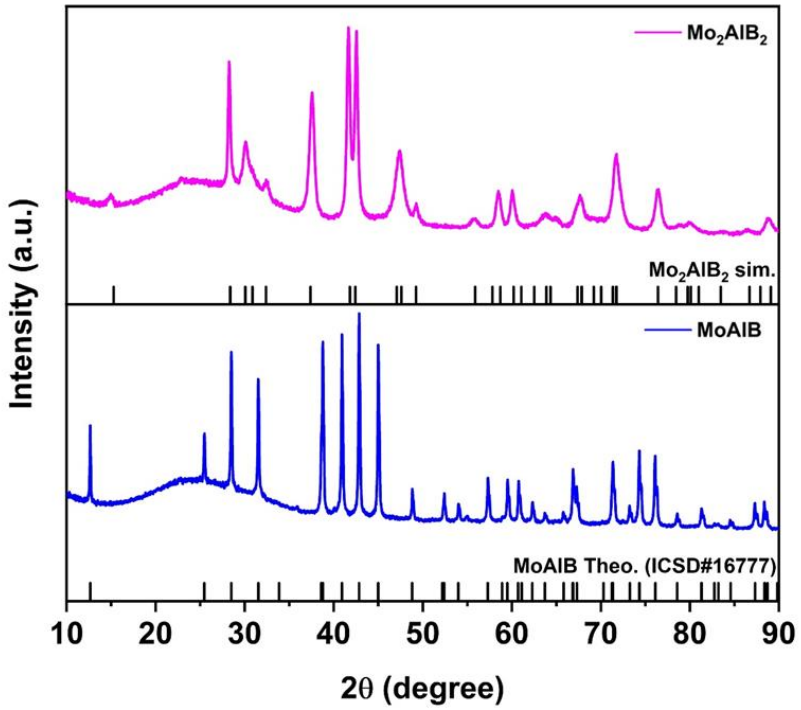

Figure 2.4 Comparison of the precursor phase MoAlB obtained from solid state reaction (blue pattern) and Mo_2AlB_2 obtained after 2h reaction with gaseous HCl at 450°C (pink pattern). The low-temperature reaction leads to a lower crystallinity and broader reflections.

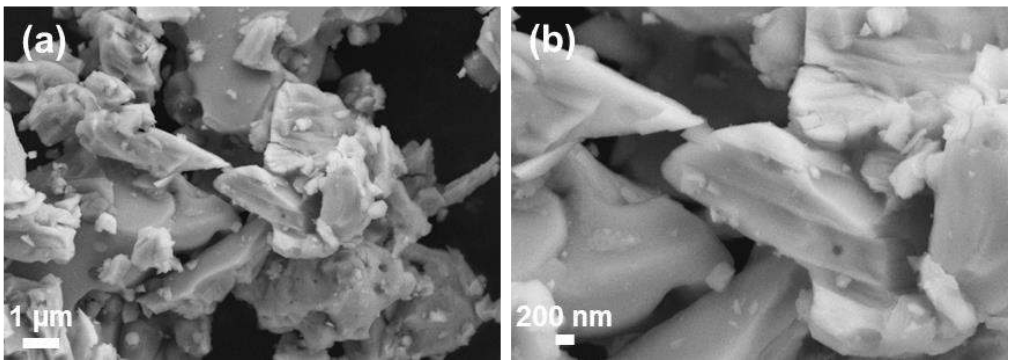

Figure 2.5 SEM images of MoAlB with (a) low and (b) high magnification (SE contrast).

- **Mo_2AlB_2 powder**

To prepare Mo_2AlB_2 using HCl solutions, 0.2 g of MoAlB powder was initially mixed with 50 mL of HCl at varying concentrations ranging from 1 to 3 M for durations of 1 to 6 h. The mixture was then centrifuged to separate the solid phase, and the resulting powder was washed with deionized (DI) water until the solution reached a pH of 7. Finally, the powder was washed with ethanol and dried in a vacuum oven at 60 °C for 12 h.

For the synthesis with gaseous HCl, all steps aside from sealing and washing were conducted under a protective Ar atmosphere in a glovebox. For this process, 1 mmol of MoAlB and 2 mmol of NH_4Cl (99.5%, Sigma-Aldrich) were weighed and MoAlB was placed in an 8 mL glass vial. Prior to use, NH_4Cl was dried at 150 °C for 2 h in a Pyrex glass crucible under vacuum. The vial was then positioned in a glass reactor, which was promptly sealed under vacuum together with NH_4Cl (Figure 2.1c and Figure 2.6). The sealed reactor was inserted into a steel tube, insulated with glass wool at both ends, and positioned in a vertical furnace. Heat treatment was applied at temperatures between 375 and 450 °C (heating rate: 3 °C/min) for 30 to 120 min. After heating, the samples were slowly cooled by turning off the furnace. Upon reaching room temperature, the reactor was opened, and the samples were washed with DI water and ethanol, then dried in a vacuum oven at 60 °C for 12 h.

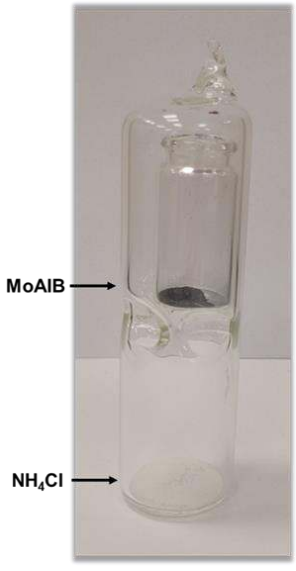

Figure 2.6 The experimental setup used for the production of Mo_2AlB_2 from MoAlB by gaseous HCl.

2.3 Chemical Characterization

To examine the impact of aqueous HCl on MoAlB, etching experiments were conducted using 1 and 3 M HCl solutions at various temperatures and durations, focusing on their effects on the phase formation (Figure 2.7). Initial trials with 1 M HCl revealed significant alterations in the XRD patterns, pointing to notable structural changes. Extended tests with both 1 and 3 M HCl for 6 h further explored temperature effects on these modifications. The (0k0) reflections, related to the stacking of MoB and Al layers, displayed shifts, broadening, or complete disappearance, [73] indicating disruptions in the long-range order along the [0k0] crystallographic direction, likely due to stacking faults caused by the etching process [56]. These observations imply reduced crystalline coherence, increased defect formation, and stacking disorder, underscoring the impact of HCl etching on structural integrity.

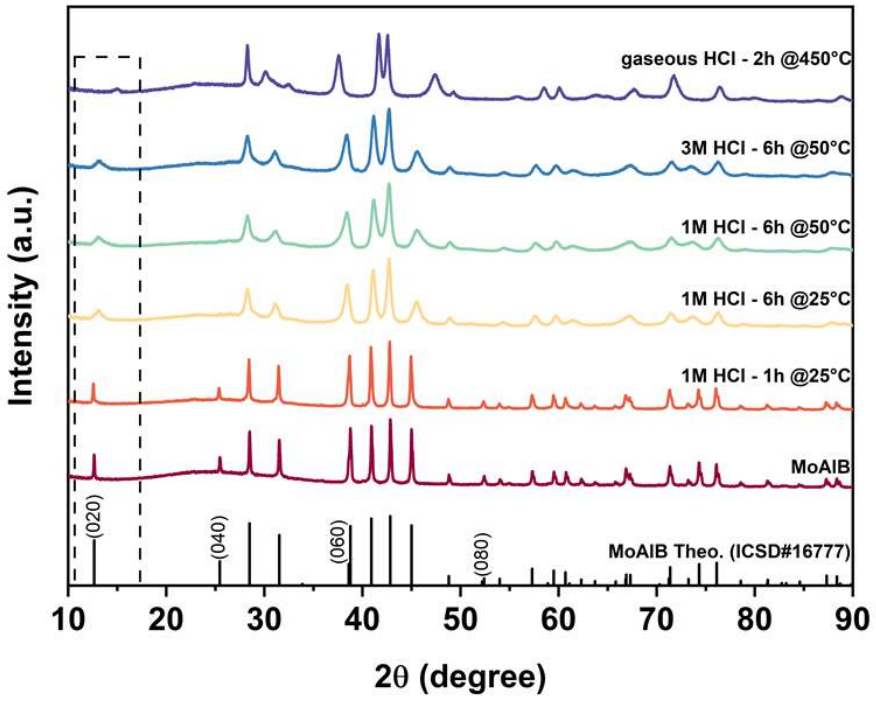

Figure 2.7 PXRD patterns of MoAlB samples treated with HCl under various conditions, with the gaseous HCl experiment displayed at the top. The hatched area highlights peak positions corresponding to the (020) plane.

Further insights were gained by comparing peak positions, particularly for the (020) plane, as highlighted in Figure 2.7. In tests conducted with 1 M HCl for 1 h, no significant changes were observed apart from peak broadening. However, extending the duration to

6 h caused a peak shift for the (020) plane to approximately 13°, alongside amorphization, likely corresponding to intermediate $MoAl_{1-x}B$ phases, such as $Mo_4Al_3B_4$, identified by Kim et al. [51] and supported by Alameda et al., [67] who noted the formation of phases like $Mo_6Al_5B_6$, $Mo_4Al_3B_4$, and $Mo_3Al_2B_3$ during chemical etching. Notably, neither higher temperatures nor increased HCl molarity significantly affected the diffraction pattern in the liquid−solid reactions. To investigate the resulting composition after 6 h HCl treatment, SEM-EDX analysis was conducted (Table 2.2), revealing an approximate atomic ratio of *n*(Mo):*n*(Al) = 1.5, indicating that the transformation from MoAlB to Mo_2AlB_2 was not complete.

Table 2.2 Atomic percentages of $MoAl_{1-x}B$ samples treated with 1M HCl for 6 hours at 25 °C, as determined by SEM-EDS analysis.

Element	at.%
Molybdenum	56.33
Aluminum	36.39
Boron	7.28
Total	**100.00**

Due to the limited success of the solution-phase HCl etching experiments, we shifted to using gaseous HCl to investigate its efficiency in facilitating the transformation. Thus, the precursor phase MoAlB and NH_4Cl were reacted at temperatures ranging from 375 to 450 °C. At these temperatures, NH_4Cl is completely decomposed into HCl and NH_3 [74]. Since the reactants are spatially separated within the reactor (Figure 2.1c), the reaction solely occurs via the gas phase, thus constituting a heterogeneous gas−solid reaction. Primarily, HCl reacts with MoAlB (Equation 2.2):

$$4MoAlB(s) + 6HCl(g) \rightarrow 2Mo_2AlB_2(s) + 2AlCl_3(g) + 3H_2(g) \qquad (2.2)$$

The reaction temperatures required for the transformation of MoAlB are surprisingly low: higher temperatures were required for the oxidation of the reactive Zintl phase $Ba_4Li_2Si_6$ to $Ba_{8-x}Si_{46}$ applying the same method [71]. An important driving force for the reaction of MoAlB with HCl is likely the formation of gaseous $AlCl_3$. Gaseous NH_3, which is the other component in the gas phase, may act as a protic oxidizing agent as well [75].

For all reaction temperatures, the crystalline reaction product only consisted of Mo_2AlB_2, according to PXRD (Figure 2.8). The comparative analysis of the gaseous HCl experiments with those utilizing HCl solutions reveals significant alterations in reflection positions, alongside the emergence of new peaks, indicating a distinct impact of the gaseous environment on the structural transformations of MoAlB (Figure 2.7). All reflections were indexed using the structure model obtained by Zhou et al. through quantum chemical optimization [76]. The pronounced reflection broadening observed in the diffraction patterns is expected for a low-temperature conversion, which typically results in low crystallinity. In addition, a complex arrangement of crystalline domains can cause dramatic line broadening. In this respect, the characteristics of the diffraction patterns are reminiscent to the highly complex γ-Al_2O_3 structure [77-79]. A simple Rietveld refinement did not allow us to obtain a reliable structure model. Lattice parameters were determined approximately based on 25 reflections (Table A1 and Table 2.3). The refinement revealed that reflections of lattice planes nearly perpendicular to the stacking axis show the largest deviation in 2θ. Therefore, it is possible that in the real microstructure, some of the Al double layers are still present, separating ideal crystalline domains above and below, which mostly affects the b cell parameter.

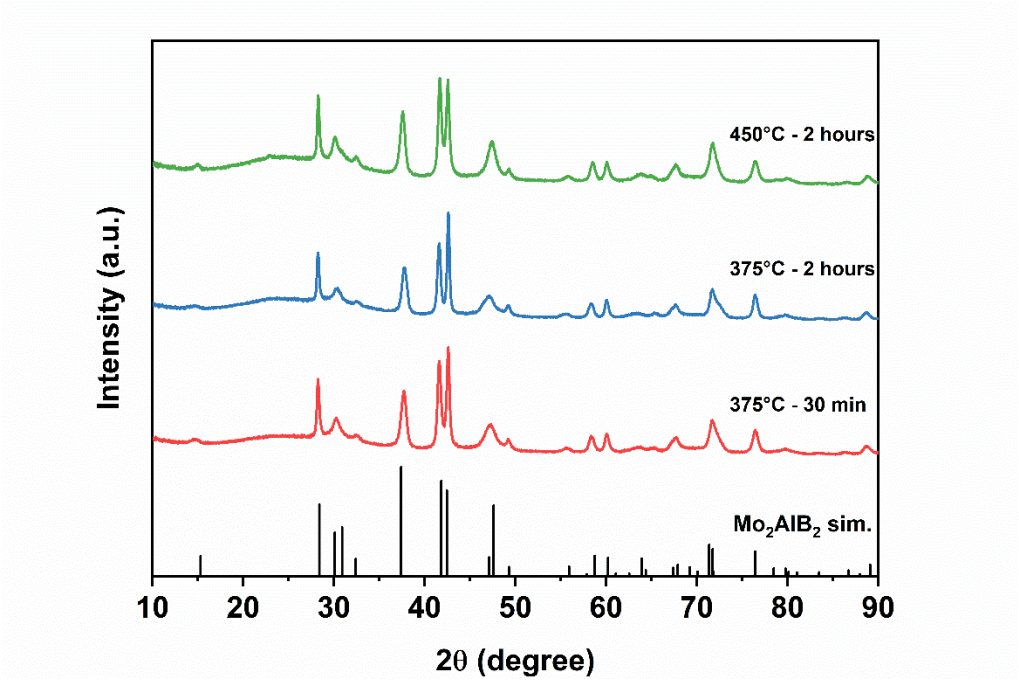

Figure 2.8 Mo_2AlB_2 products obtained from the reaction of MoAlB and gaseous HCl at different annealing conditions.

Table 2.3 Lattice parameters of Mo_2AlB_2 (space group *Cmmm*) in comparison with literature values.

a (Å)	*b* (Å)	*c* (Å)	reference
3.080(3)	11.57(1)	3.149(4)	this work
3.0610(2)	11.4200(8)	3.1428(1)	exp [80]
3.07	11.5	3.18	exp [56]
3.079	11.520	3.144	exp [61]
3.06	11.5	3.18	sim [68]
3.0710	11.5706	3.1413	sim [76]
3.0747	11.4619	3.1703	sim [61]
3.078	11.551	3.148	sim [10]
3.08914	11.63432	3.12544	sim [81]

The lattice spacing for Mo_2AlB_2 was further investigated by HR-TEM, indicating that the structure model originally proposed by Guo et al. is valid, [10] at least within separate crystalline domains (Figure 2.9a). The interlayer spacing corresponding to the (020) plane is reduced from 7.2 Å in MoAlB to 6.2 Å in Mo_2AlB_2 (Figure 2.9b and Figure A1). These results are consistent with the XRD findings (Figure 2.4 and Table A1), which show the 2θ angle of the (020) plane shifting from 12.66° to 14.99°, indicating a decrease in the interlayer distance from 6.99 to 5.91 Å. Additionally, the HR-TEM image of Mo_2AlB_2 reveals d-spacings of 2.4 Å (2.41 Å in XRD) and 1.9 Å (1.91 Å in XRD) corresponding to the (130) and (131) planes, respectively (Figure 2.9c,d).

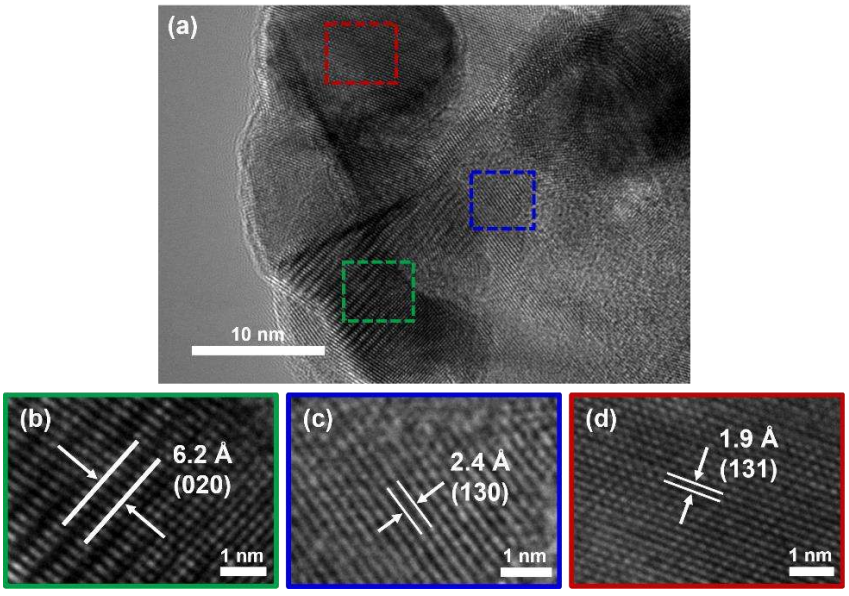

Figure 2.9 HR-TEM images of (a) Mo_2AlB_2 with different d spacings corresponding to (b) (020), (c) (130), and (d) (131) planes.

SEM images (Figure 2.10) show the homogeneity of the product, confirming that the conversion from MoAlB to Mo_2AlB_2 can be favorably performed in a one-step gas−solid reaction. After reaction at 375 °C for 30 min (Figure 2.10a), the particle surface appears highly porous. When the heat treatment was extended for 2 h (Figure 2.10b), the products consisted of small, plate-like crystallites with smooth surfaces containing etch cavities. Heat treatment at 450 °C for 2 h revealed similar characteristics but improved crystallinity (Figure 2.10c,d).

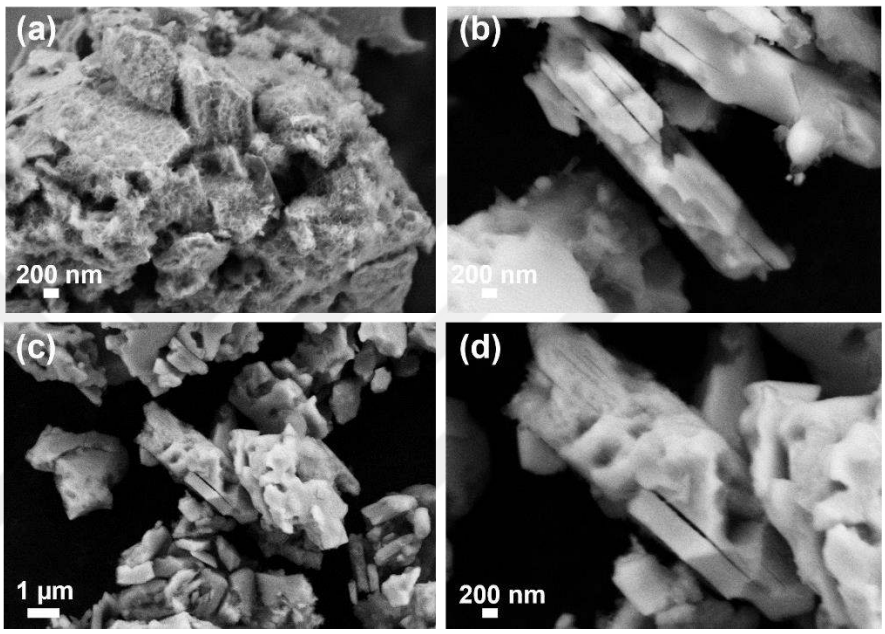

Figure 2.10 SEM images of Mo_2AlB_2 treated at 375 °C for (a) 30 min and (b) 2 h and at 450 °C for 2 h at (c) lower magnification and (d) higher magnification.

EDX revealed the expected signals of Mo, Al, and B, but also of Si, C and O (Figure 2.11a). The Si signal is attributed to impurities from the glass ampule or residues of silica sand used to clean the stainless-steel vials, while the C signal stems from the carbon tape of the sample holder and O to surface oxidation. The distribution of the majority components Mo, Al, and B in the sample is homogeneous (Figure 2.11b,c). A quantitative analysis of light elements such as boron is not reliable by EDX, moreover the arbitrarily oriented grains only allow for an estimation, but the determined atomic ratio of n(Mo):n(Al) ≈ 2.5 roughly corresponds to Mo_2AlB_2 (Table 2.4). From ICP-MS analysis the composition of the product was determined to be n(Mo):n(Al):n(B) = 2:0.8:1.8.

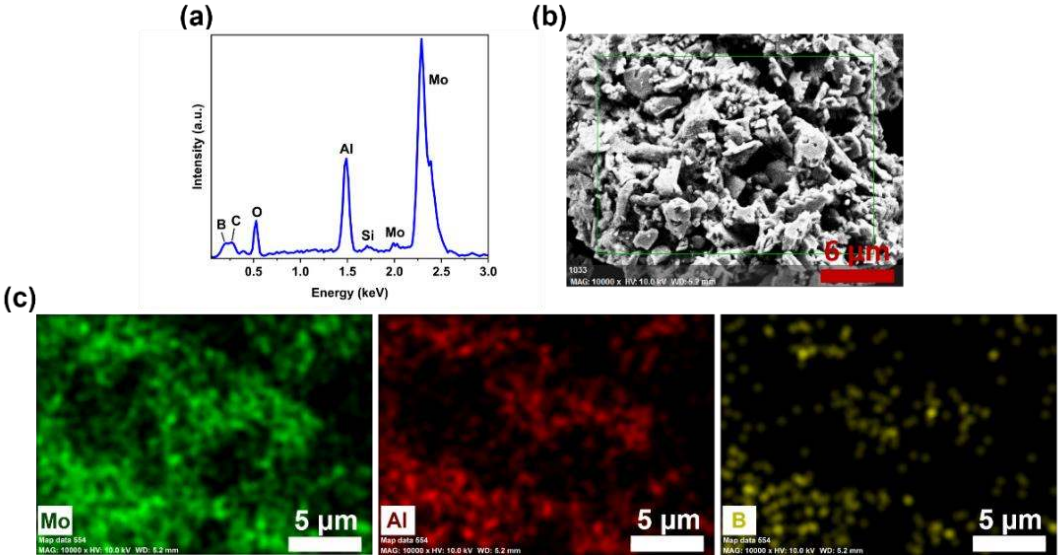

Figure 2.11 SEM-EDX investigation of Mo_2AlB_2. (a); EDX spectrum; (b) image with SE contrast; (c) elemental mapping of Mo, Al, and B.

Table 2.4 Atomic percentage of Mo_2AlB_2 from SEM-EDX.

Element	at.%
Molybdenum	70.87
Aluminum	28.50
Boron	0.63
Total	**100.00**

X-ray photoelectron spectroscopy (XPS) for MoAlB and Mo_2AlB_2 supports the EDX results (Figure 2.12). The spectra were fitted to Mo 3d, Al 2p, and B 1s states. In the Mo 3d spectrum of MoAlB, three sets of doublets are observed at 226.94, 228.18, and 231.74 eV, corresponding to the Mo−Al−B, Mo^{3+}, and Mo^{5+} states. For Mo_2AlB_2, the peaks are located at 228.51, 230.64, and 232.53 eV and are attributed to the Mo−Al−B, Mo^{4+}, and Mo^{6+}, respectively [82]. The shift to higher binding energy by nearly 1.5 eV for MoAlB and the increase in oxidation states of Mo might be explained by the lower Al content, which causes a change in the valence state of Mo. The Al 2p spectra of MoAlB showed three individual peaks assigned to elemental Al, MoAlB, and Al_2O_3 at binding energies of 71.78, 73.89, and 74.92 eV, respectively [83, 84]. Metallic Al is observed because excess Al is used in the synthesis of MoAlB to compensate for the loss of Al during synthesis due to high-temperature volatilization [85, 86]. The Al 2p signals for Mo_2AlB_2 were deconvoluted at 74.22, and 75.11 eV, corresponding to Mo_2AlB_2, and Al_2O_3. The decrease in the peak area in the high-resolution spectra of Al 2p of Mo_2AlB_2 compared

to MoAlB (Figure 2.12 and Figure A2) can be considered evidence of partial deintercalation of Al. The fitted curve of the B 1s states for MoAlB and Mo_2AlB_2 resulted in binding energies of 187.7 and 188.17 eV, respectively. Additionally, signals corresponding to boron suboxide (B_6O) and B_2O_3 are detected in both MoAlB and Mo_2AlB_2. The binding energies associated with boron suboxide are observed at around 190 eV, while the binding energies corresponding to B_2O_3 were identified at 191.73 eV for MoAlB and 191.13 eV for Mo_2AlB_2 [87].

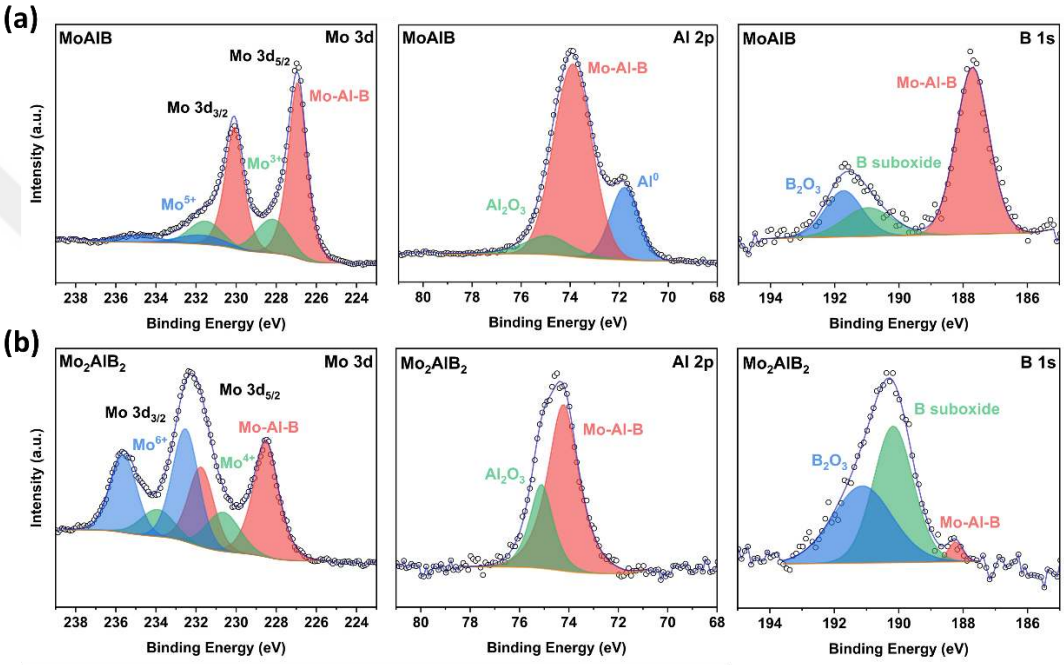

Figure 2.12 High-resolution XPS spectrum for Mo, Al, and B elements of (a) MoAlB and (b) Mo_2AlB_2.

The XPS spectra for both MoAlB and Mo_2AlB_2 reveal multiple oxidation states of molybdenum, along with the presence of aluminum and boron oxides, suggesting significant surface oxidation of the fine powders exposed to air after synthesis [88]. The washing process with deionized water and ethanol may have further contributed to this surface oxidation. Washing was performed before the XPS experiments to make sure that a possible precipitation of $AlCl_3$ in the closed reactor does not contaminate the sample surface. Notably, PXRD analysis didn't show crystalline oxide or $AlCl_3$ peaks, indicating that the oxidation is primarily limited to the surface and does not significantly impact the bulk phase. To mitigate these effects, conducting the reaction in flowing HCl would eliminate the need for washing and potentially reduce surface oxidation.

The approach introduced herein is particularly relevant for the transformation from MoAlB to Mo_2AlB_2, wherein a critical step involves breaking the Al−Al bond by removing a single layer of aluminum using gaseous HCl. Given the structural similarity between e.g., WAlB and MoAlB, both classified as $M_2Al_2B_2$ type MAB phases [40], aluminum deintercalation could also be feasible for WAlB, suggesting the possibility of a similar transformation. Bond strength comparisons reveal that the energy required to break the Al-Al bond falls within the capabilities of gaseous HCl [10], facilitating the transformation from $M_2Al_2B_2$ to M_2AlB_2.

2.4 Conclusions

In this study, we successfully applied a one-step gas-solid reaction to synthesize the metastable MAB phase Mo_2AlB_2, a method previously used for reactive Zintl phases and now adapted for d-block element compounds. This approach, using NH_4Cl to generate gaseous HCl in situ, enables a straightforward and scalable synthesis route, efficiently removing aluminum as $AlCl_3$ without requiring additional drying or separation. Compared to other methods such as aqueous HF, HCl, and NaOH solutions or high-temperature molten salt approaches, this gaseous HCl method operates at lower temperatures, reduces process complexity, and overcomes key limitations of existing techniques. The versatility and efficiency of this gas−solid synthesis pave the way for broader applications in, e.g., catalysis, energy storage, and beyond. As a simple and adaptable process, it serves as a valuable foundation for the development of 2D materials from MAB phases, holding significant potential for upscaling and expanding the accessibility of other layered 2D materials.

Chapter 3:
Hybrid Metal–Organic Framework/MBene Nanostructures Featuring Active Ni Sites for Boosted Hydrogen Evolution in Alkaline Media

Most of the content in this chapter was published in ACS Applied Nano Materials, 2025, 8(30), 15150–15164. The original article has been modified and reformatted to meet the structural requirements of this dissertation.

3.1 Introduction

Earth-abundant transition metal-based materials, including metal-containing oxides [89], hydroxides [90], chalcogenide [91], carbides [92], nitrides [93], phosphides [94], borides [87], and MOFs [95], have emerged as promising electrocatalysts due to their low cost, durability, and activity. MOFs, composed of metal nodes (e.g., Ni, Zr, Cu) connected by organic linkers, offer ultra-high porosity, large surface area, and structural tunability [96]. These properties have promoted their application in energy storage and conversion technologies, including fuel cells, supercapacitors, batteries, and electrochemical water splitting. However, the inherently poor electrical conductivity and structural instability of MOFs limit their direct use as HER catalysts [97]. To harness the high surface area and tunable architecture of MOFs for practical electrocatalytic applications, significant efforts have been dedicated to improve their performance under relevant operating conditions [98-100]. To achieve this, several structural strategies have been developed to enhance catalytic activity, stability, and active site tunability. These include incorporating macrocyclic active domains into MOF structures, where the metal coordination environment can be precisely controlled [98, 101, 102] - as well as inducing phase transitions [103], introducing heteroatom dopants [104], and forming composites with 2D materials [105].

Unlike MXenes, which often require fluoride-based etching and are limited to hexagonal structures, MBenes, such as MoB offer a more flexible and safer synthesis route, thanks to the lower bond strength of metal–boron compared to metal–carbon or metal–nitrogen [11]. This allows the selective removal of Al layers using simple acids like HCl at room temperature [55]. Moreover, MBenes exhibit higher surface activation energies, enabling easier modification of surface groups and stronger interaction with electrolyte ions, which benefits charge transport and overall catalytic activity. The structural versatility of MBenes — including orthorhombic and tetragonal phases — further expands their potential beyond conventional MXenes [106]. To date, only a few studies have explored such MBene composites, primarily for applications beyond catalysis. For example, a moss-like two-dimensional MBene-Ni/Co bimetallic metal-organic framework composite was recently reported as an efficient cathode material for alkaline zinc batteries, leveraging the favorable electrical conductivity and structural

stability of MBenes [107]. However, the electrocatalytic potential of MOF/MBene systems remains largely unexplored. While several MOF/MXene hybrids, such as layered MOFs on $Mo_2Ti_2C_3$ [108], MOFs on delaminated V_2C [109] and Fe/Ni-BTC MOFs decorating Ti_3C_2 MXene [110] have demonstrated enhanced electrocatalytic performance, their broader applicability is hindered by the harsh and selective etching processes required for MXene synthesis.

Most electrocatalysts are fabricated in powder form and applied to electrodes via two main approaches [111]. The first involves coating a conductive substrate (e.g., FTO, ITO, or glassy carbon) with a catalyst ink containing binders like Nafion; while this improves adhesion, it can increase resistance and limit conductivity [112]. Additionally, bubble formation during HER can damage the coating, reducing its performance [113]. Alternatively, directly growing catalysts on porous, conductive substrates like nickel foam (NF) offers enhanced electron transport, mechanical robustness, and improved active site utilization [111]. In previous study, in situ growth of Ni-BDC MOF nanocomposites on NF demonstrated promising HER activity by increasing structural stability and active site density [95]. Similarly, composites such as NiFeLDH/$Mo_{4/3}B_{2-x}T_z$ [114] and Pt single atom-doped $MoAl_{1-x}B$ [66] have shown excellent catalytic performances when integrated with NF.

Building on these advances, this study explores a novel nanocomposite combining Ni-BDC MOF and MoB MBene to enhance electrocatalytic HER performance in alkaline media. The integration benefits from the intrinsic catalytic activity of Ni-BDC and the superior structural and electronic properties of MoB. Strong electronic interactions at the Ni-BDC/MoB interface promote efficient charge transfer, resulting in significantly improved catalytic behavior.

3.2 Experimental Methods

3.2.1 Catalyst Preperation

- **Materials**

Molybdenum(VI) oxide (MoO_3, Alfa Aesar, 99.9 %), boron oxide (B_2O_3, Alfa Aesar, 99.9 %), activated charcoal (C, Sigma-Aldrich, pure), aluminum (Al, Thermo Fisher

Scientific, 99.5 %), zinc chloride ($ZnCl_2$, Thermo Fisher Scientific, > 98%, metal basis), sodium chloride (NaCl, Sigma Aldrich, 99 %), potassium chloride (KCl, Sigma-Aldrich, 99 %), 1,4-benzenedicarboxylic acid (terephthalic acid/1,4-BDC, Sigma-Aldrich, 98 %), N,N-dimethylformamide (DMF, Sigma-Aldrich), nickel nitrate hexahydrate ($Ni(NO_3)_2 \cdot 6H_2O$, Sigma-Aldrich, 99.999 % trace metal basis) were purchased and utilized without any prior treatment.

- **Preperation of MoAlB**

Initially, MoB was prepared by carbothermal reduction using stoichiometric amounts of MoO_3, B_2O_3, and C. The powders were weighed in a glovebox (MBraun Labmaster Pro DP, O_2 and H_2O levels < 0.1 ppm), homogenized and activated via high-energy ball milling for 3 hours, and subsequently loaded into a graphite crucible. The crucible was placed in a horizontal tube furnace, heated to 1450 °C at a rate of 8 °C min^{-1}, and annealed for 6 hours under an Ar atmosphere. The resulting MoB powder and aluminum were then mixed in a molar ratio of 1:1.6 inside an Ar-filled glovebox and transferred into a hardened steel vial. This mixture was homogenized by high-energy ball milling for 5 minutes, pressed into pellets under 5 tons of pressure using a cold press, and subsequently annealed in an alumina crucible at 1200 °C for 1 hour (heating rate: 8 °C min^{-1}) under Ar flow. After natural cooling, the resulting green body was pulverized into a fine powder to obtain the MoAlB phase.

- **Preparation of MoB MBene**

A sustainable molten salt route was employed for the synthesis of high-purity MoB MBene, which offers a scalable and environmentally benign alternative to conventional fluoride-based etching techniques. In a typical procedure, as-synthesized MoAlB, $ZnCl_2$, NaCl, and KCl were weighed in a molar ratio of 1:2:2:2 and thoroughly mixed in an agate mortar for 5 minutes inside an Ar-filled glovebox to obtain a homogeneous powder mixture. The mixture was then transferred into an alumina crucible and placed inside a quartz tube, which was sealed under Ar atmosphere within the glovebox. The sealed quartz tube was heated in a vertical furnace at 700 °C for 2 hours with a heating rate of 5 °C min-1 under continuous Ar flow. After annealing, the naturally cooled blackish powder was sequentially washed and centrifuged with DI water and ethanol to remove

residual salts. The washed product was then immersed in a 5 wt.% HCl solution for 2 hours to further eliminate any remaining metallic impurities, followed by additional washing steps with DI water and ethanol. Finally, the purified powder was dried overnight at 80 °C in a vacuum furnace to obtain the MoB MBene.

- **Preparation of MoB/Ni-BDC/NF nanocomposite**

Commercially available NF was first subjected to a pre-treatment process to remove surface oxides and contaminants. NF pieces (2 cm × 3 cm) were sequentially ultrasonicated in 2.0 M HCl solution, DI water, and ethanol for 15 minutes each, followed by drying under ambient conditions. The pre-treated NF substrates were then stored in an Ar-filled glovebox prior to catalyst deposition. The MoB/Ni-BDC nanocomposite was synthesized on NF via a hydrothermal method. Two solutions were prepared separately: 5 mmol of 1,4-BDC was stirred in 15 mL of DMF for 30 minutes, while 5 mmol of $Ni(NO_3)_2 \cdot 6H_2O$ was dissolved in 15 mL of DI water for the same duration. Afterward, the DMF solution was added instantly into the aqueous $Ni(NO_3)_2 \cdot 6H_2O$ solution and stirred vigorously for an additional 30 minutes to form a homogeneous mixture. This solution was then subjected to ultrasonication for 1 hour, during which MoB MBene powder was introduced at different weight percentages (5–10 wt.%) and dispersed thoroughly, resulting in a dark green suspension. The prepared suspension was transferred into a 50 mL Teflon-lined stainless-steel autoclave containing a pre-treated NF piece. The autoclave was sealed and heated at 180 °C for 24 hours in a furnace. After natural cooling to room temperature, the MoB/Ni-BDC-coated NF samples were thoroughly rinsed with DMF, DI water, and ethanol, and subsequently dried under vacuum at 60 °C for 12 hours. The resulting samples were denoted as MoB-*X*/Ni-BDC/NF, where X = 5, 7.5, and 10 wt.%. For the preparation of pristine Ni-BDC/NF, the same procedure was followed without the addition of MoB MBene powder. A catalyst loading of around 10 mg cm^{-2} was achieved on the NF substrate.

- **Preparation of MoB/Ni-BDC/NF/T**

The as-synthesized MoB/Ni-BDC/NF nanocomposites were annealed using an alumina crucible in the vertical furnace at different temperatures (300 and 400 °C) for 2 hours with a heating rate of 5 °C/min under an Ar atmosphere. The annealed samples

were designated as MoB/Ni-BDC/NF/*T*, where *T* represents the annealing temperature (300 or 400 °C). The catalyst loading on the NF substrates was approximately 5 mg cm^{-2}. To clarify the multi-step synthesis route, a schematic illustration is presented Figure 3.1.

- **Preparation of MoB/NF, MoB/*400*/NF and Pt/C/NF**

MoB MBene powder and Pt/C catalysts were separately deposited onto pre-treated NF substrates using a drop-casting method. For MoB/NF preparation, 5 mg of MoB MBene powder was dispersed in a mixture of 100 μL DI water and 400 μL ethanol by ultrasonication for 30 minutes. Subsequently, 10 μL of Nafion solution was added, followed by an additional 30 minutes of ultrasonication to form a homogeneous ink. The resulting ink was drop-cast onto a pre-treated NF substrate, achieving a catalyst loading of approximately 5 mg cm^{-2}, comparable to the loading of in situ synthesized electrocatalysts. MoB/*400* was also prepared following the same catalyst ink preparation and drop-casting procedure. For Pt/C/NF preparation, the same procedure described in our previous study was applied. Specifically, 5 mg of commercial 20 wt.% Pt/C catalyst was dispersed in a mixture of 400 μL DI water and 600 μL ethanol and ultrasonicated for 30 minutes. Afterward, 20 μL of Nafion solution was added and sonicated for an additional 30 minutes. The prepared Pt/C ink was then drop-cast onto NF to achieve a similar mass loading.

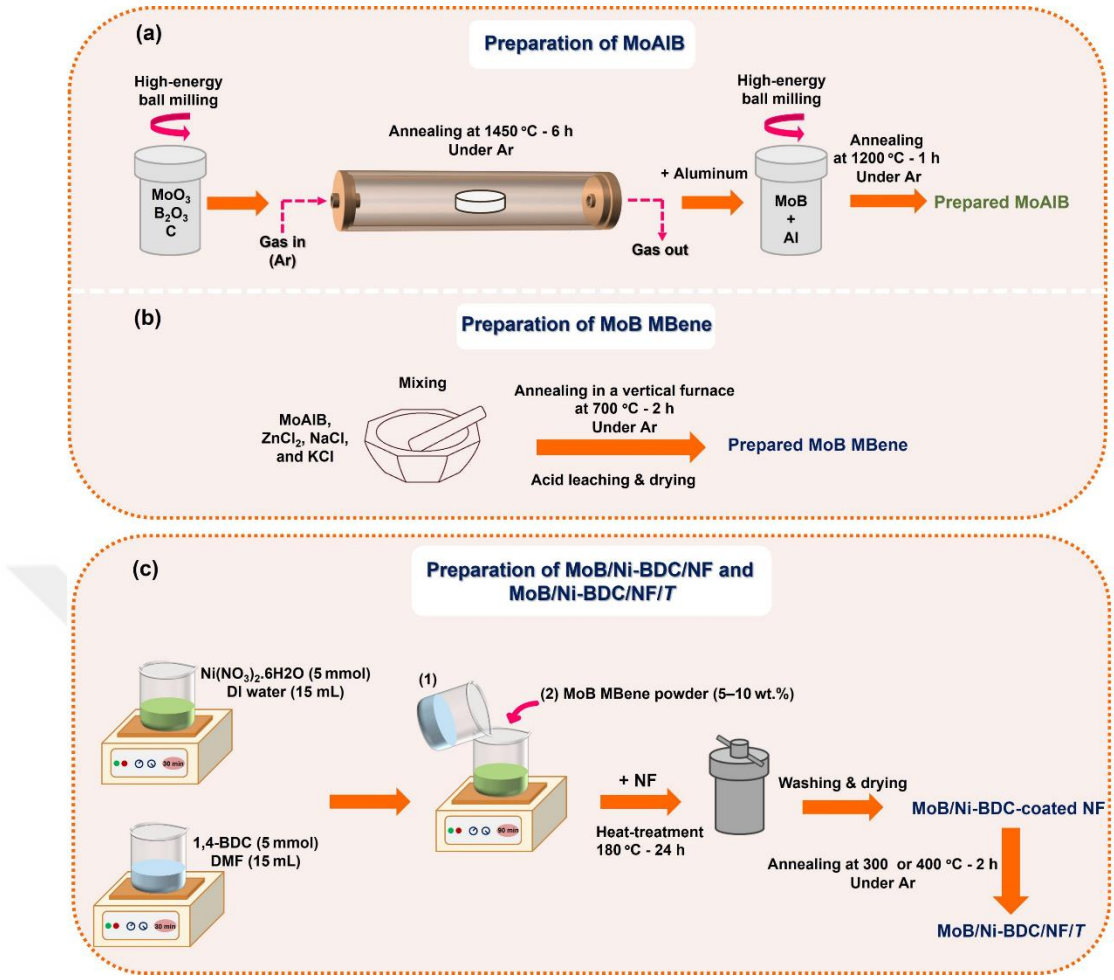

Figure 3.1 Schematic illustration of the synthesis steps: (a) Preparation of layered ternary MoAlB compound via solid-state reaction; (b) Selective etching of Al layers using Lewis acid molten salt to produce MoB MBene; (c) In-situ growth of Ni-BDC MOF integrated with MoB MBene on NF (MoB/Ni-BDC/NF), followed by thermal treatment (MoB/Ni-BDC/NF/*T*).

3.2.2 Materials Characterization

The crystal structure and phase purity of the synthesized materials were investigated using XRD with a Rigaku Mini Flex 600 instrument equipped with Cu Kα radiation (λ = 1.5418 Å). XRD measurements were performed by collecting data over a range of 5 - 90° with a scanning rate of 5°/min. Thermogravimetric analysis (TGA) was carried out on a Netzsch STA 449 Fx-Jupiter instrument, operating under an argon atmosphere with a heating rate of 5 °C/min up to 500 °C, to determine the degradation temperature of the materials. The morphology of the electrocatalysts was examined by a FE-SEM (Zeiss Ultra Plus) employed with an energy-dispersive EDS detector (Bruker XFlash 5010), giving a spectral resolution of 123 eV. The thickness of an individual nanosheet was

measured by atomic force microscopy (AFM) using a Bruker Dimension Icon system. The microstructure and lattice fringes were further explored by HR-TEM (Thermo Scientific Talos F200S 200 kV). The specific surface area was determined by nitrogen adsorption–desorption isotherms using the Brunauer–Emmett–Teller (BET) method with a Micromeritics ASAP 2010 analyzer. The surface composition and oxidation states were analyzed by XPS (Thermo Scientific K-Alpha with an Al Kα monochromator source, 1486.6 eV). All XPS spectra were corrected with respect to the binding energy of C 1s = 284.50 eV.

3.2.3 Electrochemical Characterization

All electrochemical studies were conducted using an AutoLab Potentiostat/Galvanostat instrument (PGSTAT302N, fabricated in the Netherlands) using a typical three-electrode cell in an alkaline condition (1.0 M KOH). As-prepared catalyst on NF (0.5 cm × 1 cm), Pt spring, and standard reversible hydrogen electrode (RHE; HydroFlex) were used as working, counter, and reference electrodes, respectively. To evaluate the electrocatalytic HER performance, the linear sweep voltammetry (LSV) profiles were recorded within the potential window of 0 to -0.8 V at a scanning rate of 5 mV s^{-1}. The HER overpotentials were calculated at a current density of 10 and 50 mA cm^{-2}. The obtained LSV curves were subsequently replotted to achieve Tafel plots. The ECSA analysis relied on the concept of electrochemical C_{dl}, which was determined using CV data collected at various scan rates (0.06 to 0.2 V s^{-1}) between 0.65 and 0.75 V vs RHE. TOF values were calculated at regular 50 mV intervals over the overpotential range of 100 to 400 mV. Chronopotentiometry (CP) test was performed at 10 and 50 mA cm^{-2} current densities for 50 hours to evaluate the long-term HER stability of the best-performing catalyst. An EIS analysis was carried out at a fixed potential of 0.0 V vs. RHE, probing the material's response across a broad frequency spectrum ranging from 100 kHz to 0.1 Hz. All electrochemical data were reported applying a 60% iR correction.

3.3 Chemical Characterization

The XRD pattern of the MoAlB precursor (Figure 3.2a, blue curve) shows sharp and well-defined peaks that match closely with the theoretical MoAlB reference pattern (ICSD-16777), confirming the successful synthesis of highly crystalline MoAlB. After

treatment with a Lewis acid molten salt mixture ($ZnCl_2$/NaCl/KCl) at 700 °C, followed by sequential washing with DI water and dilute HCl to remove residual salts and Zn byproducts, a significant change in the diffraction pattern was observed (Figure 3.2a, red curve). The resulting MoB MBene pattern displays broadened peaks compared to MoAlB, indicating a reduction in crystallinity and/or the formation of nanoscale domains, typical of 2D exfoliated structures. Importantly, the peak corresponding to the (112) plane remains prominent, suggesting a preferred orientation along this direction in the resulting MoB MBene [61]. The mass yield of the final MoB MBene product was gravimetrically determined to be approximately 32%, based on the initial mass of the MoAlB precursor and the dried weight of the etched product. This moderate yield can be attributed to partial dissolution of Zn-based byproducts and unavoidable mechanical loss during repetitive washing and centrifugation steps. XRD analysis confirmed the phase purity of the final product, through which the successful removal of Al layers and formation of MoB MBene were verified.

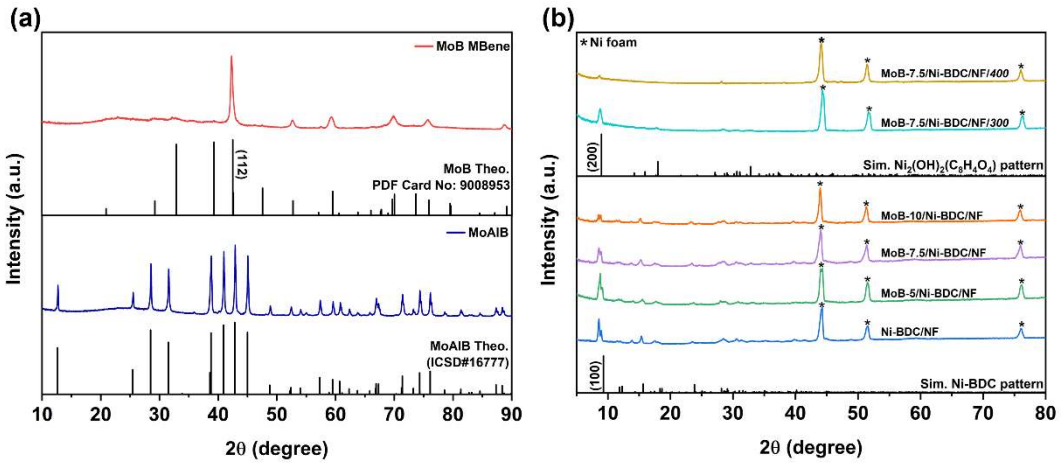

Figure 3.2 XRD patterns of (a) MoAlB and MoB MBene, (b) Ni-BDC/NF and MoB-*X*/Ni-BDC/NF nanocomposites before and after annealing.

A solvothermal reaction was employed to synthesize the MoB/Ni-BDC nanocomposite by simultaneously depositing MoB MBene and forming Ni-BDC on NF. The crystalline phases of the resulting nanocomposites with varying MoB content were characterized by XRD to optimize the composition. As shown in Figure 3.2b, the diffraction patterns of the nanocomposites align closely with the simulated Ni-BDC

pattern prior to any heat treatment, confirming the successful formation of the Ni-BDC phase. In addition to Ni-BDC reflections, intense peaks at 44.3°, 51.7°, and 76.2°, corresponding to the (111), (200), and (220) planes of metallic nickel, are observed due to the underlying NF substrate. With increasing MoB MBene content, a gradual decrease in the intensity of the Ni-BDC (100) reflection is noted, suggesting that MoB incorporation affects the growth or crystallinity of the Ni-BDC structure. No distinct peaks corresponding to MoB are detected, likely due to its low loading, high dispersion within the composite, or peak overlap with the dominant signals from Ni-BDC and NF [115, 116].

Ni-BDC, or nickel terephthalate, with the chemical formula $Ni_3(OH)_2(H_2O)_4(tp)_2$ (tp: $C_8H_4O_4^{-2}$), crystallizes in a triclinic structure and forms infinite layers oriented parallel to the (010) planes [117]. In this framework, nickel chains are connected by two adjacent dicarboxylate linkers, creating a 2D network stabilized predominantly by hydrogen bonds [118]. Due to the relative weakness of hydrogen bonding, the structure is susceptible to thermal-induced transformations. As reported by Mesbah et al., heating to 160 °C results in the removal of two water molecules per unit cell, leading to the formation of $Ni_3(OH)_2(H_2O)_2(tp)_2$ [119]. Upon further heating beyond 210 °C, one Ni(tp) unit and the remaining coordinated water molecules are eliminated, resulting in the transition to a monoclinic $Ni_2(OH)_2(tp)$ structure.

FT-IR spectroscopy was conducted to investigate the functional groups and structural characteristics of the synthesized materials. As shown in Figure 3.3a, the FT-IR spectra of the MoB/Ni-BDC composites closely resemble that of pristine Ni-BDC [95], indicating that the fundamental framework of Ni-BDC is preserved. Distinct peaks at 1377 cm^{-1} and 1579 cm^{-1} correspond to the symmetric and asymmetric stretching vibrations of the $-COO^-$ groups, respectively, confirming the presence of the dicarboxylate linkers within the Ni-BDC structure [120]. The clear separation between these two modes suggests that the $-COO^-$ groups of the para-BDC linker are coordinated to Ni ions in a bidentate mode [121]. A peak around 1530 cm^{-1} is assigned to the stretching vibrations of para-aromatic C–H bonds [121, 122]. Bands observed in the range of 740–850 cm^{-1} are attributed to additional C–H stretching vibrations. Broad absorption features between 3300 and 3600 cm^{-1} are associated with O–H stretching vibrations, originating from coordinated

water molecules or surface hydroxyl groups [121, 123]. Finally, characteristic bands between 400 and 550 cm^{-1} correspond to Ni–O bond vibrations, further confirming the metal–organic coordination environment [122, 124].

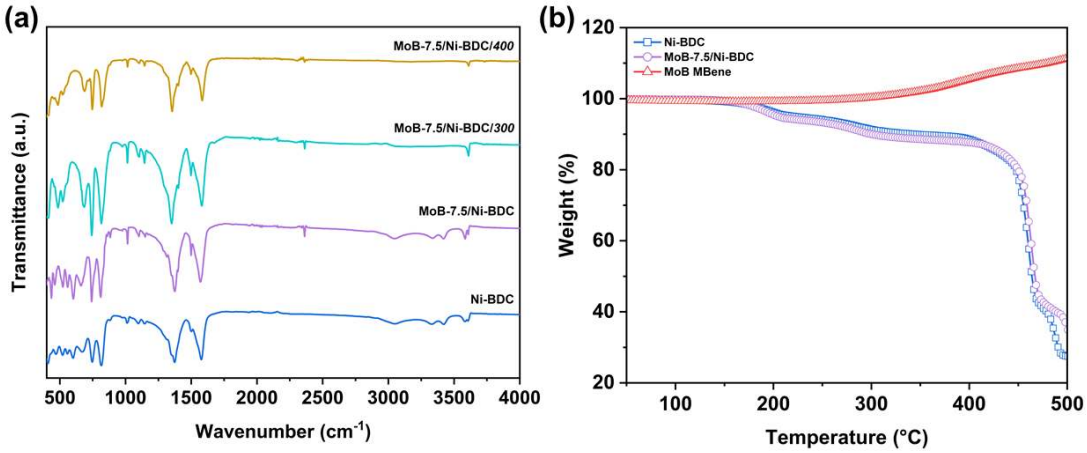

Figure 3.3 FT-IR results of (a) Ni-BDC, MoB-7.5/Ni-BDC, MoB-7.5/Ni-BDC/*300* and MoB-7.5/Ni-BDC/*400* and (b) TGA results of Ni-BDC, MoB-7.5/Ni-BDC, and MoB MBene.

TGA analysis of Ni-BDC, MoB/Ni-BDC, and MoB MBene was performed under an Ar atmosphere to investigate their thermal stability (Figure 3.3b). Ni-BDC exhibited a gradual mass loss up to 450 °C, primarily attributed to the removal of coordinated water molecules and partial decomposition of Ni(tp) units, consistent with structural transformations reported by Sun et al. [125]. Beyond 450 °C, a more pronounced mass loss was observed, corresponding to the dissociation of the organic framework and the formation of Ni nanoparticles. Similarly, the TGA profile of MoB MBene showed a gradual increase in the oxidation rate above 400 °C, indicating its thermal sensitivity at elevated temperatures. A comparable thermal behavior was observed for the MoB-7.5/Ni-BDC nanocomposite, suggesting that both components undergo structural modifications in this temperature range. Based on these observations, annealing treatments were carried out at 300 °C and 400 °C to study the impact of structural evolution in Ni-BDC. As illustrated in Figure 3.2b, the diffraction patterns of MoB-7.5/Ni-BDC/*300* and MoB-7.5/Ni-BDC/*400* match closely with the simulated $Ni_2(OH)_2$(tp) phase, confirming the thermal transformation pathway. Notably, a progressive decrease in the intensity of the (200) reflection was observed with increasing temperature, indicating the gradual breakdown of the layered structure. To further verify Ni nanoparticle formation, XRD

measurements were conducted on powder samples (Figure 3.4a), as the metallic NF initially complicated direct identification. The agreement between the simulated $Ni_2(OH)_2(tp)$ pattern and the experimental data confirms the removal of Ni(tp) units and coordinated water molecules upon annealing. Additionally, the emergence of distinct Ni metal peaks in the sample annealed at 400 °C provides direct evidence of Ni nanoparticle formation, marking the onset of decomposition of the $Ni_2(OH)_2(tp)$ framework. In addition, MoB MBene was annealed at 400 °C under the same conditions to determine its structural stability. As shown in Figure 3.4b, no noticeable changes were observed in its diffraction pattern, which means that the MoB phase remains stable without any structural transformation at the temperature of interest.

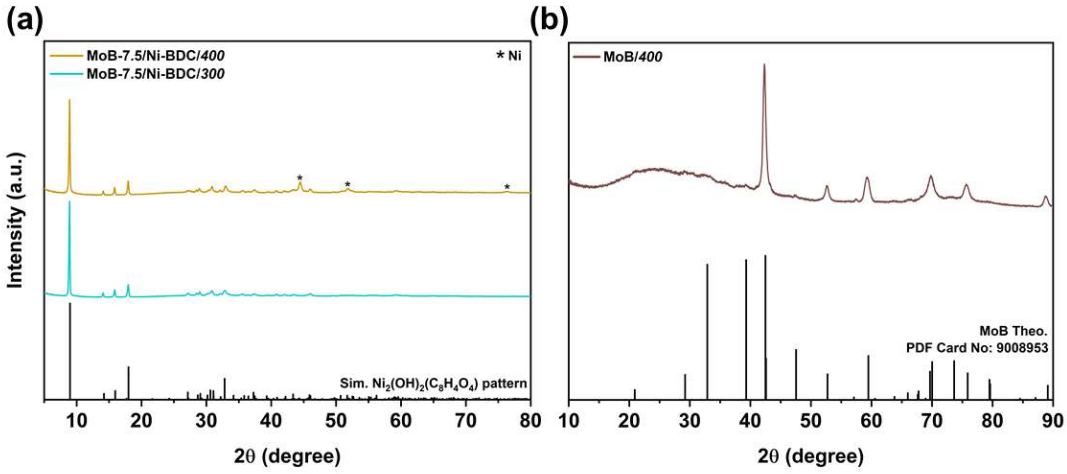

Figure 3.4 XRD pattern of (a) MoB-7.5/Ni-BDC annealed at 300 and 400 °C with the powder form and (b) MoB MBene annealed at 400 °C under Ar atmosphere.

The morphological characteristics of the samples were examined using FE-SEM at various magnifications. As shown in Figure 3.5a and b, the MoAlB precursor exhibited microcrystalline features with a non-uniform particle size distribution. Following the selective removal of Al, the resulting MoB MBene displayed a layered, flake-like morphology (Figure 3.5c and d), distinct from the accordion-like structures typically observed in MXenes [9]. This difference is attributed to nanosheet agglomeration occurring during the high-temperature etching process [61].

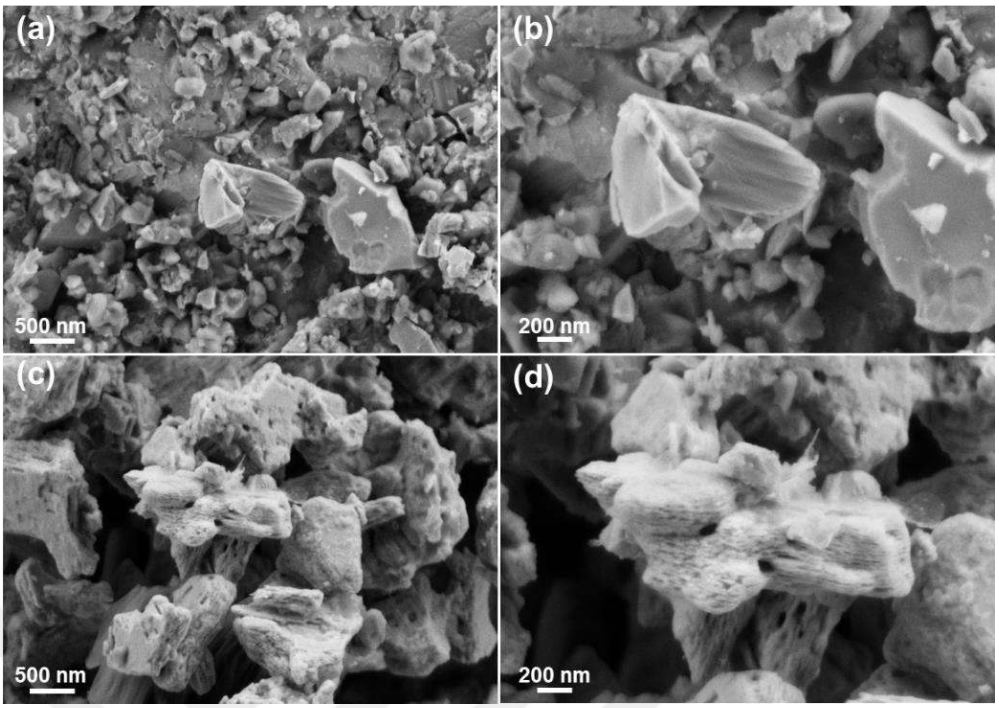

Figure 3.5 SEM images of (a, b) MoAlB and (c, d) MoB MBene powder.

Elemental distribution was analyzed by EDS mapping at different magnifications, confirming a homogeneous distribution of Mo throughout the structure (Figure 3.6a and b). Due to the low atomic number of boron, its detection by EDS is unreliable and was therefore not considered. Despite the HCl washing step, trace amounts of Zn were detected, likely stemming from the use of $ZnCl_2$ as the Lewis acid during synthesis. The Al content, initially measured at approximately 7 at% (Figure 3.6a), decreased to around 3 at% in regions highlighting the layered morphology at higher magnifications (Figure 3.6b), indicating a significant reduction in residual Al between the MoB layers.

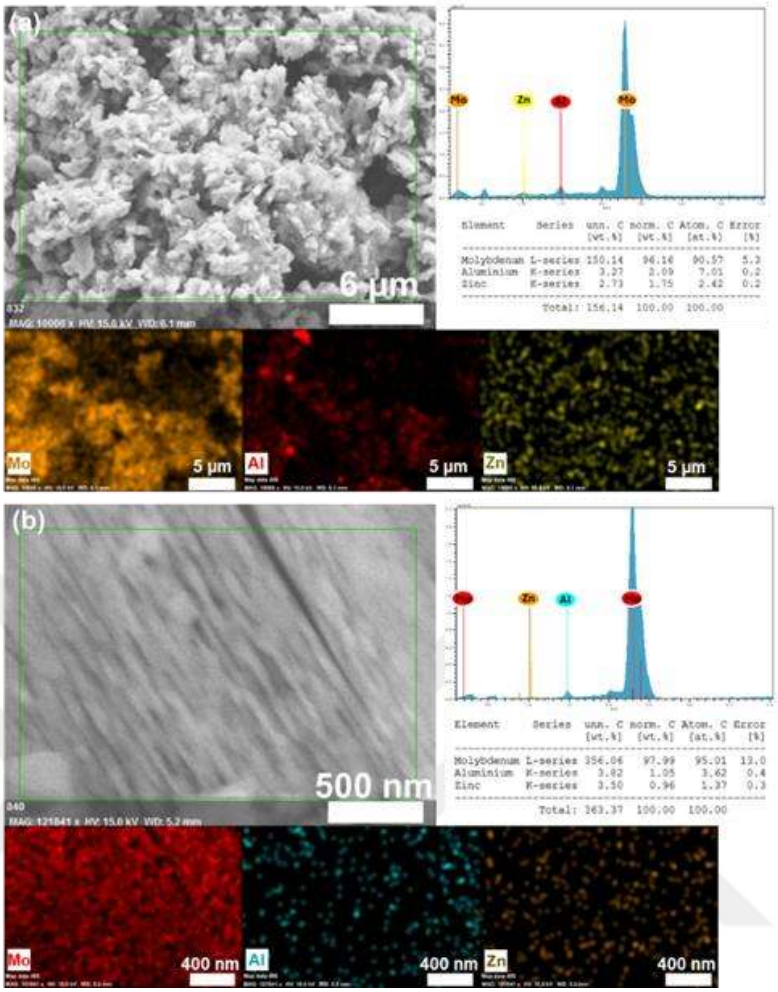

Figure 3.6 SEM-EDS results of MoB MBene at (a) low and (b) high magnification.

To further characterize the nanoscale morphology and thickness of the synthesized MoB MBene, AFM measurements were performed. The results, provided in Figure 3.7, reveal that the MoB MBene nanosheets exhibit an average thickness of approximately 30 nm, based on height profiles taken across different regions of the flakes. Additionally, apparent thickness variations were observed near the edges and corners, where localized values of approximately 20 nm were measured, attributed to stacked, layered regions that persist following selective etching. It is also worth noting that the apparent edge thickness in the AFM images appears higher than that of the interior regions, which is most likely due to wrinkles or bending at the edges of the ultrathin 2D nanosheets. Such features are common in exfoliated 2D materials and arise from the intrinsic flexibility of the sheets combined with the effects of liquid surface tension during sample preparation. These morphological features confirm the successful formation of layered MoB MBene and are

consistent with the structural characteristics expected for incompletely delaminated 2D materials.

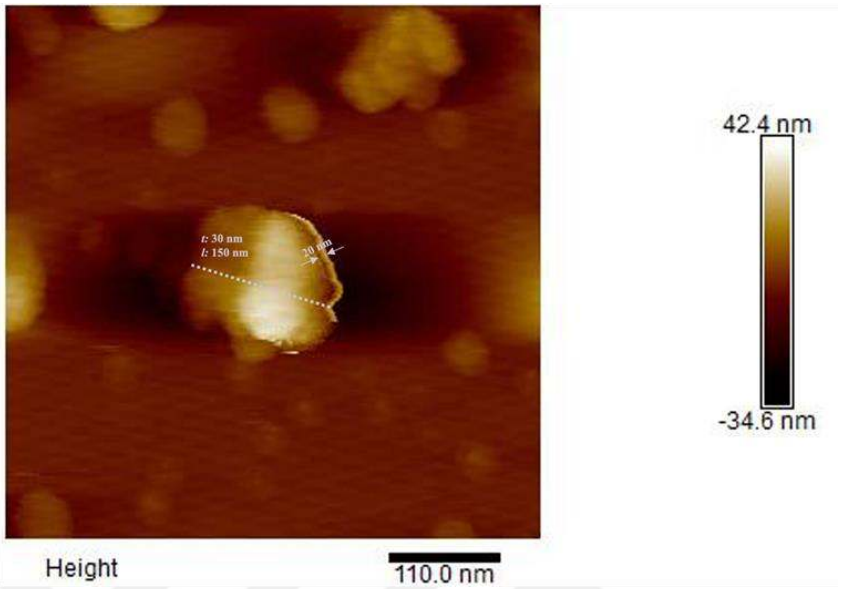

Figure 3.7 AFM images of MoB MBene.

SEM imaging revealed that Ni-BDC deposited on NF forms densely packed, vertically aligned rod-like structures across the foam substrate (Figure 3.8a). In the MoB-incorporated nanocomposites, the introduction of MoB MBene significantly altered morphology. MoB-5/Ni-BDC/NF exhibited a plate-like structure with partially preserved rod features (Figure 3.8b), which evolved into a rough, cauliflower-like morphology as the MoB content increased to 10 wt.%, characterized by larger, aggregated tuberous features (Figure 3.8c and d). This morphological transition suggests that MoB incorporation disrupts the regular crystallization of Ni-BDC, resulting in increased surface roughness and potentially more accessible catalytic sites. The progressive increase in Mo content was corroborated by SEM-EDS analysis, showing a steady rise in the atomic percentage of Mo with higher MoB loading (Figure B1).

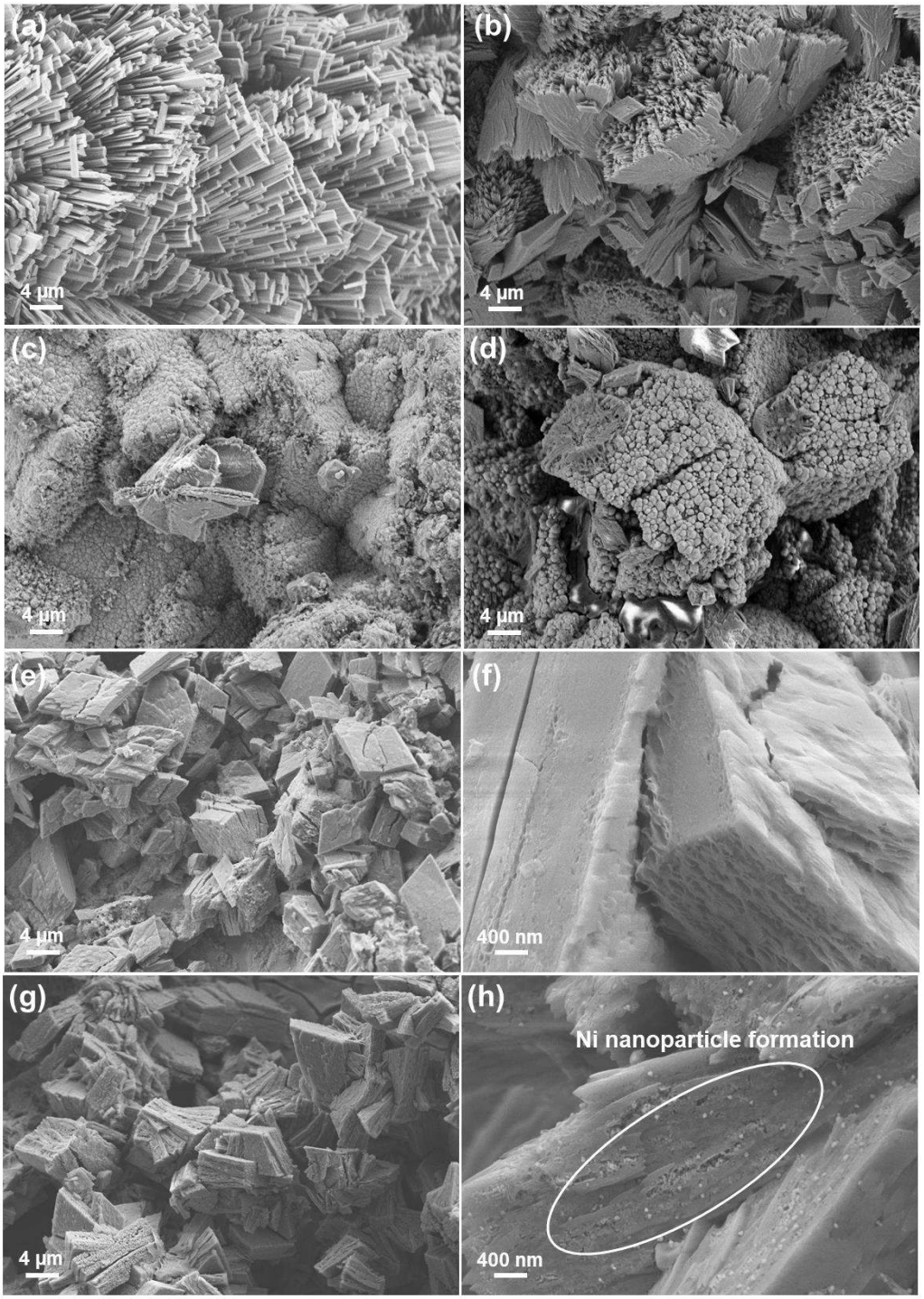

Figure 3.8 SEM images of (a) Ni-BDC/NF, (b) MoB-5/Ni-BDC/NF, (c) MoB-7.5/Ni-BDC/NF, (d) MoB-10/Ni-BDC/NF, (e, f) MoB-7.5/Ni-BDC/NF/*300* and (g, h) MoB-7.5/Ni-BDC/NF/*400* at low and high magnifications.

Upon thermal treatment at 300 °C, a phase transition occurred in the Ni-BDC framework from a triclinic to a monoclinic $Ni_2(OH)_2(tp)$ structure, accompanied by the development of a more layered morphology, as observed in MoB-7.5/Ni-BDC/NF/*300*

(Figure 3.8e and f). Further annealing at 400 °C led to partial decomposition of the Ni-BDC framework and the formation of well-dispersed Ni nanoparticles, clearly visible in Figure 3.8g and the high-magnification image in Figure 3.8h. Notably, the particle size in the annealed samples was reduced and more uniform compared to the pre-annealed composites, reflecting the restructuring effect of thermal treatment. Elemental mapping conducted by EDS confirmed the uniform distribution of Ni, C, and O in the pristine Ni-BDC/NF sample (Figure 3.9a). In contrast, the MoB-7.5/Ni-BDC/NF and MoB-7.5/Ni-BDC/NF/*400* nanocomposites exhibited an additional homogeneous distribution of Mo across the surface (Figure 3.9b and c), indicating successful and stable incorporation of MoB into the composite structure even after high-temperature annealing.

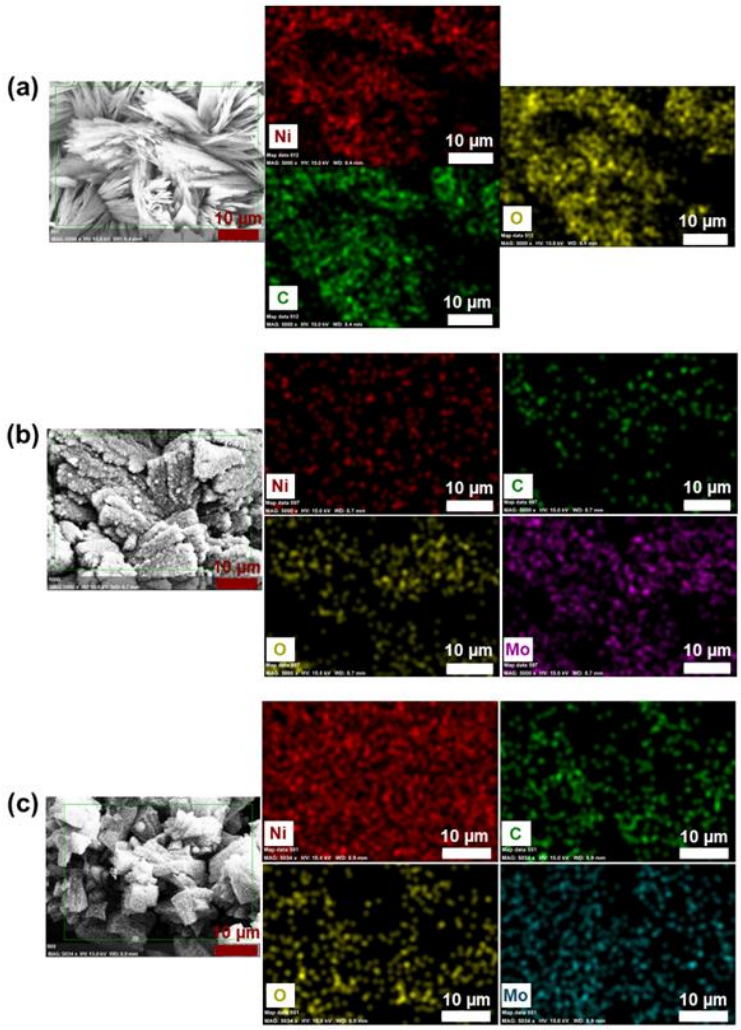

Figure 3.9 SEM-EDS elemental mapping of (a) Ni-BDC/NF, (b) MoB-7.5/Ni-BDC/NF, and (c) MoB-7.5/Ni-BDC/NF/*400*.

Microstructural and morphological characteristics of the samples were further investigated through TEM and HR-TEM analyses. TEM imaging of Ni-BDC revealed large, smooth platelet-like structures (Figure 3.10a), consistent with the rod-like morphology observed in SEM. In contrast, the MoB-7.5/Ni-BDC nanocomposite exhibited a significant morphological transformation, where the original platelets evolved into denser, polygonal aggregates (Figure 3.10b). For the MoB-7.5/Ni-BDC/*400* sample, TEM and HR-TEM analyses confirmed further structural evolution (Figure 3.10c and d). Thermal decomposition induced the fragmentation of the Ni-BDC framework and led to the formation of well-dispersed Ni nanoparticles, while remnants of thin, layered MoB sheets remained visible, as evidenced by their similar morphology to the pristine MoB MBene shown in Figure 3.11.

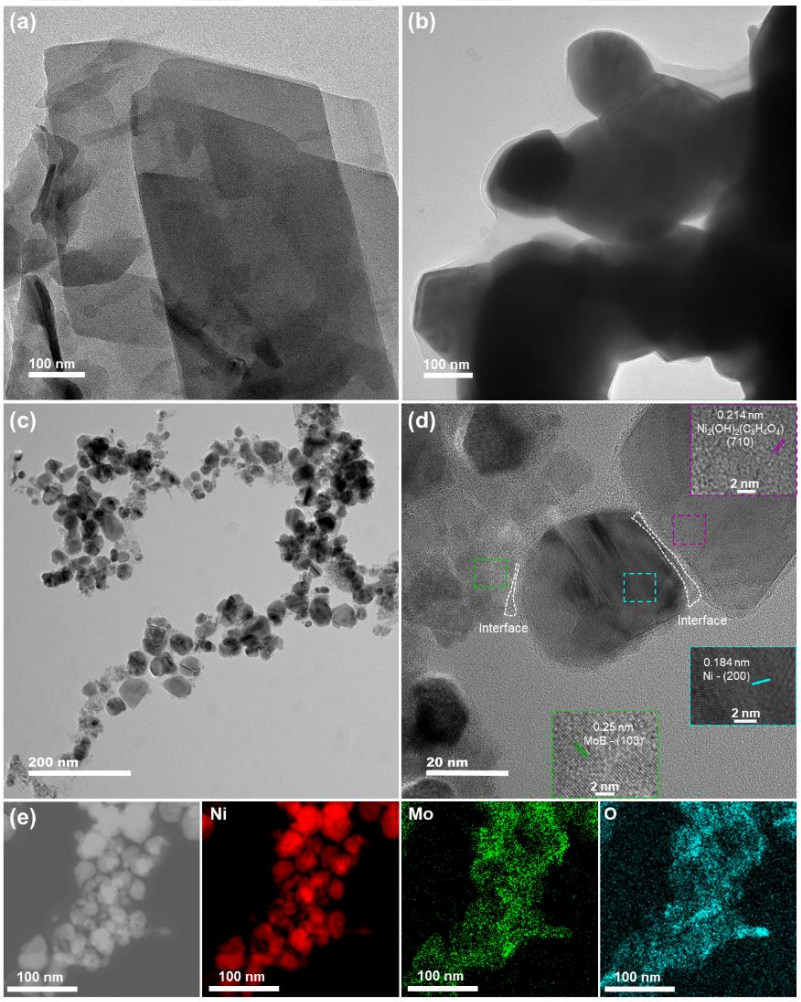

Figure 3.10 TEM images of (a) Ni-BDC, (b) MoB-7.5/Ni-BDC, and (c) MoB-7.5/Ni-BDC/*400*. HR-TEM images of (d) MoB-7.5/Ni-BDC/*400* and (e) HAADF-STEM image along with the corresponding EDS–STEM elemental mappings.

High-resolution TEM analysis provided additional structural insights. Lattice fringes with interplanar spacings of 0.25 nm, 0.184 nm, and 0.214 nm were indexed to the (103) plane of MoB, the (200) plane of metallic Ni, and the (710) plane of $Ni_2(OH)_2(tp)$, respectively. The clear interfaces observed between these distinct phases confirm the successful formation of an integrated nanocomposite structure. Such strong interfacial coupling is expected to facilitate efficient charge transfer, thereby enhancing the electrochemical activity of the material. Further elemental analysis by HAADF-STEM imaging and EDS-STEM mapping (Figure 3.10e) revealed a homogeneous distribution of Ni, Mo, and O throughout the nanocomposite.

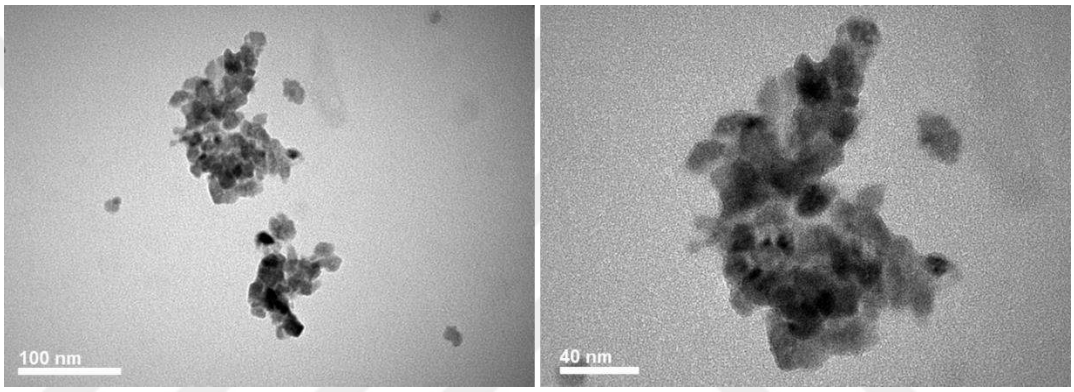

Figure 3.11 TEM images of MoB MBene.

To probe further into the structural evolution and porosity changes induced by MoB incorporation and subsequent thermal treatment, nitrogen adsorption–desorption measurements were conducted. The corresponding isotherms and pore size distribution curves are presented in Figure 3.12, with the quantitative results summarized in Table B1. Pristine Ni-BDC exhibited a moderately porous structure. The insignificant BET surface area observed both in Ni-BDC and MoB-7.5/Ni-BDC can be ascribed to the trapped moisture in the micro- and mesoporous structure of Ni-MOF. Upon MoB incorporation, both surface area and pore volume slightly decreased, likely due to partial pore blockage or structural densification. Interestingly, thermal treatment at 400 °C led to a pronounced increase in both surface area and porosity. This enhancement is attributed to the removal of residual organic species, the generation of new porous domains, and the formation of well-dispersed nickel nanoparticles, as confirmed by SEM and further EDX analyses. The isotherm of the thermally treated composite displays a sharp increase at high relative pressures, indicative of the development of macroporous features [126, 127]. Such

textural improvements are expected to increase the number of accessible active sites and facilitate mass transport.

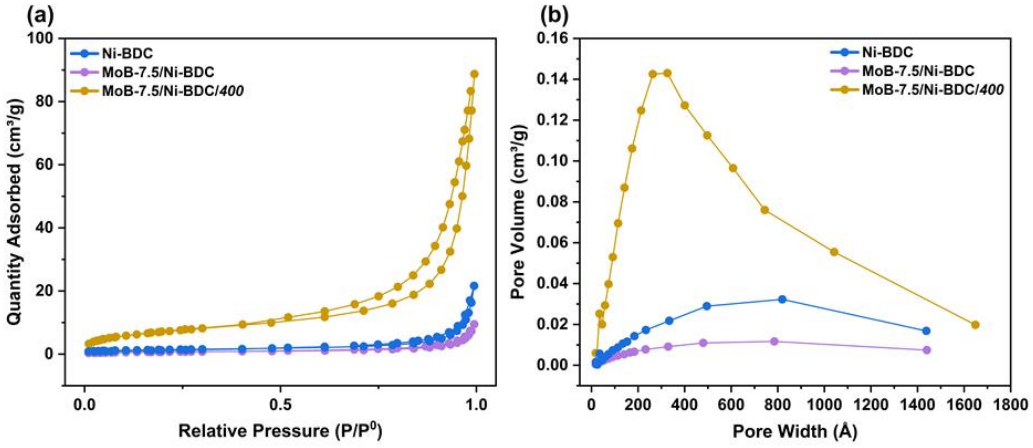

Figure 3.12 Nitrogen adsorption–desorption isotherms (a) and corresponding BJH pore size distribution curves (b) of Ni-BDC, MoB-7.5/Ni-BDC, and MoB-7.5/Ni-BDC/*400* samples.

XPS analysis was employed to investigate the chemical composition and oxidation states of the nanocomposites synthesized with Ni-BDC. In agreement with the SEM-EDS findings, the XPS survey spectrum confirmed the presence of Ni, Mo, B, C, and O in the samples (Figure B2). Detailed examination of the high-resolution Ni 2p spectrum (Figure 3.13a) for Ni-BDC/NF revealed oxidation peaks characteristic of Ni^{2+} ($2p_{3/2}$: 855.5 eV; $2p_{1/2}$: 872.8 eV) and Ni^{3+} ($2p_{3/2}$: 856.6 eV; $2p_{1/2}$: 873.9 eV), accompanied by satellite features [95]. Similar observations were made for the MoB-7.5/Ni-BDC/NF nanocomposite, with Ni^{2+} ($2p_{3/2}$: 856.0 eV; $2p_{1/2}$: 873.3 eV) and Ni^{3+} ($2p_{3/2}$: 857.6 eV; $2p_{1/2}$: 874.9 eV) peaks. Coupling MoB and Ni-BDC resulted in Ni shifting to higher binding energies, implying a potential electron transfer between the two mentioned components; in this scenario, Ni donated electrons. It must be pointed out that, according to the literature, the Ni^{2+} species may originate from $Ni(OH)_2$ [125], whereas the Ni^{3+} species can arise from the octahedral coordination of Ni atoms with terephthalate ligands in the 3D Ni-BDC framework [128].

After heat treatment, significant structural and electronic transformations were detected on the MoB-7.5/Ni-BDC/NF/*400*. The high-resolution Ni 2p spectrum of the annealed sample displayed distinct peaks for Ni^0 ($2p_{3/2}$: 852.8 eV; $2p_{1/2}$: 870.1 eV), Ni^{2+} ($2p_{3/2}$: 855.8 eV; $2p_{1/2}$: 873.2 eV), and Ni^{3+} ($2p_{3/2}$: 857.8 eV; $2p_{1/2}$: 875.0 eV) [125]. These

shifts highlight the formation of metallic Ni nanoparticles and changes in the Ni-BDC structure due to thermal treatment. Metallic nickel has been widely shown to accelerate alkaline HER, on account of its ability to adsorb hydrogen atoms (H*) and facilitate electron transfer, thereby promoting the rate-limiting Volmer step [129]. Similar to the above-mentioned observation, both oxidation states of 2+ and 3+ of Ni present in the final product shifted to higher binding energies as a result of the heat treatment process compared to pristine Ni-BDC.

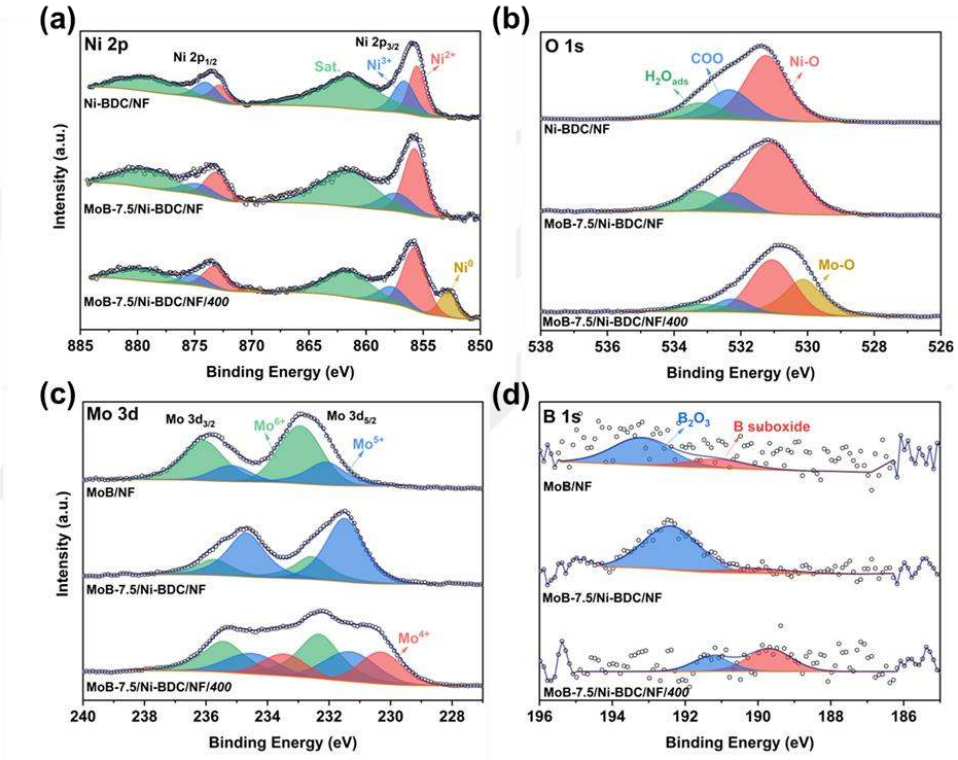

Figure 3.13 High resolution XPS spectrum (a) Ni 2p and (b) O 1s for Ni-BDC/NF, MoB-7.5/Ni-BDC/NF and MoB-7.5/Ni-BDC/NF/*400*; (c) Mo 3d and (d) B 1s for MoB/NF, MoB-7.5/Ni-BDC/NF and MoB-7.5/Ni-BDC/NF/*400*.

Building upon the insights from the XPS survey spectrum, the O 1s spectrum provided additional evidence of the chemical interactions within the nanocomposites (Figure 3.13b). In the Ni-BDC/NF and the MoB-7.5/Ni-BDC/NF samples, three prominent peaks were identified, corresponding to Ni-O (531.2 eV), COO (532.3 eV), and adsorbed H_2O (H_2O_{ads}, 533.2 eV) [130]. The MoB-7.5/Ni-BDC/NF/*400* nanocomposite exhibited an additional peak at 530.1 eV, which was attributed to the Mo-O bond [131].

To further understand the chemical states within the composite, the Mo 3d high-resolution spectrum was analyzed (Figure 3.13c). In the pristine MoB/NF sample, characteristic doublets corresponding to Mo^{5+} ($3d_{5/2}$: 232.1 eV; $3d_{3/2}$: 235.2 eV), and Mo^{6+} ($3d_{5/2}$: 233.0 eV; $3d_{3/2}$: 236.1 eV) were identified. The MoB-7.5/Ni-BDC nanocomposite exhibited similar peaks, with slight shifts toward lower binding energies: Mo^{5+} ($3d_{5/2}$: 231.5 eV; $3d_{3/2}$: 234.7 eV), and Mo^{6+} ($3d_{5/2}$: 232.6 eV; $3d_{3/2}$: 235.7 eV). In this context, it can be inferred that coupling MoB and Ni-BDC brought about electronic interactions; in this case, Mo in the composite product gained electrons.

Following annealing at 400 °C, Mo^{4+} species ($3d_{5/2}$: 230.3 eV; $3d_{3/2}$: 233.5 eV) emerged alongside Mo^{5+} ($3d_{5/2}$: 231.3 eV; $3d_{3/2}$: 234.2 eV) and Mo^{6+} ($3d_{5/2}$: 232.3 eV; $3d_{3/2}$: 235.4 eV), indicating the coexistence of multiple oxidation states [53, 132]. From these observations, Mo in the final product significantly shifted to lower binding energies relative to MoB. This is in agreement with our earlier observation, indicating that the electronic interaction might be between Ni and Mo sites, the former donating electrons, while the latter accepting electrons.

Since boron is a light element, conventional SEM-EDS or TEM-EDS techniques often fail to quantify its presence accurately, necessitating the use of XPS for precise analysis. High-resolution B 1s spectra (Figure 3.13d) provided key insights, revealing oxidation peaks for boron suboxides and B_2O_3 in all samples, including MoB/NF, MoB-7.5/Ni-BDC/NF, and MoB-7.5/Ni-BDC/NF/*400*. Binding energies for the boron suboxide peaks were observed at 191.2 eV, 190.0 eV, and 190.5 eV for the respective samples, while the B_2O_3 peaks appeared at 193.2 eV, 192.4 eV, and 192.6 eV [61, 83].

Due to the surface-sensitive nature of XPS (~10 nm detection depth), direct observation of MoB MBene signals in the nanocomposites was limited. This suggests that surface oxide species such as MoO_2, Mo_2O_5, MoO_3, and B_2O_3 were likely formed during sample preparation (e.g., exposure to DI water, ethanol, DMF, or air) [133]. However, the XPS survey and high-resolution spectra of powdered MoAlB and MoB MBene (Figure 3.14a and b) confirmed the presence of underlying MoB structures, as evidenced by characteristic Mo–B bonding features in both Mo 3d and B 1s regions (Figure B3). Additionally, a Zn 2p signal was detected in MoB MBene, consistent with minor residual Zn species from the $ZnCl_2$ molten salt etching process, as also seen in SEM-EDS analysis.

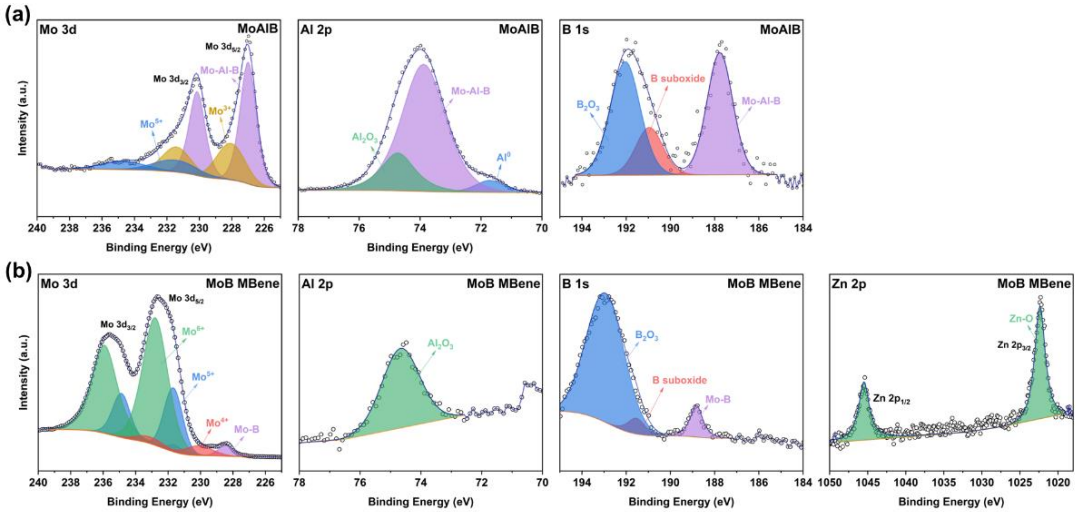

Figure 3.14 XPS high resolution spectrum of Mo 3d, B 1s, Al 2p for (a) MoAlB and (b) MoB MBene with Zn 2p.

3.4 Electrochemical Studies

3.4.1 Electrocatalytic Activities of the Electrodes for HER

The electrocatalytic performance of the prepared samples was evaluated in 1.0 M KOH electrolyte using a three-electrode system. HER polarization curves for Pt/C and the prepared catalysts were obtained by LSV over a reduction potential range of 0.0 to -0.8 V (Figure 3.15a). LSV curves were corrected using 60% iR compensation. iR correction was not applied to the Pt/C reference, as it was used solely for benchmarking. Overpotentials corresponding to current densities of 10 mA cm^{-2} and 50 mA cm^{-2} were extracted from the LSV data and are presented in a 3D bar graph (Figure 3.15b). As anticipated, the state-of-the-art material Pt/C exhibited the lowest overpotential, achieving 61 mV at 10 mA cm^{-2}. Among the prepared catalysts, the overpotentials followed the order: MoB-7.5/Ni-BDC/NF = 214 mV < MoB-5/Ni-BDC/NF = 231 mV < MoB-10/Ni-BDC/NF = 245 mV < Ni-BDC/NF = 245 mV < MoB/*400*/NF = 267 mV < MoB/NF = 279 mV. These results demonstrate that the nanocomposite containing 7.5 wt.% MoB combined with Ni-BDC exhibited superior performance among the prepared samples, making it a suitable candidate for annealing.

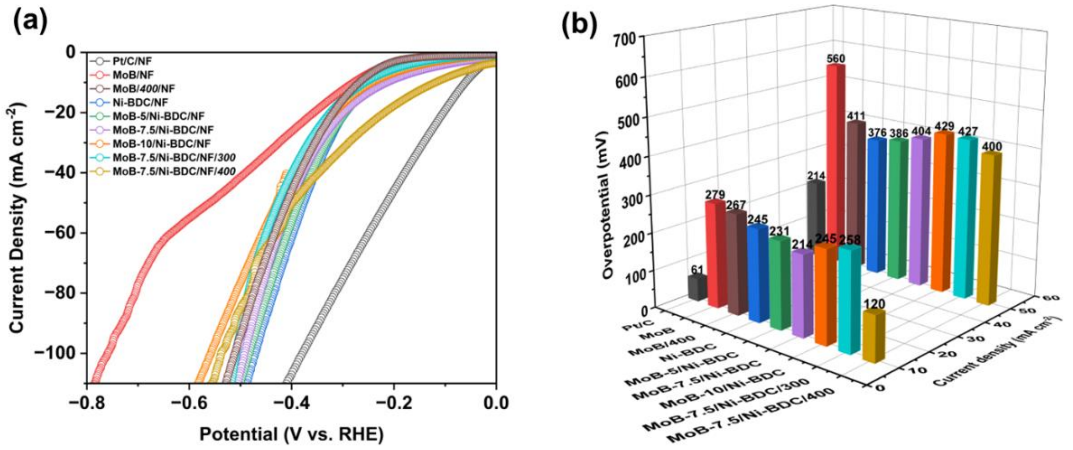

Figure 3.15 (a) HER polarization curves of the samples, (b) 3D bar graphs of overpotentials at 10 and 50 mA cm^{-2}.

While a slight decline in performance was observed after annealing at 300 °C (MoB-7.5/Ni-BDC/NF/*300* = 258 mV), annealing at 400 °C significantly enhanced the catalytic activity and drastically reduced the overpotential (MoB-7.5/Ni-BDC/NF/*400* = 120 mV). This indicates that while the pristine forms of Ni-BDC, MoB, and even thermally treated MoB (MoB/*400*) exhibited relatively high overpotentials, the composite structure of MoB-7.5/Ni-BDC/NF benefited greatly from thermal treatment at 400 °C, yielding substantial improvements in catalytic efficiency with the changing Ni-BDC structure and formation of Ni nanoparticles. It must be pointed out that Ni-based materials are popular electrocatalysts for alkaline HER because their hydrogen binding energy is similar to that of Pt [134]. To benchmark our catalyst against relevant systems, recent literature data on MBene-based and Ni-based electrocatalysts have been summarized in Table B2.

The electrochemical HER kinetics of the catalysts were analyzed using Tafel slope calculations. In alkaline media, the HER mechanism involves the adsorption and desorption of hydrogen atoms or molecules, which proceed via the Volmer-Tafel or Volmer-Heyrovsky pathways. These processes are represented by the following reaction steps [5]:

- Volmer step: $H_2O + e^- + * \rightarrow H_{ads}* + OH^-$
- Heyrovsky step: $H_{ads}* + H_2O + e^- \rightarrow H_2 + OH^- + *$
- Tafel step: $2H_{ads}* \rightarrow H_2 + 2*$

here, * shows the active sites on the catalyst surface, while H_{ads}* represents hydrogen atoms adsorbed onto these active sites. In the Volmer step, a water molecule interacts with the catalyst surface and undergoes an electrochemical reduction, forming H_{ads}*. Experimental studies have shown that this step typically corresponds to a Tafel slope of approximately 120 mV dec^{-1}. Subsequently, hydrogen gas can be produced either through a chemical pathway involving the combination of two H_{ads}* species (Tafel step) with a Tafel slope of 40 mV dec-1 or via an electrochemical reaction between H_2O and H_{ads}* (Heyrovsky step), which is associated with a Tafel slope of 30 mV dec^{-1}.

The Tafel slopes of the prepared catalysts were derived from the LSV data (Figure 3.16a). Among the samples, Pt/C exhibited the lowest Tafel slope at 102 mV dec^{-1}, indicating facile HER kinetics. In contrast, all other prepared catalysts displayed Tafel slopes exceeding 120 mV dec^{-1}, signifying that the rate-determining step involves the adsorption of hydrogen atoms at the active sites. Among the unannealed samples, MoB/*400*/NF demonstrated the lowest Tafel slope (140 mV dec^{-1}), reflecting faster reaction kinetics and enhanced hydrogen adsorption efficiency. Interestingly, the annealed MoB-7.5/Ni-BDC/NF/*400*, which exhibited the most favorable overall performance, had a slightly higher Tafel slope (235 mV dec^{-1}). This discrepancy can be attributed to factors previously detailed in our earlier studies [135, 136]. Specifically, the enhanced performance is predominantly influenced by the presence of highly conductive components, such as Ni and Mo, and the improved interfacial electronic interactions within the composite material. These factors significantly enhance electron transfer and reduce the overpotential for HER, thereby exerting a more pronounced effect on catalytic activity.

Although the MoB-7.5/Ni-BDC/NF/*400* composite exhibits a low overpotential of 120 mV at 10 mA cm^{-2}, its high Tafel slope (235 mV dec^{-1}) does not necessarily reflect sluggish intrinsic kinetics. In porous composite electrodes, the Tafel slope is often affected by factors such as surface coverage with hydrogen intermediates, limited charge-transfer efficiency, and increased double-layer capacitance. At elevated overpotentials, saturation of active sites can alter the rate-determining step, typically shifting it toward a Volmer-type mechanism, which is characterized by higher slope values [137]. Moreover, non-Faradaic processes and uncompensated resistance may distort the LSV-derived

slope, particularly in systems with high capacitance or moderate conductivity [135]. These combined effects likely contribute to the elevated Tafel slope observed in this work.

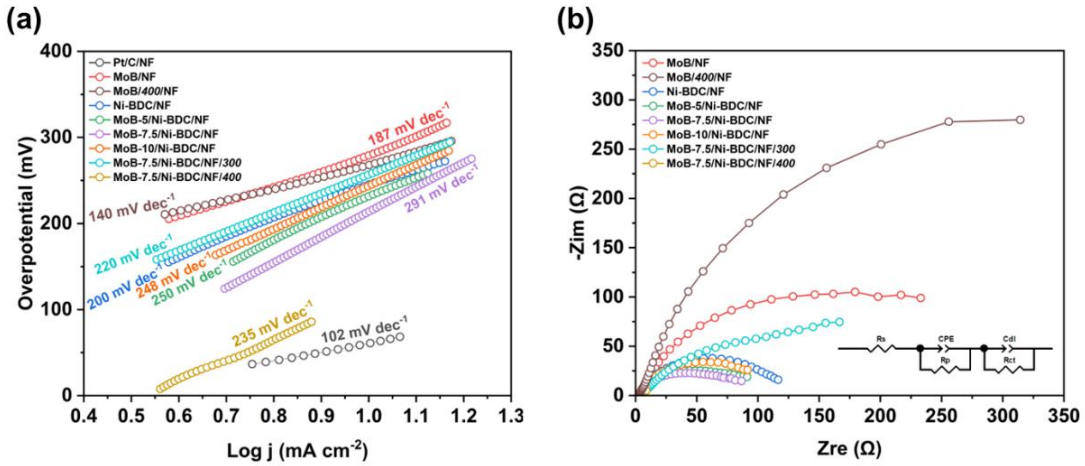

Figure 3.16 (a) HER Tafel plots obtained by polarization curves, (b) EIS spectra recorded at 0.0 V versus RHE.

EIS analysis was also performed to better understand HER kinetics. The Nyquist plots indicated that all catalysts exhibited similar semicircular profiles (Figure 3.16b). The equivalent circuit models used for the analysis consisted of solution resistance (R_s), porosity resistance (R_p), and charge transfer resistance (R_{ct}). A constant phase element (CPE) was included in the model to address the non-ideal behavior of capacitive components. Additionally, the double-layer capacitance (C_{dl}) at the electrode-electrolyte interface was incorporated into the calculations, with all the fitted parameters summarized in Table B3. Among the tested samples, MoB-7.5/Ni-BDC/NF/*400* demonstrated the lowest charge transfer resistance (R_{ct} = 5.4 Ω), indicating superior charge transfer kinetics. Similarly, MoB-7.5/Ni-BDC/NF exhibited a relatively low value (R_{ct} = 35.42 Ω) compared to other nanocomposites. Furthermore, MoB-7.5/Ni-BDC/NF/*400* showed the highest double-layer capacitance (C_{dl} = 0.37525), which suggests enhanced non-faradaic/capacitive behavior. This increased capacitive behavior may contribute to the higher Tafel slope observed in its LSV curves, indicating distinctive electrochemical characteristics [135].

ECSA analyses were carried out to comprehensively assess the surface characteristics of the catalysts. Based on cyclic voltammetry (Figure 3.17), the ECSA,

proportional to C_{dl}, demonstrated that MoB-7.5/Ni-BDC/NF/*400* possesses a markedly higher C_{dl} (13.75 mF cm^{-2}) than its unannealed counterpart (MoB-7.5/Ni-BDC/NF = 0.39 mF cm^{-2}), indicative of significantly enhanced HER activity (Figure 3.18a and b). The formation of metallic Ni from the transformation of Ni-BDC resulted in a porous Ni-based catalyst on the MoB sheet, enhancing the active metal centers in the MoB phase. In addition, the high porosity of the distributed Ni nanoparticles is evident from the HR-TEM images, which are above a few nm. From an electrochemical perspective, this mesoporous morphology facilitates easy electrolyte penetration throughout the sample, enabling rapid ion/electron transfer and enhancing electrochemical reactivity [95, 138].

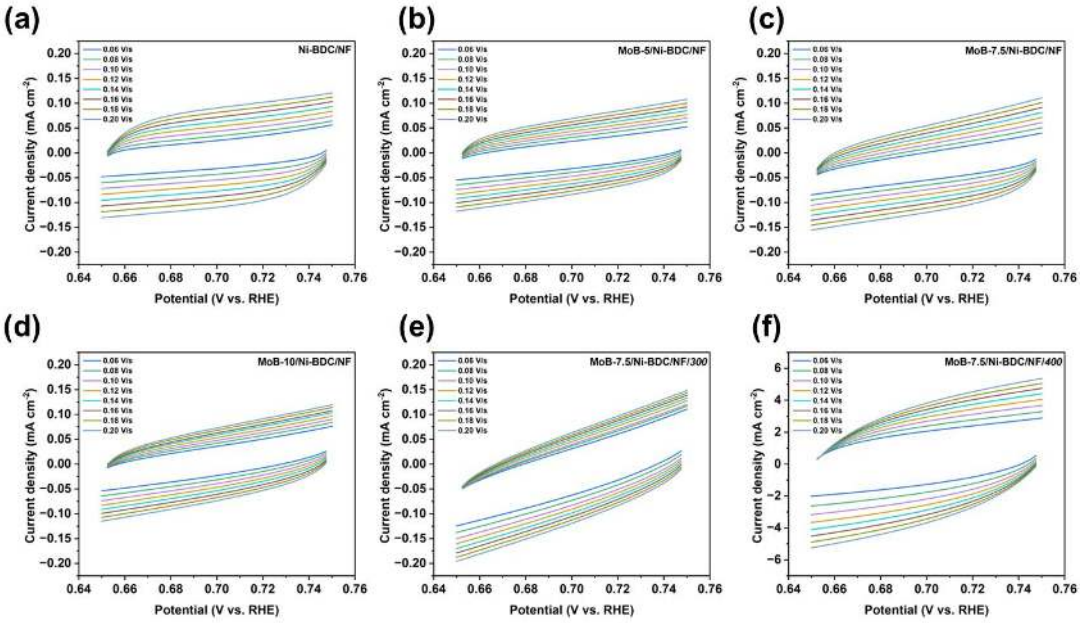

Figure 3.17 Typical cyclic voltammetry (CV) curves obtained at different scan rates (0.06–0.20 V s-1) within the potential window 0.65–0.75 V vs RHE for (a) Ni-BDC/NF, (b) MoB-5/Ni-BDC/NF, (c) MoB-7.5/Ni-BDC/NF, (d) MoB-10/Ni-BDC/NF, (e) MoB-7.5/Ni-BDC/NF/*300* and (f) MoB-7.5/Ni-BDC/NF/*400*.

The dramatic increase in C_{dl} from 0.39 to 13.75 mF cm^{-2} for MoB-7.5/Ni-BDC/NF/*400* clearly reflects the formation of a highly porous Ni nanoparticle network on MoB sheets, leading to a considerable expansion of active surface area. Such Ni^0 sites are well-established as primary HER active centers, with Ni metal showing favorable hydrogen adsorption energy ($\Delta G_H \approx$ -0.4 eV) —close to Pt— and facilitating efficient Volmer–Heyrovsky kinetics [139]. Moreover, recent studies on Ni-MoB heterostructures revealed that electronic coupling at the Ni/MoB interface enhances surface charge density, supporting rapid charge transfer and synergistically

boosting HER performance [140]. Therefore, the composite's superior activity can be attributed to a cooperative mechanism: abundant Ni^0 active sites provide the necessary adsorption and desorption steps, while the conductive MoB scaffold [58] and the Ni–MoB interface ensure efficient electron delivery and catalyst stability.

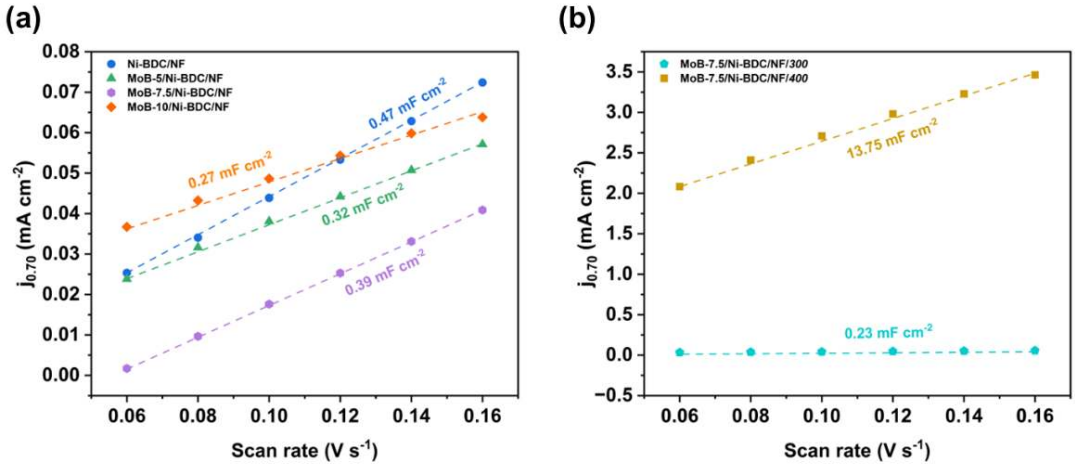

Figure 3.18 Capacitive current density versus scan rate curves for ECSA measurements (a) before and (b) after annealing.

Among the unannealed nanocomposites, MoB-7.5/Ni-BDC/NF displayed the largest C_{dl} (relative to MoB-5/Ni-BDC/NF = 0.32 mF cm^{-2} and MoB-10/Ni-BDC/NF = 0.27 mF cm^{-2}), resulting in its lower overpotential. Interestingly, Ni-BDC/NF alone exhibited a relatively larger C_{dl} (0.47 mF cm^{-2}) compared to these particular composites, suggesting that certain intrinsic structural features in Ni-BDC favor electrochemical activity prior to composite formation. Interestingly, the C_{dl} value for Ni-BDC is higher than that of the composite electrodes. This difference can be attributed to the distinct morphologies of the two catalysts, as shown in the SEM images in Figure 3.8a and c. The lamellar structure of Ni-BDC/NF (Figure 3.8a) provides a higher active surface area for electrochemical reactions, whereas the highly irregular morphology of MoB-7.5/Ni-BDC/NF (Figure 3.8c) may hinder electrolyte penetration and diffusion. It should be noted that ECSA alone is not a definitive indicator of electrode activity, as it quantifies the number of active sites but does not account for their quality, which is equally crucial.

To further validate the intrinsic catalytic performance of the synthesized materials beyond surface-related effects, turnover frequency (TOF) calculations were performed (Table B4). TOF offers a reliable metric for evaluating the per-site hydrogen evolution

rate, effectively isolating the contribution of each active center. As presented in Table B4, the MoB-7.5/Ni-BDC/NF/*400* electrode consistently displayed the highest TOF values across nearly all measured overpotentials (Figure 3.19a). Notably, at an overpotential of 200 mV, it achieved a TOF of 5.54×10^{-3} s^{-1} - over twice the value of its unannealed counterpart containing the same MoB loading 2.68×10^{-3} s^{-1} - highlighting the substantial enhancement in site-specific activity induced by thermal activation. This increase aligns well with the sharp rise in C_{dl} and the development of nanostructured metallic Ni domains, both of which collectively boost the number and accessibility of HER-active regions. Although SEM imaging revealed a relatively disordered surface, the well-integrated MoB–Ni interface likely facilitates efficient charge movement and proton reduction. Hence, the observed HER performance can be attributed not only to increased active area but also to improved catalytic turnover at individual active sites, as evidenced by the superior TOF values.

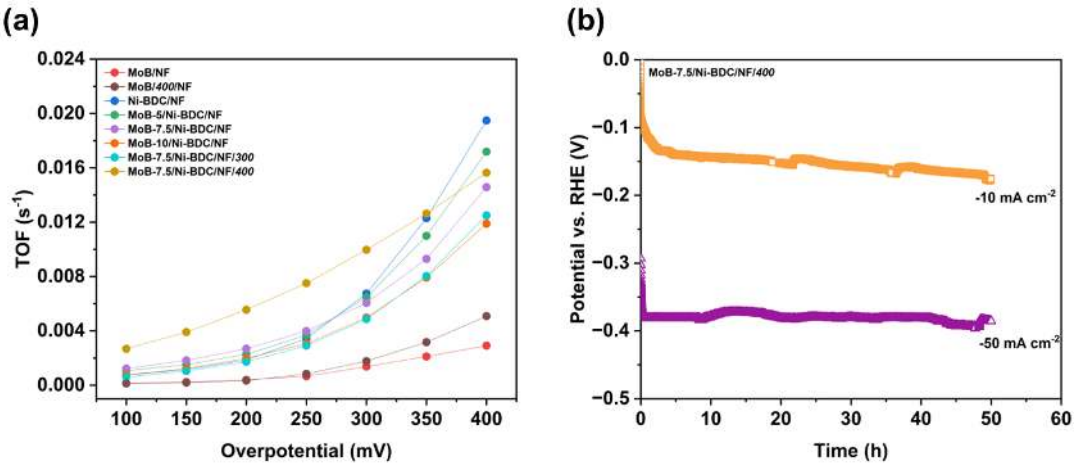

Figure 3.19 (a) TOF values of the samples at various overpotentials, (b) long-term HER stability test of best performing MoB-7.5/Ni-BDC/NF/*400* at the applied current densities of 10 and 50 mA cm^{-2}.

Interestingly, despite exhibiting a higher C_{dl} value, pristine Ni-BDC/NF demonstrates lower HER activity compared to certain MoB-integrated composites. This outcome underscores that the performance enhancement is not solely due to increased electrochemical surface area, but rather stems from improved intrinsic catalytic properties. This interpretation is reinforced by TOF results and further substantiated by XPS analysis (Figure 3.13), which reveals electronic coupling at the Ni–MoB interface. In particular, observable shifts in the binding energies of Ni 2p and Mo 3d orbitals

indicate charge redistribution, aligning with the concept of MoB-induced electronic modulation.

Long-term durability of the MoB-7.5/Ni-BDC/*400* catalysts was evaluated by chronopotentiometric measurements at current densities of 10 and 50 mA cm^{-2} in 1.0 M KOH (Figure 3.19b). During the first few hours, a decrease in potential was observed, which can be attributed to changes in the oxidation states of Mo and Ni as well as partial exfoliation of the nanocomposite structure, both of which reduce the number of active sites on the catalyst surface. Beyond this initial period, no further decrease in potential was recorded over 50 hours, emphasizing the catalyst's stability for practical applications. Furthermore, LSV performed after 50 hours at a current density of -50 mA cm^{-2} showed a moderate increase in overpotential from 120 mV to 173 mV, indicating minimal degradation in catalytic activity (Figure 3.20).

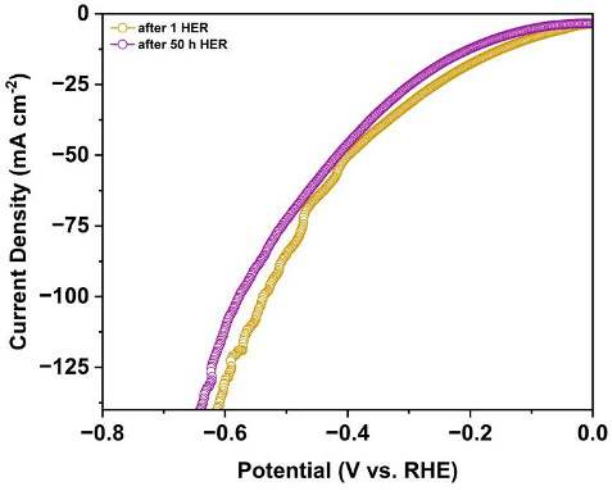

Figure 3.20 HER polarization curve of the MoB-7.5/Ni-BDC/NF/*400* catalyst after a 50 h stability test under a constant current density of 50 mA cm^{-2}.

3.4.2 Post-Electrocatalysis Characterization

Following the 50-hour stability test at a current density of 50 mA cm^{-2} on the MoB-7.5/Ni-BDC/NF/*400* nanocomposite, a series of morphological and chemical characterizations was conducted to evaluate the structural changes induced by prolonged HER operation. The SEM images (Figure 3.21a and b) revealed a morphology similar to that observed before testing, even after a single HER operation and a 50-hour stability test.

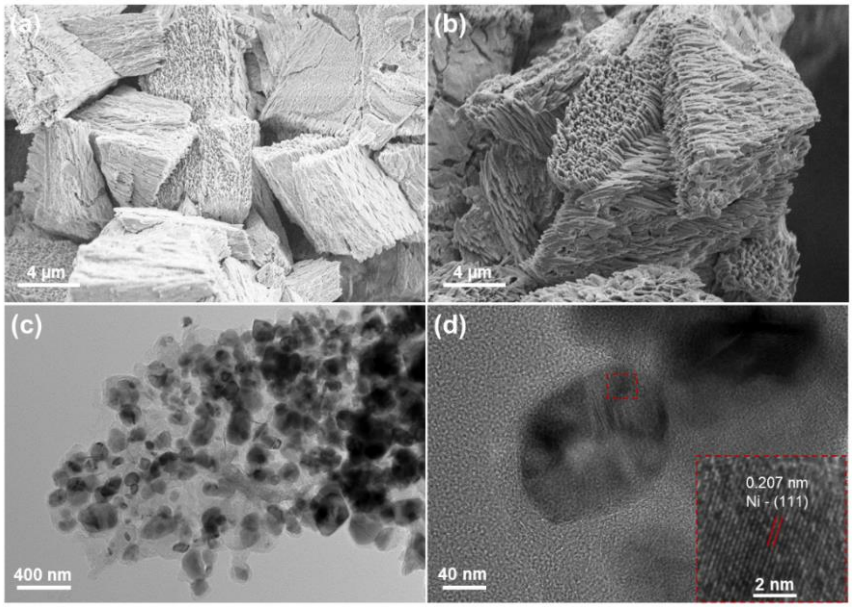

Figure 3.21 SEM images of MoB-7.5/Ni-BDC/NF/*400* after (a) 1 HER run and (b) 50 h HER stability test. (c) TEM and (d) HR-TEM images of MoB-7.5/Ni-BDC/NF/*400* after 50 h HER.

TEM and HR-TEM further confirmed these observations, showing lattice fringes of 0.207 nm corresponding to the (111) plane of Ni (Figure 3.21c and d). In addition, TEM-EDS mapping demonstrated that Ni, Mo, and O remained well-distributed throughout the structure (Figure 3.22).

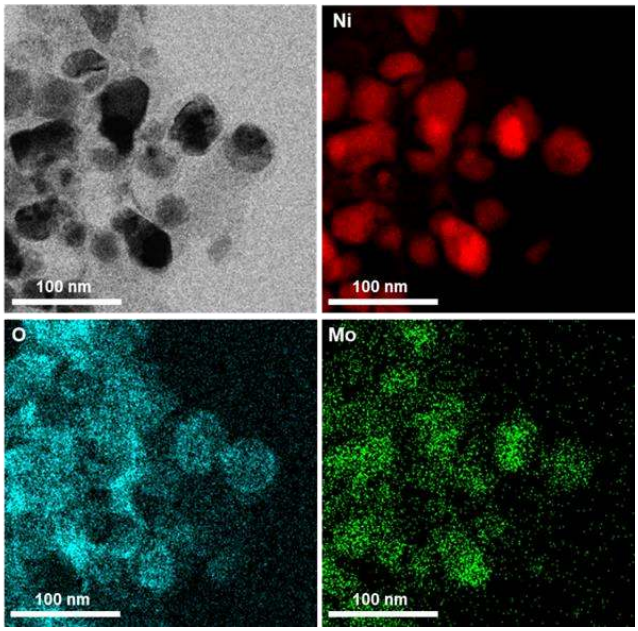

Figure 3.22 TEM-EDS elemental mappings of MoB-7.5/Ni-BDC/NF/*400* after 50 hours stability test at a current density of 50 mA cm^{-2}.

Surface chemical states were investigated after electrochemical reaction by XPS (Figure 3.23). A comparison among the fresh samples, the catalyst after a single HER cycle, and the catalyst after 50 hours of operation revealed significant changes in the Ni 2p region (Figure 3.23a). Although elemental Ni was still detectable after the initial HER run, its intensity significantly decreased after 50 hours of testing. Instead, Ni^{2+} and Ni^{3+} peaks emerged as dominant, accompanied by a shift in Ni 2p binding energies to lower values relative to the fresh sample, which is solid proof that the Ni has been drastically reduced after 50 hours. The emergence of oxidation states of 2+ and 3+ — similar to what we observed on the fresh sample — might be attributed to $Ni(OH)_2$ and NiOOH. The overall Ni atomic proportion also decreased as compared to the fresh sample (from 5.56 to 4.84), suggesting that Ni atoms actively participated in hydrogen evolution (Table 3.1). This can partially be attributed to catalyst detachment from the NF substrate and demetallation. Similarly, the Mo 3d spectrum showed a shift of Mo^{5+} to higher binding energy and Mo^{6+} to lower binding energy (Figure 3.23b), along with a marked decline in its atomic proportion (from 8.82 to 4.20). According to these findings, both Ni and Mo have experienced extreme reduction during long-term HER operation. This behavior suggests that both metals are actively involved in H^+ adsorption sites on the catalyst surface, potentially contributing to the overall hydrogen evolution reaction. The evolution of metal oxidation states may help create or modify active sites, thereby influencing long-term catalytic performance.

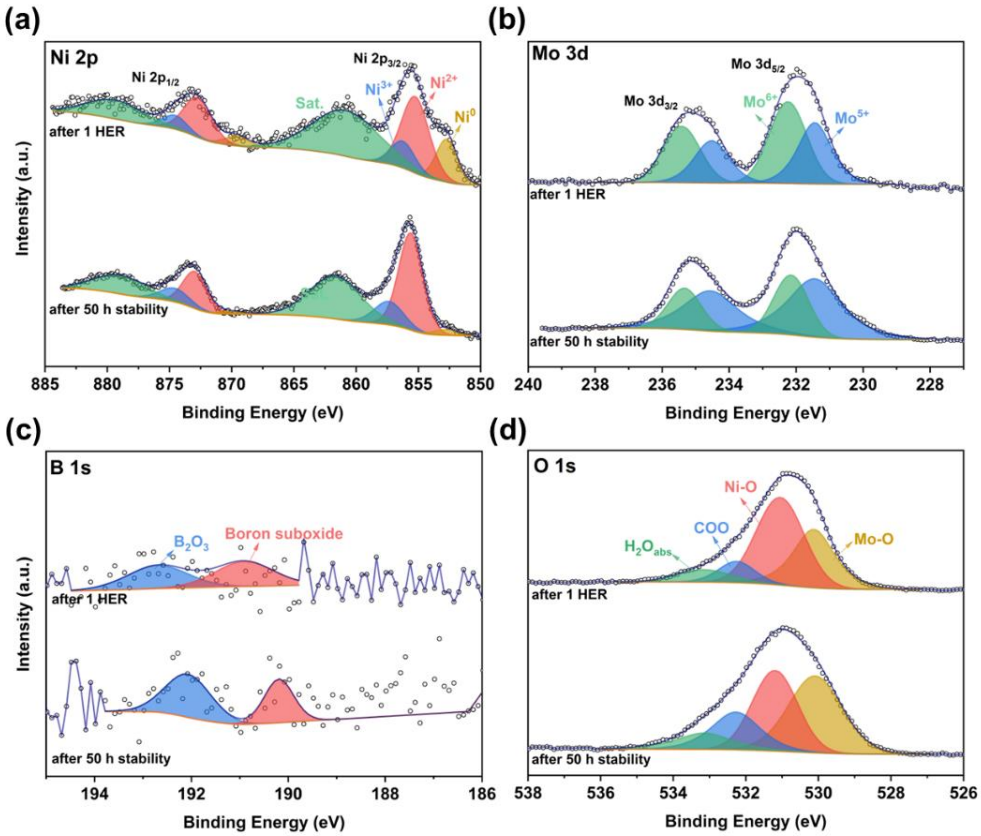

Figure 3.23 High-resolution XPS spectra of MoB-7.5/Ni-BDC/NF/*400* after HER and 50-hour stability testing: (a) Ni 2p, (b) Mo 3d, (c) B 1s, (d) O 1s.

Although no major changes were observed in the B 1s peak position (Figure 3.23c), the B atomic proportion decreased (from 0.96 to 0.69). In contrast, the O 1s atomic proportion gradually increased (from 39.79 to 44.73), which is consistent with the formation of more oxidized species (Figure 3.23d).

Table 3.1 XPS results of MoB-7.5/Ni-BDC/NF/*400* as an atomic percent before and after stability test.

Nanocomposites / Elements (at.%)	MoB-7.5/Ni-BDC/NF/*400*	after 50 h HER
Ni	5.56	4.84
Mo	8.82	4.2
B	0.96	0.69
O	39.79	44.73
C	44.87	45.54
Total	**100**	**100**

3.5 Conclusion

Overall, MoB MBene was initially synthesized via the Lewis acid molten salt method using $ZnCl_2$ and subsequently incorporated into Ni-BDC structures through a solvothermal process at various weight ratios (5, 7.5, and 10 wt.%) to form composite architectures on Ni foam. Post-synthesis thermal treatments at 300 °C and 400 °C were employed to promote the formation of Ni nanoparticles, which significantly contributed to catalytic activity. Electrochemical evaluation in 1.0 M KOH revealed that the nanocomposite containing 7.5 wt.% MoB MBene exhibited an overpotential of 214 mV for the hydrogen evolution reaction, which was impressively reduced to 120 mV following an annealing at 400 °C. Furthermore, long-term stability testing demonstrated sustained performance for up to 50 hours at a current density of 50 mA cm^{-2}. Comprehensive chemical and morphological characterizations (XRD, TGA, SEM, EDS, TEM, AFM, BET, XPS) confirmed a substantial increase in surface area accompanied by a notable morphology transformation, both of which supported enhanced HER performance. XPS analysis provided evidence of strong electronic interactions between MoB MBene and the Ni-BDC matrix, which are believed to enhance both the structural stability and the overall electrocatalytic activity of the composite. These findings highlight the potential of MoB MBene–Ni-BDC composites as efficient and durable electrocatalysts for water splitting applications.

Chapter 4: Conclusion

MBenes are regarded as promising candidates for high-performance electrocatalysts in water splitting due to their large surface area and excellent electrical conductivity. Additionally, the transition metals incorporated in their structure are far more abundant and cost-effective compared to noble metals, making them attractive and practical alternatives for catalysis research. In this thesis, MoAlB (one of the MAB phases and a suitable precursor for MBene synthesis) was synthesized and evaluated. By selectively etching Al from the structure through different chemical approaches, MBene-like materials were successfully obtained. Their electrocatalytic performance in HER applications was subsequently investigated.

To synthesize MoAlB, α-MoB was first mechanically activated using oxide powders and active carbon as a reductant, followed by carbothermal reduction. The resultant MoAlB phase was then obtained by presurless sintering with aluminum addition. XRD analysis confirmed that both α-MoB and the synthesized MoAlB were phase-pure. SEM revealed that MoAlB exhibited a microcrystalline and irregular morphology.

Structurally, MoAlB consists of two aluminum layers, which is uncommon among MAB phases with the exception of WAlB. Theoretical studies have suggested that Mo_2AlB_2 is the most appropriate precursor for MoB MBene due to its favorable layered structure and bonding characteristics. However, MoAlB is the only thermodynamically stable ternary phase within the Mo–Al–B system, making direct synthesis of Mo_2AlB_2 via conventional solid-state routes unfeasible. Therefore, in the second part of this thesis, the synthesis of Mo_2AlB_2 from MoAlB was investigated. Initial experiments employed aqueous HCl solutions. After 6 hours of stirring in 1 M HCl, XRD results exhibited a notable shift in the (020) plane toward higher angles, suggesting structural transformation. However, XRD and SEM-EDX analyses indicated the formation of intermediate phases such as $Mo_4Al_3B_4$ referred to as $MoAl_{1-x}B$ rather than the desired Mo_2AlB_2.

When it became evident that variations in acid concentration, reaction time, or temperature did not result in significant improvement, a gas-phase etching method was employed. This was achieved using in situ generated HCl gas produced by the thermal

decomposition of NH_4Cl within a closed system. The reaction was carried out at 450 °C for 2 hours. XRD analysis confirmed that the (020) reflection shifted to 14.99°, in full agreement with the simulated pattern of Mo_2AlB_2. SEM images revealed the formation of etch cavities, and elemental analysis using SEM-EDX and ICP-MS showed a Mo:Al atomic ratio of 2.5 and 2:0.8, respectively. HRTEM analysis of the (020) plane demonstrated an interlayer spacing of 6.2 Å, in good agreement with the XRD-derived value of 5.9 Å. This novel approach successfully produced phase-pure, metastable Mo_2AlB_2 in a single step, at significantly lower temperatures and shorter reaction times compared to previously reported methods.

In the third part of this thesis, the goal was to design an efficient HER electrocatalyst by integrating the high surface area and catalytic activity of MOFs with the superior electrical conductivity of MoB MBene. MoB MBene was synthesized by etching MoAlB using Lewis acidic molten salts, specifically $ZnCl_2$, in a redox process at 700 °C for two hours, followed by acid washing. XRD confirmed the phase purity of the MoB MBene, while SEM images revealed a flake-like morphology. The MoB MBene was then combined with Ni-BDC, a nickel-based MOF, and deposited onto nickel foam using a solvothermal method, forming a nanocomposite in situ. This composite was subsequently subjected to thermal treatment. XPS indicated strong electronic interactions between the Ni-BDC and the MoB MBene, as evidenced by observed shifts in the binding energies of Ni and Mo. The formation of Ni nanoparticles after annealing at 400 °C was further verified by SEM, TEM, and XPS. BET surface area analysis showed a substantial increase from 2.49 m^2/g to 26.06 m^2/g, attributed to the creation of these nanoparticles. Electrochemical measurements revealed that the nanocomposite containing 7.5 wt.% MoB MBene and annealed at 400 °C (denoted as MoB-7.5/Ni-BDC/NF/*400*) exhibited the best HER performance, with an overpotential of 120 mV at a current density of 10 mA cm^{-2}. EIS further showed that this sample had the lowest charge transfer resistance, measured at just 5.4 Ω, indicating minimal resistance between the electrode surface and the electrolyte. Stability tests conducted at 10 and 50 mA cm^{-2} confirmed excellent durability, with the catalyst maintaining consistent performance for 50 hours.

In conclusion, this thesis successfully demonstrated the experimental synthesis of Mo_2AlB_2 and MoB from the MBene material class and their effective integration into MOF-based nanocomposites for electrocatalytic HER applications. The results of this

study provide a new and promising pathway for the development of MBene-based materials in green energy technologies.

Bibliography

1. Chu, S. and A. Majumdar, *Opportunities and challenges for a sustainable energy future.* nature, 2012. **488**(7411): p. 294-303.

2. Xiong, B., L. Chen, and J. Shi, *Anion-containing noble-metal-free bifunctional electrocatalysts for overall water splitting.* ACS Catalysis, 2018. **8**(4): p. 3688-3707.

3. Shi, Y. and B. Zhang, *Recent advances in transition metal phosphide nanomaterials: synthesis and applications in hydrogen evolution reaction.* Chemical Society Reviews, 2016. **45**(6): p. 1529-1541.

4. Wang, W., et al., *Perovskite oxide based electrodes for high-performance photoelectrochemical water splitting.* Angewandte Chemie International Edition, 2020. **59**(1): p. 136-152.

5. Zhu, J., et al., *Recent advances in electrocatalytic hydrogen evolution using nanoparticles.* Chemical reviews, 2019. **120**(2): p. 851-918.

6. Li, X., et al., *Water splitting: from electrode to green energy system.* Nano-Micro Letters, 2020. **12**(1): p. 131.

7. Li, S., et al., *Nanostructured Co-based bifunctional electrocatalysts for energy conversion and storage: current status and perspectives.* Journal of Materials Chemistry A, 2019. **7**(32): p. 18674-18707.

8. Chen, Z., et al., *Recent advances in transition metal-based electrocatalysts for alkaline hydrogen evolution.* Journal of Materials Chemistry A, 2019. **7**(25): p. 14971-15005.

9. Naguib, M., et al., *25th anniversary article: MXenes: a new family of two-dimensional materials.* Advanced materials, 2014. **26**(7): p. 992-1005.

10. Guo, Z., J. Zhou, and Z. Sun, *New two-dimensional transition metal borides for Li ion batteries and electrocatalysis.* Journal of Materials Chemistry A, 2017. **5**(45): p. 23530-23535.

11. Javed, M.S., et al., *MXenes to MBenes: latest development and opportunities for energy storage devices.* Materials Today, 2024. **74**: p. 121-148.

12. Aghamohammadi, P., et al., *Recent advances in the electrocatalytic applications (HER, OER, ORR, water splitting) of transition metal borides (MBenes) materials.* International Journal of Hydrogen Energy, 2024. **87**: p. 179-198.

13. Zhang, Y., et al., *Establishing theoretical landscapes for identifying basal plane active sites in MBene toward multifunctional HER, OER, and ORR catalysts.* Journal of Colloid and Interface Science, 2023. **652**: p. 1954-1964.

14. Zhang, T., et al., *Mo 2 B 2 MBene-supported single-atom catalysts as bifunctional HER/OER and OER/ORR electrocatalysts.* Journal of Materials Chemistry A, 2021. **9**(1): p. 433-441.

15. Feng, S., N. Miao, and J. Wang, *Hexagonal MBene (Hf2BO2): a promising platform for the electrocatalysis of hydrogen evolution reaction.* ACS Applied Materials & Interfaces, 2021. **13**(47): p. 56131-56139.

16. Xu, T., et al., *A rising 2D star: novel MBenes with excellent performance in energy conversion and storage.* Nano-Micro Letters, 2023. **15**(1): p. 6.

17. Grigoriev, S.A., et al., *Current status, research trends, and challenges in water electrolysis science and technology.* International Journal of Hydrogen Energy, 2020. **45**(49): p. 26036-26058.

18. Zeng, K. and D. Zhang, *Recent progress in alkaline water electrolysis for hydrogen production and applications.* Progress in Energy and Combustion Science, 2010. **36**(3): p. 307-326.

19. Walter, M.G., et al., *Solar water splitting cells.* Chemical reviews, 2010. **110**(11): p. 6446-6473.

20. Banoth, P., C. Kandula, and P. Kollu, *Introduction to electrocatalysts*, in *Noble Metal-Free Electrocatalysts: New Trends in Electrocatalysts for Energy Applications. Volume 2*. 2022, ACS Publications. p. 1-37.

21. You, B. and Y. Sun, *Innovative strategies for electrocatalytic water splitting.* Accounts of chemical research, 2018. **51**(7): p. 1571-1580.

22. Zeng, M. and Y. Li, *Recent advances in heterogeneous electrocatalysts for the hydrogen evolution reaction.* Journal of Materials Chemistry A, 2015. **3**(29): p. 14942-14962.

23. Chatenet, M., et al., *Water electrolysis: from textbook knowledge to the latest scientific strategies and industrial developments.* Chemical society reviews, 2022. **51**(11): p. 4583-4762.

24. Xu, H.G., et al., *Rational design of hydrogen evolution reaction electrocatalysts for commercial alkaline water electrolysis.* Small Structures, 2023. **4**(8): p. 2200404.

25. Gunaseelan, H., et al., *Metal-organic framework derived carbon-based electrocatalysis for hydrogen evolution reactions: A review.* Materials Today Sustainability, 2023. **22**: p. 100371.

26. Anantharaj, S. and S. Noda, *Appropriate use of electrochemical impedance spectroscopy in water splitting electrocatalysis.* ChemElectroChem, 2020. **7**(10): p. 2297-2308.

27. Zhang, S., et al., *Recent advances in non-precious metal electrocatalysts for pH-universal hydrogen evolution reaction.* Green Energy & Environment, 2021. **6**(4): p. 458-478.

28. Yang, Y., et al., *Engineering ruthenium-based electrocatalysts for effective hydrogen evolution reaction.* Nano-Micro Letters, 2021. **13**(1): p. 160.

29. Zhang, K. and R. Zou, *Advanced transition metal-based OER electrocatalysts: current status, opportunities, and challenges.* Small, 2021. **17**(37): p. 2100129.

30. Zhong, H., et al., *Fundamental Understanding of Structural Reconstruction Behaviors in Oxygen Evolution Reaction Electrocatalysts.* Advanced Energy Materials, 2023. **13**(31): p. 2301391.

31. Novoselov, K.S., et al., *Electric field effect in atomically thin carbon films.* science, 2004. **306**(5696): p. 666-669.

32. Zhang, Y.-n., et al., *2D van der Waals materials for ultrafast pulsed fiber lasers: review and prospect.* Nanotechnology, 2021. **33**(8): p. 082003.

33. Dong, Z., et al., *Raman characterization on two-dimensional materials-based thermoelectricity.* Molecules, 2018. **24**(1): p. 88.

34. Naguib, M., et al., *Two-Dimensional Nanocrystals Produced by Exfoliation of Ti3AlC2.* Advanced Materials, 2011. **23**(37): p. 4248-4253.

35. Dahlqvist, M., M.W. Barsoum, and J. Rosen, *MAX phases–Past, present, and future.* Materials Today, 2024. **72**: p. 1-24.

36. Rosenkranz, A., et al., *MAB-Phases and Beyond—A Tribological Success Story?* Advanced Materials Interfaces, 2022. **9**(26): p. 2200869.

37. Nair, V.G., et al., *2D MBenes: a novel member in the flatland.* Advanced Materials, 2022. **34**(23): p. 2108840.

38. Halla, F. and W. Thury, *Über boride von molybdän und wolfram.* Zeitschrift für anorganische und allgemeine Chemie, 1942. **249**(3): p. 229-237.

39. Jeitschko, W., *Die kristallstruktur von MoAlB.* Monatshefte für Chemie und verwandte Teile anderer Wissenschaften, 1966. **97**(5): p. 1472-1476.

40. Ade, M. and H. Hillebrecht, *Ternary borides Cr2AlB2, Cr3AlB4, and Cr4AlB6: The first members of the series (CrB2) n CrAl with n= 1, 2, 3 and a unifying concept for ternary borides as MAB-phases.* Inorganic chemistry, 2015. **54**(13): p. 6122-6135.

41. Alameda, L.T., et al., *Soft chemistry of hard materials: low-temperature pathways to bulk and nanostructured layered metal borides.* Accounts of Chemical Research, 2023. **56**(23): p. 3515-3524.

42. Kota, S., M. Sokol, and M.W. Barsoum, *A progress report on the MAB phases: atomically laminated, ternary transition metal borides.* International Materials Reviews, 2020. **65**(4): p. 226-255.

43. Zhang, B., J. Zhou, and Z. Sun, *MBenes: progress, challenges and future.* Journal of Materials Chemistry A, 2022. **10**(30): p. 15865-15880.

44. Qi, X., et al., *Stability trend, weak bonding, and magnetic properties of the Al- and Si-containing ternary-layered borides MAB phases.* Journal of the American Ceramic Society, 2023. **106**(2): p. 1513-1530.

45. Zhang, H., et al., *Crystal structure of Cr4AlB4: A new MAB phase compound discovered in Cr-Al-B system.* Journal of materials science & technology, 2019. **35**(4): p. 530-534.

46. Wang, J., et al., *Discovery of hexagonal ternary phase Ti2InB2 and its evolution to layered boride TiB.* Nature communications, 2019. **10**(1): p. 2284.

47. Miao, N., et al., *Discovery of Two-dimensional hexagonal MBene HfBO and exploration on its potential for Lithium-Ion storage.* Angewandte Chemie, 2023. **135**(36): p. e202308436.

48. Dahlqvist, M., et al., *Theoretical prediction and synthesis of a family of atomic laminate metal borides with in-plane chemical ordering.* Journal of the American Chemical Society, 2020. **142**(43): p. 18583-18591.

49. Kubitza, N., et al., *Extending the chemistry of layered solids and nanosheets: chemistry and structure of MAX phases, MAB phases and MXenes.* ChemPlusChem, 2023. **88**(8): p. e202300214.

50. Alameda, L.T., et al., *Partial etching of Al from MoAlB single crystals to expose catalytically active basal planes for the hydrogen evolution reaction.* Chemistry of Materials, 2017. **29**(21): p. 8953-8957.

51. Kim, K., et al., *Topochemical synthesis of phase-pure Mo 2 AlB 2 through staging mechanism.* Chemical communications, 2019. **55**(63): p. 9295-9298.

52. Wang, Y., et al., *Above-room-temperature strong ferromagnetism in 2D MnB nanosheet.* ACS nano, 2023. **17**(23): p. 24320-24328.

53. Zhou, J., et al., *Boridene: Two-dimensional Mo4/3B2-x with ordered metal vacancies obtained by chemical exfoliation.* Science, 2021. **373**(6556): p. 801-805.

54. Wang, Z., et al., *Discovery of Bimetallic Hexagonal MBene Mo2ErB3T2. 5 (T= O, F, and Cl).* Small, 2024. **20**(50): p. 2407100.

55. Zhang, H., et al., *First demonstration of possible two-dimensional MBene CrB derived from MAB phase Cr2AlB2.* Journal of Materials Science & Technology, 2018. **34**(11): p. 2022-2026.

56. Alameda, L.T., et al., *Multi-step topochemical pathway to metastable Mo2AlB2 and related two-dimensional nanosheet heterostructures.* Journal of the American Chemical Society, 2019. **141**(27): p. 10852-10861.

57. Bury, D., et al., *Wet-chemical etching and delamination of MoAlB into MBene and its outstanding photocatalytic performance.* Advanced Functional Materials, 2023. **33**(50): p. 2308156.

58. Xiong, W., et al., *Fluorine-free prepared two-dimensional molybdenum boride (MBene) as a promising anode for lithium-ion batteries with superior electrochemical performance.* Chemical Engineering Journal, 2022. **446**: p. 137466.

59. Wei, S., G. Kale, and X. Lai, *Unlocking Enhanced Electrochemical Performance of MBene-MoB Through Controlled Aluminum Dissipation from MoAlB.* Small, 2024. **20**(38): p. 2401573.

60. Khan, M.U., et al., *Hydrothermal green synthesis and electrochemical properties of Mo4/3B2Tx MBene.* Ionics, 2025. **31**(5): p. 5127-5137.

61. Mou, J., et al., *Deintercalation of Al from MoAlB by molten salt etching to achieve a Mo 2 AlB 2 compound and 2D MoB nanosheets.* Journal of Advanced Ceramics, 2023. **12**(5).

62. Baumler, K.J., O.S. Adams, and R.E. Schaak, *One-step topochemical transformation of MoAlB into metastable Mo 2 AlB 2 using a metal chloride salt reaction.* Chemical Communications, 2023. **59**(32): p. 4814-4817.

63. Li, Y., et al., *Molten salt derived Mo2AlB2 with excellent HER catalytic performance.* Materials Research Letters, 2023. **11**(7): p. 571-577.

64. Chen, Y.-Z., et al., *Layered Mo x B y (MBenes) derived by a molten-salt method and their application in advanced LIB anodes.* Journal of Materials Chemistry A, 2024. **12**(20): p. 12163-12172.

65. Guan, Y., J. Lai, and G. Xu, *Recent Advances on Electrocatalysis Using Pristinely Conductive Metal-Organic Frameworks and Covalent Organic Frameworks.* ChemElectroChem, 2021. **8**(15): p. 2764-2777.

66. Park, S.J., et al., *Delaminated MBene sheets beyond usual 2D transition metal materials for securing Pt single atoms to boost hydrogen evolution.* Energy & Environmental Science, 2023. **16**(9): p. 4093-4104.

67. Alameda, L.T., et al., *Topochemical deintercalation of Al from MoAlB: stepwise etching pathway, layered intergrowth structures, and two-dimensional MBene.* Journal of the American Chemical Society, 2018. **140**(28): p. 8833-8840.

68. Majed, A., et al., *Toward MBenes Battery Electrode Materials: Layered Molybdenum Borides for Li-Ion Batteries.* Small methods, 2023. **7**(8): p. 2300193.

69. Böhme, B., et al., *Oxidation of M4Si4 (M= Na, K) to clathrates by HCl or H2O.* Journal of the American Chemical Society, 2007. **129**(17): p. 5348-5349.

70. Böhme, B., et al., *Synthesis of the intermetallic clathrate Na2Ba6Si46 by oxidation of Na2BaSi4 with HCl.* Science and Technology of Advanced Materials, 2007. **8**(5): p. 410-415.

71. Liang, Y., et al., *Synthesis of the Clathrate-I Phase Ba8− x Si46 via Redox Reactions.* Inorganic chemistry, 2011. **50**(10): p. 4523-4528.

72. Hatipoglu, E., et al., *Design of metal-substituted tungsten diboride as an efficient bifunctional electrocatalyst for hydrogen and oxygen evolution.* International Journal of Energy Research, 2022. **46**(12): p. 17540-17555.

73. Wei, S., X. Lai, and G.M. Kale, *Exploring the potential of MBenes supercapacitors: fluorine-free synthesized MoAl1–x B with ultrahigh conductivity and open space.* ACS Applied Materials & Interfaces, 2023. **15**(28): p. 33560-33570.

74. Oppermann, H. and D. Huong, *Untersuchungen zur thermischen Zersetzung der Ammoniumyttriumhalogenide I. Ammoniumyttriumchloride.* Zeitschrift für anorganische und allgemeine Chemie, 1995. **621**(4): p. 665-670.

75. Yu, C.-C., et al., *Na2Ga7: A Zintl–Wade Phase Related to "α-Tetragonal Boron".* Inorganic Chemistry, 2023. **62**(23): p. 9054-9062.

76. Zhou, Y., et al., *Theoretical prediction on the stability, electronic structure, room and elevated temperature properties of a new MAB phase Mo2AlB2.* Journal of Materials Science & Technology, 2019. **35**(12): p. 2926-2934.

77. Pakharukova, V., et al., *Coherent 3D nanostructure of γ-Al2O3: Simulation of whole X-ray powder diffraction pattern.* Journal of solid state chemistry, 2017. **246**: p. 284-292.

78. Rudolph, M., M. Motylenko, and D. Rafaja, *Structure model of γ-Al2O3 based on planar defects.* IUCrJ, 2019. **6**(1): p. 116-127.

79. Yatsenko, D.A., V.P. Pakharukova, and S.V. Tsybulya, *Low temperature transitional aluminas: structure specifics and related x-ray diffraction features.* Crystals, 2021. **11**(6): p. 690.

80. Mou, J., et al., *Thermal stability and decomposition mechanism of Mo2AlB2 in argon atmosphere.* Ceramics International, 2024. **50**(11): p. 18758-18764.

81. Carlsson, A., J. Rosen, and M. Dahlqvist, *Finding stable multi-component materials by combining cluster expansion and crystal structure predictions.* npj Computational Materials, 2023. **9**(1): p. 21.

82. Cheng, Y., et al., *Aqueous MBene-based electrochemical filter capacitors with high frequency response and capacity density.* ACS Materials Letters, 2023. **5**(9): p. 2473-2480.

83. Natu, V., S.S. Kota, and M.W. Barsoum, *X-ray photoelectron spectroscopy of the MAB phases, MoAlB, M2AlB2 (M= Cr, Fe), Cr3AlB4 and their binary monoborides.* Journal of the European Ceramic Society, 2020. **40**(2): p. 305-314.

84. Fu, Y., et al., *Transition metal aluminum boride as a new candidate for ambient-condition electrochemical ammonia synthesis.* Nano-Micro Letters, 2020. **12**(1): p. 65.

85. Kota, S., et al., *Magnetic properties of Cr2AlB2, Cr3AlB4, and CrB powders.* Journal of Alloys and Compounds, 2018. **767**: p. 474-482.

86. Kota, S., et al., *Synthesis and characterization of the atomic laminate Mn2AlB2.* Journal of the European Ceramic Society, 2018. **38**(16): p. 5333-5340.

87. Peighambardoust, N.S., E. Hatipoglu, and U. Aydemir, *Structure-induced catalytic activity of nickel-and cobalt-substituted layered MoB2 toward hydrogen evolution.* ACS Sustainable Chemistry & Engineering, 2022. **10**(48): p. 15909-15925.

88. Wang, M., et al., *Alloying nickel with molybdenum significantly accelerates alkaline hydrogen electrocatalysis.* Angewandte Chemie, 2021. **133**(11): p. 5835-5841.

89. Chamani, S., et al., *Tuning electrochemical hydrogen-evolution activity of CoMoO4 through Zn incorporation.* Catalysts, 2023. **13**(5): p. 798.

90. Dionigi, F., et al., *Intrinsic electrocatalytic activity for oxygen evolution of crystalline 3d-transition metal layered double hydroxides.* Angewandte Chemie International Edition, 2021. **60**(26): p. 14446-14457.

91. Chen, B., et al., *In situ porousized MoS2 nano islands enhance HER/OER bifunctional electrocatalysis.* Small, 2023. **19**(14): p. 2207177.

92. Meyer, S., et al., *Transition metal carbides (WC, Mo2C, TaC, NbC) as potential electrocatalysts for the hydrogen evolution reaction (HER) at medium temperatures.* International Journal of Hydrogen Energy, 2015. **40**(7): p. 2905-2911.

93. Yu, L., et al., *A universal synthesis strategy to make metal nitride electrocatalysts for hydrogen evolution reaction.* Journal of Materials Chemistry A, 2019. **7**(34): p. 19728-19732.

94. Pan, Y., et al., *Monodispersed nickel phosphide nanocrystals with different phases: synthesis, characterization and electrocatalytic properties for hydrogen evolution.* Journal of Materials Chemistry A, 2015. **3**(4): p. 1656-1665.

95. Sadeghi, E., et al., *Designing in situ grown ternary oxide/2D Ni-BDC MOF nanocomposites on nickel foam as efficient electrocatalysts for electrochemical water splitting.* ACS Materials Au, 2022. **3**(2): p. 143-163.

96. *Introduction to Metal–Organic Frameworks.* Chemical Reviews, 2012. **112**(2): p. 673-674.

97. Senthil Raja, D., X.-F. Chuah, and S.-Y. Lu, *In Situ Grown Bimetallic MOF-Based Composite as Highly Efficient Bifunctional Electrocatalyst for Overall Water Splitting with Ultrastability at High Current Densities.* Advanced Energy Materials, 2018. **8**(23): p. 1801065.

98. Giddaerappa, et al., *Uranium Phthalocyanine-Anchored Acid-Functionalized Multiwalled Carbon Nanotubes for Water Electrolysis.* ACS Applied Nano Materials, 2023. **6**(10): p. 8880-8893.

99. Hadimane, S., et al., *Bioinspired Precious-Metal-Free N4 Macrocycle as an Electrocatalyst for the Hydrogen Evolution Reaction.* ACS Applied Energy Materials, 2021. **4**(10): p. 10826-10834.

100. K, V., et al., *A ligand-specific bimetallic electrocatalyst for efficient oxygen evolution reaction at higher current density.* Sustainable Energy & Fuels, 2025. **9**(9): p. 2287-2293.

101. Kousar, N., Giddaerappa, and L.K. Sannegowda, *Hybrid cobalt phthalocyanine polymer as a potential electrocatalyst for hydrogen evolution reaction.* International Journal of Hydrogen Energy, 2024. **50**: p. 37-47.

102. Chikkabasur Kumbara, A., N. Kousar, and L. Koodlur Sannegowda, *Catalytic Reinforcement in Hybrid Imidazole Functionalized Cobalt Phthalocyanine and Ketjenblack for Boosted Hydrogen Evolution.* Chemistry – An Asian Journal, 2025. **20**(7): p. e202401090.

103. Chen, W., et al., *Synthesis of ZIF-9(III)/Co LDH layered composite from ZIF-9(I) based on controllable phase transition for enhanced electrocatalytic oxygen evolution reaction.* Chemical Engineering Journal, 2021. **414**: p. 128784.

104. Zhang, L., et al., *Highly graphitized nitrogen-doped porous carbon nanopolyhedra derived from ZIF-8 nanocrystals as efficient electrocatalysts for oxygen reduction reactions.* Nanoscale, 2014. **6**(12): p. 6590-6602.

105. Yaqoob, L., et al., *Nanocomposites of cobalt benzene tricarboxylic acid MOF with rGO: An efficient and robust electrocatalyst for oxygen evolution reaction (OER).* Renewable Energy, 2020. **156**: p. 1040-1054.

106. Chen, J., et al., *From synthesis to energy storage, the microchemistry of MXene and MBene.* Advanced Energy Materials, 2025. **15**(17): p. 2403757.

107. Li, Z., et al., *Moss-like two-dimensional MBene-Ni/Co bimetallic metal-organic framework composite as efficient cathode for alkaline zinc batteries.* Journal of Power Sources, 2025. **633**: p. 236437.

108. Murtaza, M., et al., *Layered MOF supported on 2D delaminated MXene (Mo 2 Ti 2 C 3) nanosheets boosted water splitting.* Nanoscale Advances, 2024. **6**(24): p. 6317-6327.

109. Murtaza, M., et al., *Delaminated vanadium carbide MXene supported Two-dimensional (2D) CoNH2BDC MOF hybrid for enhanced water splitting.* Industrial & Engineering Chemistry Research, 2024. **63**(48): p. 20915-20924.

110. Murtaza, M., et al., *Bimetallic Fe/Ni-BTC MOF decorated MXene hybrid for improved oxidation of water.* Diamond and Related Materials, 2024. **147**: p. 111379.

111. Chaudhari, N.K., et al., *Nanostructured materials on 3D nickel foam as electrocatalysts for water splitting.* Nanoscale, 2017. **9**(34): p. 12231-12247.

112. Qu, H., et al., *Ni2P/C nanosheets derived from oriented growth Ni-MOF on nickel foam for enhanced electrocatalytic hydrogen evolution.* Journal of Colloid and Interface Science, 2020. **572**: p. 83-90.

113. Wang, Q., et al., *High Efficiency FeNi-Metal-Organic Framework Grown In-situ on Nickel Foam for Electrocatalytic Oxygen Evolution.* ChemistrySelect, 2019. **4**(19): p. 5988-5994.

114. Xu, L., et al., *NiFeLDH/Mo 4/3 B 2− x T z/NF composite electrodes to enhance oxygen evolution performance.* Journal of Materials Chemistry A, 2024. **12**(16): p. 9714-9722.

115. Xie, X., et al., *Ti3C2Tx MXene as a Janus cocatalyst for concurrent promoted photoactivity and inhibited photocorrosion.* Applied Catalysis B: Environmental, 2018. **237**: p. 43-49.

116. Xi, Q., et al., *In situ formation ZnIn2S4/Mo2TiC2 Schottky junction for accelerating photocatalytic hydrogen evolution kinetics: manipulation of local coordination and electronic structure.* Small, 2023. **19**(24): p. 2300717.

117. Carton, A., et al., *Ab initio crystal structure of nickel (II) hydroxy-terephthalate by synchrotron powder diffraction and magnetic study.* Solid state sciences, 2007. **9**(6): p. 465-471.

118. Carton, A., et al., *Structures of transition metal hydroxyterephthalates.* Zeitschrift für Kristallographie Supplements, 2007. **2007**(suppl_26): p. 581-586.

119. Mesbah, A., et al., *From hydrated Ni3 (OH) 2 (C8H4O4) 2 (H2O) 4 to anhydrous Ni2 (OH) 2 (C8H4O4): impact of structural transformations on magnetic properties.* Inorganic chemistry, 2014. **53**(2): p. 872-881.

120. Ahsan, M.A., et al., *Ultrafast catalytic reduction of environmental pollutants in water via MOF-derived magnetic Ni and Cu nanoparticles encapsulated in porous carbon.* Applied Surface Science, 2019. **497**: p. 143608.

121. Yang, J., et al., *Metal–organic frameworks: a new promising class of materials for a high performance supercapacitor electrode.* Journal of Materials Chemistry A, 2014. **2**(39): p. 16640-16644.

122. Li, F.L., et al., *Large-scale, bottom-up synthesis of binary metal–organic framework nanosheets for efficient water oxidation.* Angewandte Chemie, 2019. **131**(21): p. 7125-7130.

123. Yang, C., et al., *A new promising Ni-MOF superstructure for high-performance supercapacitors.* Chemical Communications, 2020. **56**(12): p. 1803-1806.

124. Sun, X., et al., *In Situ Construction of Flexible V□ Ni Redox Centers over Ni-Based MOF Nanosheet Arrays for Electrochemical Water Oxidation.* Small Methods, 2021. **5**(10): p. 2100573.

125. Sun, H., et al., *A hierarchical nickel–carbon structure templated by metal–organic frameworks for efficient overall water splitting.* Energy & Environmental Science, 2018. **11**(9): p. 2363-2371.

126. Fu, S., et al., *Accurate characterization of full pore size distribution of tight sandstones by low-temperature nitrogen gas adsorption and high-pressure mercury intrusion combination method.* Energy Science & Engineering, 2021. **9**(1): p. 80-100.

127. Thommes, M., et al., *Physisorption of gases, with special reference to the evaluation of surface area and pore size distribution (IUPAC Technical Report).* Pure and applied chemistry, 2015. **87**(9-10): p. 1051-1069.

128. Sun, Y., et al., *Modulating electronic structure of metal-organic frameworks by introducing atomically dispersed Ru for efficient hydrogen evolution.* Nature communications, 2021. **12**(1): p. 1369.

129. Huo, L., et al., *Applications of nickel-based electrocatalysts for hydrogen evolution reaction.* Advanced Energy and Sustainability Research, 2022. **3**(4): p. 2100189.

130. Sun, F., et al., *NiFe-based metal–organic framework nanosheets directly supported on nickel foam acting as robust electrodes for electrochemical oxygen evolution reaction.* Advanced Energy Materials, 2018. **8**(21): p. 1800584.

131. Yang, X., et al., *Heterogeneous Ni-MOF/V 2 CT x–MXene hierarchically-porous nanorods for robust and high energy density hybrid supercapacitors.* Journal of Materials Chemistry A, 2022. **10**(22): p. 12225-12234.

132. Chang, M., et al., *Two-dimensional layered MBene membrane towards sustainable freshwater production from solar interfacial evaporation.* Chemical Engineering Journal, 2024. **486**: p. 150078.

133. Chandel, M., et al., *Multilayered MoAlB@ MBene structures using mild microwave-assisted etching and their optical properties.* Materials Horizons, 2025. **12**(10): p. 3473-3484.

134. Xu, J., et al., *Powder metallurgy synthesis of porous NiMo alloys as efficient electrocatalysts to enhance the hydrogen evolution reaction.* Journal of Alloys and Compounds, 2021. **865**: p. 158901.

135. Sadeghi, E., et al., *NiMo/CoMoO4 heterostructure with confined oxygen vacancy for active and durable alkaline hydrogen evolution reaction.* ACS Applied Energy Materials, 2023. **6**(14): p. 7658-7671.

136. Sadeghi, E., et al., *In Situ Design of a Nanostructured Interface between NiMo and CuO Derived from Metal–Organic Framework for Enhanced Hydrogen Evolution in Alkaline Solutions.* ACS Applied Materials & Interfaces, 2024. **16**(8): p. 10078-10092.

137. Park, K., B. Chang, and S. Hwang, *Correlation between Tafel Analysis and Electrochemical Impedance Spectroscopy by Prediction of Amperometric Response from EIS. ACS Omega 2019, 4 (21), 19307–19313*.

138. Li, J., et al., *High electrochemical performance of monodisperse NiCo2O4 mesoporous microspheres as an anode material for Li-ion batteries.* ACS applied materials & interfaces, 2013. **5**(3): p. 981-988.

139. Zhou, Y., et al., *Enhancing the hydrogen activation reactivity of nonprecious metal substrates via confined catalysis underneath graphene.* Nano letters, 2016. **16**(10): p. 6058-6063.

140. Jiang, L., et al., *Modulate the surface charge toward efficient hydrogen evolution reaction: Electronic structure engineering of MoB-Ni3B interface.* Chemical Engineering Journal, 2024. **485**: p. 149920.

141. Yang, Y., et al., *Vacancy and Dopant Co-Constructed Active Microregion in Ru–MoO3− x/Mo2AlB2 for Enhanced Acidic Hydrogen Evolution.* Angewandte Chemie, 2025: p. e202504084.

142. Helmer, P., et al., *Investigation of 2D boridene from first principles and experiments.* Advanced Functional Materials, 2022. **32**(14): p. 2109060.

143. Wang, Q., et al., *MOF-derived porous Ni 2 P nanosheets as novel bifunctional electrocatalysts for the hydrogen and oxygen evolution reactions.* Journal of Materials Chemistry A, 2018. **6**(38): p. 18720-18727.

144. Xu, X., et al., *Large-scale synthesis of porous nickel boride for robust hydrogen evolution reaction electrocatalyst.* Applied Surface Science, 2019. **470**: p. 591-595.

145. Gothandapani, K., et al., *Ni-Ti3C2 MXene composite derived from Ni-metal organic framework for electrochemical hydrogen evolution reaction in acidic and alkaline medium.* International Journal of Hydrogen Energy, 2024. **52**: p. 1164-1171.

Appendix A

Table A1 Miller indices, experimental and calculated 2 Theta values, and their differences (Delta) used for the calculation of lattice parameters.

h	k	l	2-theta(exp)	2-theta(cal)	Delta
0	2	0	14.99	15.311	-0.321
0	0	1	28.229	28.342	-0.113
1	1	0	30.065	30.023	0.042
0	4	0	30.799	30.904	-0.105
0	2	1	32.474	32.367	0.107
1	3	0	37.527	37.36	0.167
1	1	1	41.631	41.758	-0.127
0	4	1	42.503	42.425	0.078
0	6	0	47.067	47.113	-0.046
1	3	1	47.582	47.548	0.034
1	5	0	49.167	49.242	-0.075
0	6	1	55.653	55.896	-0.243
0	0	2	58.461	58.633	-0.172
2	0	0	60.01	60.079	-0.069
1	7	0	63.634	63.902	-0.268
0	8	0	64.787	64.399	0.388
1	1	2	67.513	67.272	0.241
2	0	1	67.961	67.732	0.229
1	7	1	71.568	71.335	0.233
1	3	2	71.751	71.617	0.134
2	4	1	76.337	76.292	0.045
1	5	2	79.919	80.015	-0.096
0	10	0	83.582	83.531	0.051
2	6	1	86.402	86.589	-0.187
2	0	2	88.762	88.892	-0.13

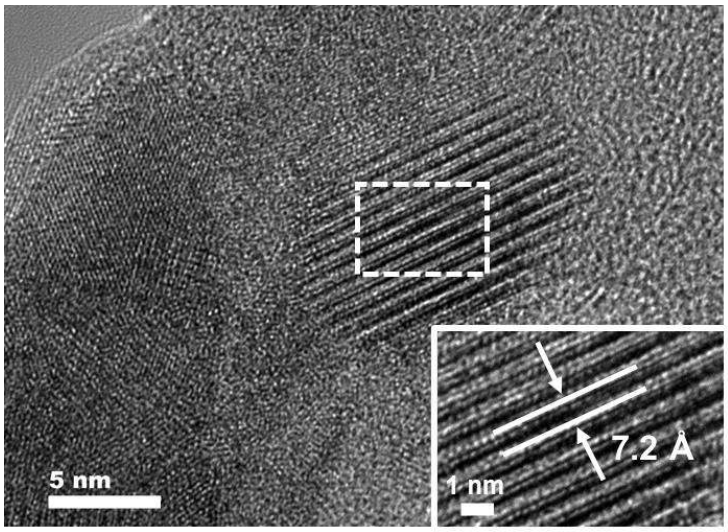

Figure A1 HR-TEM images of MoAlB which corresponds to (020) plane. The interlayer spacing is 7.2 Å.

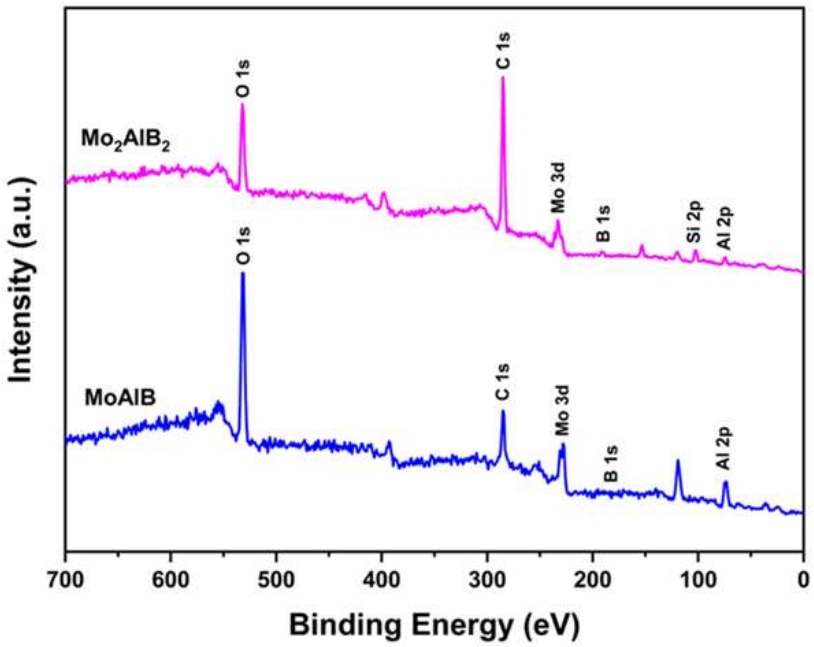

Figure A2 XPS survey of MoAlB and Mo_2AlB_2.

Appendix B

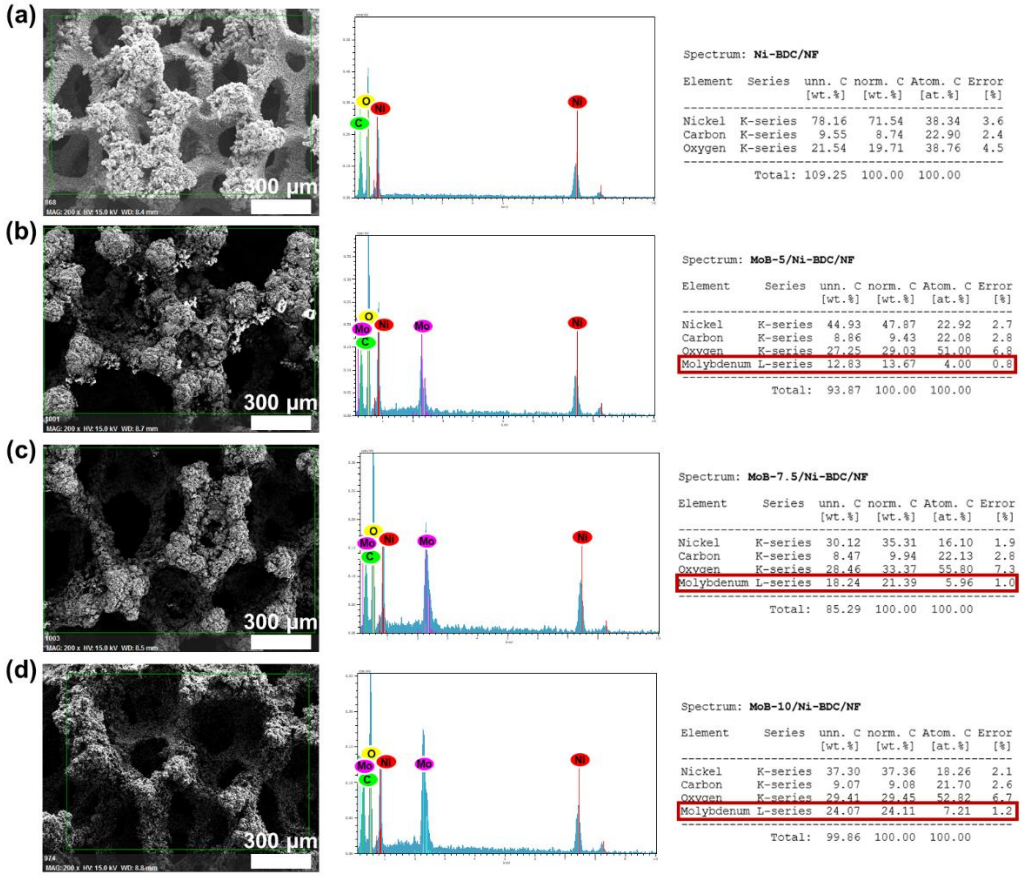

Figure B1 SEM-EDS analysis of (a) Ni-BDC/NF and (b-d) MoB-X/Ni-BDC/NF (X: 5, 7.5, 10).

Table B1 BET surface area, BJH adsorption pore volume, and average pore size, along with the estimated nanoparticle size of the samples.

Sample	BET Surface Area (m^2/g)	BJH Adsorption Pore Volume (cm^3/g)	BJH Adsorption Avg. Pore Size (Å)	Average Nanoparticle Size (nm)
Ni-BDC	4.8184	0.032631	387.708	124.52318
MoB-7.5/Ni-BDC	2.4941	0.014286	318.948	240.56759
MoB-7.5/Ni-BDC/*400*	26.0601	0.134013	269.445	23.02369

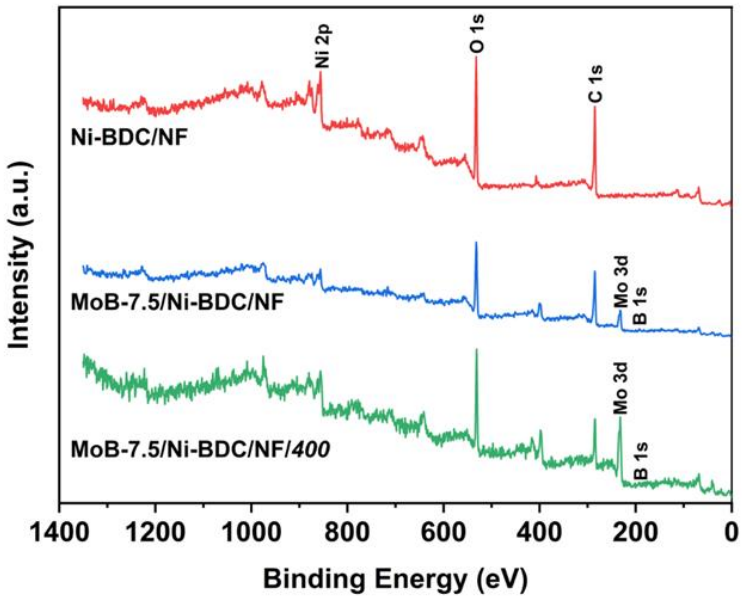

Figure B2 XPS survey spectra of Ni-BDC/NF, MoB-7.5/Ni-BDC/NF and MoB-7.5/Ni-BDC/NF/*400*.

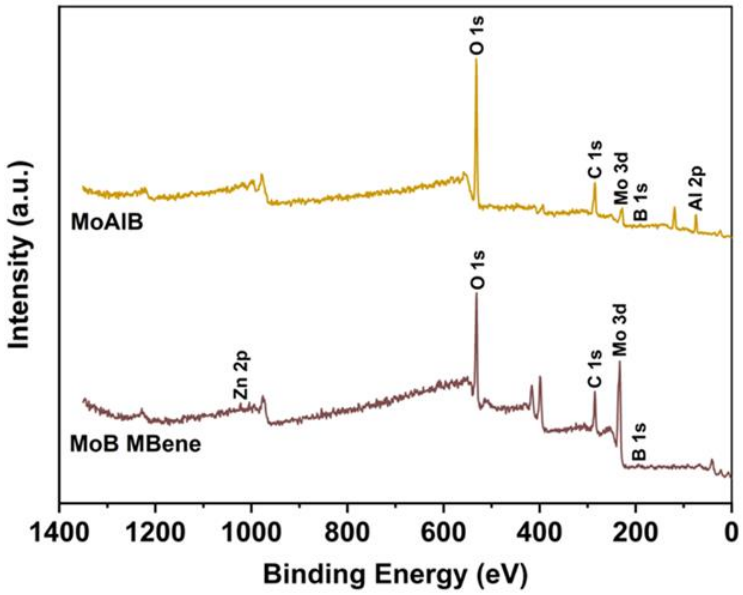

Figure B3 XPS survey spectrum of MoAlB and MoB MBene.

Table B2 Literature comparison of hydrogen evolution reaction performance parameters for representative MBene-based and Ni-based electrocatalysts.

Catalysts	Electrolyte	Substrate	η_{10} @10 mA cm^{-2} (mV)	Tafel (mV/dec)	ECSA/C_{dl} (mF cm^{-2})	Stability	Ref.
MoAlB (not etched)	0.5 M H_2SO_4	-	400	85	-	24 h	[50]
MoAlB (etched)			301	61		24 h	
MoAlB	1.0 M KOH	Carbon Paper	410	219.7	0.63	24 h	[63]
Mo_2AlB_2			145	76	1.31	24 h	
MoAlB	1.0 M KOH	Ni Foam	224	-	-	-	[66]
$MoAl_{1-x}B$			197	-	3.84	-	
Pt - $MoAl_{1-x}B$			32	83.6	4.52	80 h	
MoAlB	0.5 M H_2SO_4	Carbon Cloth	385	-	-	-	
$MoAl_{1-x}B$			253	-	5.28	-	
Pt - $MoAl_{1-x}B$			18	78.8	9.54	80 h	
MoAlB	0.5 M H_2SO_4	Carbon Paper	445	167.5	0.54	-	[141]
Mo_2AlB_2			252	156.7	7.9	-	
MoO_{3-x}/Mo_2AlB_2			75	77.9	15.8	-	
Ru-MoO_{3-x}/Mo_2AlB_2			38	57.1	27	100 h	
$Mo_{4/3}B_2T_x$	0.5 M H_2SO_4	Glassy Carbon	-	241	-	67 h	[142]
Ni-BDC	1.0 M KOH	Ni Foam	268	150.9	0.22	-	[95]
NCZ/Ni-BDC			170	137.2	0.483	32 h	
Ni/C-600	1.0 M KOH	Ni Foam	37	57	95	70 h	[125]
Ni_2P	1.0 M KOH	Glassy Carbon	168	63	3.44	10 h	[143]
Ni_3B-850	0.5 M H_2SO_4	-	79	85.32	63.44	24 h	[144]
$CoNiNH_2BDC$ MOF	1.0 M KOH	Glassy Carbon	135	88	1.17	-	[108]
$Mo_2Ti_2C_3T_x$			224	137	1.13	-	
MOFMX3			37	45	9.42	1000 CV cycle	
Ni-MOF	0.1 M NaOH	Glassy Carbon	210.43	78.12	-	-	[145]
Ti_3C_2			202.15	75	2.512	-	
Ni-Ti_3C_2			181.15	56.5	2.856	1000 CV cycle	
Ni-MOF	0.5 M H_2SO_4		241	107.2	-	-	
Ti_3C_2			224	93.2	2.041	-	
Ni-Ti_3C_2			187.25	67.21	2.275	1000 CV cycle	

Table B3 Fit parameters for the samples derived from EIS experiments.

Samples	R_s (Ω)	R_p (Ω)	CPE-T (F^{-1} s^{1-n})	R_{ct} (Ω)	C_{dl}-T (F^{-1} s^{1-n})
MoB/NF	3.128	301.7	0.00065312	220.2	0.18583
MoB/*400*/NF	2.956	136.1	0.00033756	596.6	0.000419
Ni-BDC/NF	2.653	47.1	0.0020414	78.48	0.0053481
MoB-5/Ni-BDC/NF	2.501	47.47	0.001707	49.78	0.011081
MoB-7.5/Ni-BDC/NF	2.547	50.87	0.0014615	35.42	0.014941
MoB-10/Ni-BDC/NF	2.609	55.82	0.0015219	68.9	0.0080455
MoB-7.5/Ni-BDC/NF/*300*	3.66	169	0.0025078	109.3	0.027396
MoB-7.5/Ni-BDC/NF/*400*	3.15	39.78	0.20237	5.4	0.37525

Table B4 Turnover frequency (TOF) values of MoB-x/Ni-BDC/NF electrocatalysts as a function of overpotential.

Catalysts	100 mV	150 mV	200 mV	250 mV	300 mV	350 mV	400 mV
MoB/NF	0.000156	0.000227	0.000396	0.000659	0.001367	0.002111	0.002909
MoB/*400*/NF	0.000126	0.000186	0.000339	0.000835	0.001773	0.003169	0.005082
Ni-BDC/NF	0.000750	0.001149	0.001863	0.003432	0.006736	0.012293	0.019489
MoB-5/Ni-BDC/NF	0.001066	0.001519	0.002275	0.003693	0.006480	0.010992	0.017186
MoB-7.5/Ni-BDC/NF	0.001222	0.001830	0.002683	0.003986	0.006053	0.009295	0.014574
MoB-10/Ni-BDC/NF	0.000761	0.001216	0.001978	0.0030661	0.004978	0.007926	0.011891
MoB-7.5/Ni-BDC/NF/*300*	0.000606	0.001035	0.001723	0.0029087	0.004866	0.008033	0.012496
MoB-7.5/Ni-BDC/NF/*400*	0.002677	0.003909	0.005549	0.007509	0.009968	0.012630	0.015639